NAVAL POSTGRADUATE SCHOOL
Monterey, California

DTIC QUALITY INSPECTED 4

THESIS

NUMERICAL MODELING OF
OPTO-ELECTRONIC INTEGRATED CIRCUITS

by

Christopher C. Foster

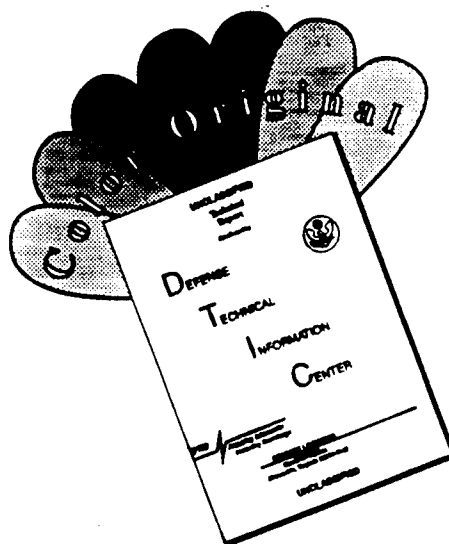December 1994

Thesis Advisor: Phillip E. Pace
Thesis Co-Advisor: Alfred W. M. Cooper

19950310 009

DISCLAIMER NOTICE

THIS DOCUMENT IS BEST QUALITY AVAILABLE. THE COPY FURNISHED TO DTIC CONTAINED A SIGNIFICANT NUMBER OF COLOR PAGES WHICH DO NOT REPRODUCE LEGIBLY ON BLACK AND WHITE MICROFICHE.

REPORT DOCUMENTATION PAGE

Public reporting burden for this collection of information is estimated to average 1 hour per response, including the time for reviewing instructions, searching existing data sources, gathering and maintaining the data needed, and completing and reviewing the collection of information. Send comments regarding this burden estimate or any other aspect of this collection of information, including suggestions for reducing the burden, to Washington Headquarters Services, Directorate for Information Operations and Reports, 1215 Jefferson Davis Highway, Suite 1204, Arlington, VA 22202-4302, and to the Office of Management and Budget, Paperwork Reduction Project (0704-0188), Washington, DC 20503.

1. AGENCY USE ONLY *(Leave blank)*	2. REPORT DATE December, 1994	3. REPORT TYPE AND DATES COVERED Master's Thesis

4. TITLE AND SUBTITLE
NUMERICAL MODELING OF OPTO-ELECTRONIC INTEGRATED CIRCUITS

5. FUNDING NUMBERS

6. AUTHOR(S)
Foster, Christopher C.

7. PERFORMING ORGANIZATION NAME(S) AND ADDRESS(S)
Naval Postgraduate School
Monterey, Ca. 93943-5000

8. PERFORMING ORGANIZATION REPORT NUMBER

9. SPONSORING / MONITORING AGENCY NAME(S) AND ADDRESS(S)

10. SPONSORING / MONITORING AGENCY REPORT NUMBER

11. SUPPLEMENTARY NOTES
The views expressed in this thesis are those of the author and do not reflect the official policy or position of the Department of Defense or the U.S. Government.

12a. DISTRIBUTION / AVAILABILITY STATEMENT
Approved for public release; distribution unlimited

12b. DISTRIBUTION CODE

13. ABSTRACT *(Maximum 200 words)*

This thesis develops an efficient and effective method for designing and analyzing the performance of various integrated optical waveguide structures using the beam propagation method of analysis. Modifications in the physical layout of an optical device through changes in coupling connection design, splitting angles and waveguide dimensions may have significant effects on device performance. The beam propagation method is initially developed for a symmetric Mach-Zehnder interferometer for baseline validation of the accuracy and applicability of the propagation scheme. A major validation is achieved through modeling an asymmetric device designed and built by the Naval Research Laboratory. The validated simulation model is used to analyze the performance and design characteristics of complex parallel configurations of interferometers. The beam propagation method allows quantitative analysis of the performance of these integrated optical devices. The propagation model developed implements a new global propagator scheme that substantially reduces computational requirements and introduces a design methodology that ensures compatibility between the discrete implementation and the physical structure. Also identified are areas in which continued research can provide a complete modeling system that may be implemented as a stand-alone design and analysis.

14. SUBJECT TERMS
Mach-Zehnder Interferometer (MZI), Beam Propagation Method (BPM).

15. NUMBER OF PAGES
117

16. PRICE CODE

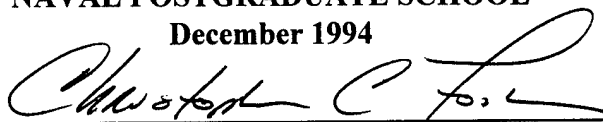| 17. SECURITY CLASSIFICATION OF REPORT	18. SECURITY CLASSIFICATION OF THIS PAGE	19. SECURITY CLASSIFICATION OF ABSTRACT	20. LIMITATION OF ABSTRACT
UNCLASSIFIED	UNCLASSIFIED	UNCLASSIFIED	UL

NUMERICAL MODELING OF
OPTO-ELECTRONIC INTEGRATED CIRCUITS
by

Christopher C. Foster
Captain, United States Marine Corps
B. S., Southern Illinois University, 1984

Submitted in partial fulfillment
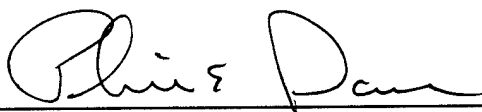of the requirements for the degree of

MASTER OF SCIENCE IN ELECTRICAL ENGINEERING
and
MASTER OF SCIENCE IN APPLIED PHYSICS
and
ELECTRICAL ENGINEER
from the
NAVAL POSTGRADUATE SCHOOL
December 1994

Author: _____

Christopher C. Foster
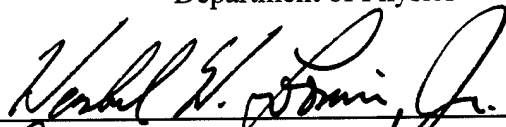
Approved by: _____

Phillip E. Pace, Thesis Advisor

_____

Alfred W. M. Cooper, Co-Advisor

_____

William B. Colson, Chairman,
Department of Physics

_____

for   Michael A. Morgan, Chairman,
Department of Electrical and Computer Engineering

Accesion For		
NTIS CRA&I	☑	
DTIC TAB	☐	
Unannounced	☐	
Justification		
By		
Distribution /		
Availability Codes		
Dist	Avail and / or Special	
A-1		

iii

ABSTRACT

This Thesis develops an efficient and effective method for designing and analyzing the performance of various integrated optical waveguide structures using the beam propagation method of analysis. Modifications in the physical layout of an optical device through changes in coupling connection design, splitting angles and waveguide dimensions may have significant effects on device performance. The beam propagation method is initially developed for a symmetric Mach-Zehnder interferometer for baseline validation of the accuracy and applicability of the propagation scheme. A major validation is achieved through modeling an asymmetric device designed and built by the Naval Research Laboratory. The validated simulation model is used to analyze the performance and design characteristics of complex parallel configurations of interferometers. The beam propagation method allows quantitative analysis of the performance of these integrated optical devices. The propagation model developed implements a new global propagator scheme that substantially reduces computational requirements and introduces a design methodology that ensures compatibility between the discrete implementation and the physical structure. Also identified are areas in which continued research can provide a complete modeling system that may be implemented as a stand-alone design and analysis tool.

TABLE OF CONTENTS

ix

LIST OF FIGURES

ACKNOWLEDGMENT

I. INTRODUCTION

A. BACKGROUND

A number of computational schemes exist which can be used to numerically model integrated optical waveguide structures. These schemes include the second-order finite differencing method, the split operator method, the short iterative Lanczos propagator and the Chebyshev scheme. These schemes have been utilized to propagate solutions to the scalar Homogeneous Helmholtz equation and the time dependent Schrödinger equation as well [1]. The applicability of the propagation scheme to the physical structure, numerical efficiency, stability of the solution and computational constraints must all be considered when choosing a modeling scheme.

The beam propagation method (BPM) is a split operator method to solve the scalar Homogeneous Helmholtz equation. The BPM has been shown to be an effective, efficient tool for generating required numerical solutions for waveguide structures [1]. The BPM permits the rapid analysis of design parameters and overall system performance in an extremely short period of time.

B. PRINCIPLE CONTRIBUTIONS

Although the BPM has been previously utilized for optical analysis [2, 3], the time constraints and required flexibility for analyzing relatively long complex integrated optical devices posed serious problems. This thesis develops an optimal BPM algorithm for integrated optic circuits. This thesis develops a methodology for ensuring that the discrete parameters used to implement a physical device are matched to the device

1

parameters by utilizing a subtle aspect of sampling theory that forces equalization. A major contribution of this thesis is the development of the global propagator scheme. The global propagator developed in this thesis has made the BPM an important tool for designing and analyzing the long structures required for highly sensitive voltage detection devices such the Mach-Zehnder Interferometer (MZI).

This thesis attempts to prove the applicability of the BPM through modeling an existing device and comparing the theoretical BPM results to actual data measured in the laboratory. The resulting confirmation of the validity of the BPM demonstrates the potential applicability of the method. The validated BPM is utilized to analyze more complex parallel MZI structures. The performance of parallel structures is evaluated as a function of separation distance between the individual interferometers, and the effects of radiation mode coupling are quantified.

C. THESIS ORGANIZATION

This thesis begins in Chapter II with the mathematical development of the BPM algorithm. The BPM algorithm is a numerical solution to the scalar Helmholtz equation. The equation is broken down into an alternate series of propagation and lens terms that allow the optical field to propagate through a guiding structure. The constraints and limitations of the BPM are analyzed and a complete set of algorithm design equations are developed. This development provides the basis for the global propagator scheme that is employed in this thesis.

In Chapter III the first test of the BPM is the simulation of the well known symmetric MZI. Since the single symmetric MZI has been previously analyzed the expected output is available for comparison. Although the equations for the output of the single MZI do not include radiation losses, this first step is vital in developing a reliable design tool. This provides the basis for validation of the global propagator, and demonstrates the methodology for implementing the discrete matched device parameters.

The modeling of the single asymmetric MZI is a major validation phase of the code development performed in Chapter IV. The BPM representation of the asymmetric interferometer is developed and the BPM analysis is compared to the physical data measured in the laboratory. The BPM is shown to be a valid integrated optical design tool that effectively implements radiation losses due to device characteristics.

The complex analysis of a parallel configuration of Mach-Zehnder Interferometers is performed in Chapter V. Parallel configurations of guided wave MZI are important in signal processing architecture that utilize voltage modulators. The BPM is used to analyze the effects of radiation mode coupling between adjacent interferometers and radiation losses due to branching angles and power dividers.

Finally, Chapter VI addresses the potential use of the BPM for design of other integrated optical devices. The use of integrated optics is a growing area of signal processing and the use of optical computers is rapidly becoming a reality. Potential improvements of the BPM algorithm to include other optical effects and unusual design parameters are addressed.

II. DEVELOPMENT OF AN OPTIMAL BPM ALGORITHM

A. BEAM PROPAGATION METHOD

The Beam Propagation Method (BPM) is a numerical solution to the wave equation that effectively models an optical structure as a series of infinitely thin lenses separated by an incremental axial distance Δz.

1. Fresnel Approximation to the Wave Equation

If we assume that light propagating in an optical waveguide is monochromatic, then we can apply the homogeneous Helmholtz Equation

$$\nabla^2 \bar{E} + \frac{\omega^2}{c^2} n^2(\omega, x, y)\bar{E} = 0, \tag{1}$$

where the refractive index $n^2(\omega, x, y)$ is assumed to only have dependence on the x and y coordinates [4]. If we assume a forward propagating field in the $+z$ direction, then we can express $\bar{E}(\omega, x, y, z)$ as

$$\bar{E}(\omega, x, y, z) = E \exp(-jkz), \tag{2}$$

where

$$k = n_0 \omega/c, \tag{3}$$

and n_o is the refractive index of the substrate.

By substituting Equation (2) into Equation (1) we now have

$$\nabla^2 E \exp(-jkz) + \frac{\omega^2}{c^2} n^2(x, y)E \exp(-jkz) = 0. \tag{4}$$

Since

$$\nabla^2 = \frac{\partial^2}{\partial x^2} + \frac{\partial^2}{\partial y^2} + \frac{\partial^2}{\partial z^2}, \tag{5}$$

we can evaluate the partial derivative with respect to z separately, so that

$$\frac{\partial^2}{\partial z^2} E \exp(-jkz) = \frac{\partial}{\partial z}\left[\frac{\partial}{\partial z} E \exp(-jkz)\right] \tag{6}$$

$$= \frac{\partial}{\partial z}\left[\exp\left(-jkz\right)\frac{\partial}{\partial z}\mathbf{E} - jk\,\mathbf{E}\exp\left(-jkz\right)\right] \tag{7}$$

$$= \exp\left(-jkz\right)\frac{\partial^2}{\partial z^2}\mathbf{E} - jk\exp\left(-jkz\right)\frac{\partial}{\partial z}\mathbf{E} - k^2\exp\left(-jkz\right)\mathbf{E} - jk\exp\left(-jkz\right)\frac{\partial}{\partial z}\mathbf{E} \tag{8}$$

$$= \exp\left(-jkz\right)\frac{\partial^2}{\partial z^2}\mathbf{E} - 2jk\exp\left(-jkz\right)\frac{\partial}{\partial z}\mathbf{E} - k^2\exp\left(-jkz\right)\mathbf{E}. \tag{9}$$

By substituting Equation (9) into Equation (4) we now have

$$\frac{\partial^2}{\partial z^2}\mathbf{E} - 2jk\frac{\partial}{\partial z}\mathbf{E} - k^2\mathbf{E} + \nabla_\perp^2\mathbf{E} + k^2\frac{n^2}{n_0^2}\mathbf{E} = 0, \tag{10}$$

where

$$\nabla_\perp^2 = \frac{\partial^2}{\partial x^2} + \frac{\partial^2}{\partial y^2}. \tag{11}$$

Now, rearranging the terms of Equation (10) into a more recognizable form we have

$$-\frac{\partial^2}{\partial z^2}\mathbf{E} + 2jk\frac{\partial}{\partial z}\mathbf{E} = \nabla_\perp^2\mathbf{E} + k^2\left(\frac{n^2}{n_0^2} - 1\right)\mathbf{E}. \tag{12}$$

If the field is slowly varying in the $+z$ direction then we can neglect the first term on the left in Equation (12). This gives the paraxial or Fresnel form of the wave equation

$$2jk\frac{\partial}{\partial z}\mathbf{E}' = \nabla_\perp^2\mathbf{E}' + k^2\left(\frac{n^2}{n_0^2} - 1\right)\mathbf{E}' \tag{13}$$

or

$$\frac{\partial}{\partial z}\mathbf{E}' + \frac{j}{2k}\left[\nabla_\perp^2 + k^2\left(\frac{n^2}{n_0^2} - 1\right)\right]\mathbf{E}' = 0, \tag{14}$$

where $\mathbf{E}'$ represents solutions to the Fresnel approximation to the wave equation. Since Equation (14) represents a standard ordinary differential equation, the solution is

$$\mathbf{E}'(x,y,\Delta z) = \exp\left[-\frac{j\Delta z}{2k}\left(\nabla_\perp^2 + k^2\left(\frac{n^2}{n_0^2} - 1\right)\right)\right]\mathbf{E}'(x,y,0), \tag{15}$$

where $\mathbf{E}'(x, y, 0)$ is the initial condition of the field at $z = 0$. Separating the operation of the exponent in Equation (15) provides the basis for the Split Operator Method (SOM) or BPM [2], so that we now have

$$\mathbf{E}'(x, y, \Delta z) = \exp\left(-\frac{j\Delta z}{2k}\nabla_\perp^2\right)\exp\left(-\frac{j\Delta z}{2k}k^2\left(\frac{n^2}{n_0^2} - 1\right)\right)\mathbf{E}'(x, y, 0). \tag{16}$$

As developed in [2], Equation (16) can be further split so that

$$\mathbf{E}'(x, y, \Delta z) = \exp\left(-\frac{j\Delta z}{4k}\nabla_\perp^2\right)\exp\left(-\frac{j\Delta z k}{2}\left(\frac{n^2}{n_0^2} - 1\right)\right)\exp\left(-\frac{j\Delta z}{4k}\nabla_\perp^2\right)\mathbf{E}'(x, y, 0)$$

$$+ O(\Delta z)^3, \tag{17}$$

where the three exponential factors represent a half step of propagation, a phase or lens term, and a second half step of propagation respectively. Since the $\nabla_\perp^2$ term in the first exponential term of Equation (16) does not commute with the x and y dependence of the second exponential term, an error term $O(\Delta z)^3$ is introduced in Equation (17). The error term is not evaluated at this point since the split operation is not actually performed in the BPM implementation. In structures that require large axial distances, adjacent propagation steps are normally combined to reduce computation time, as will be shown in a later section. However, Equation (17) provides an excellent method of visualizing the propagation process by replacing the optical waveguide with a series of infinitely thin lenses [1], as shown in Figure 1.

If the initial field is composed of a limited spectral bandwidth then the field can be represented by a truncated Fourier series such that

$$\mathbf{E}'(x, y, z) = \sum_{m=-N/2+1}^{N/2} \sum_{n=-M/2+1}^{M/2} \mathbf{E}'_{mn}(z) \exp\left[j\left(\frac{2\pi mx}{L_1} + \frac{2\pi ny}{L_2}\right)\right], \tag{18}$$

7

where L_1 is the width of the computational grid in the x direction, L_2 is the width of the computational grid in the y direction and N and M are the total transverse points in the
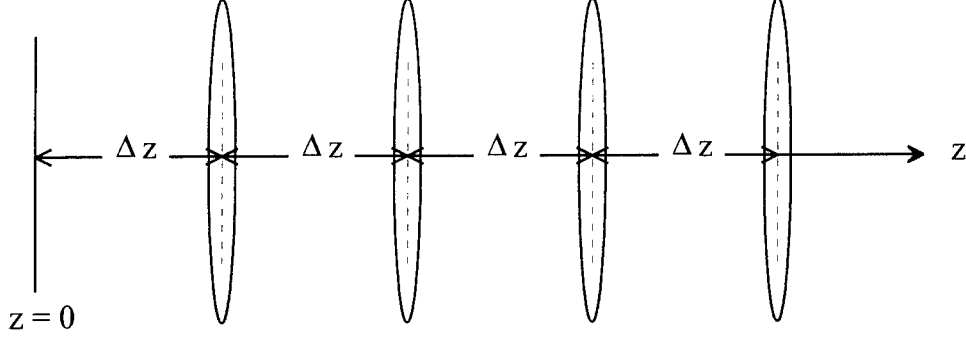
Figure 1. Thin lens representation of BPM algorithm.

computational grid. If the propagation term

$$\exp\left(-\frac{j\Delta z}{4k}\nabla_\perp^2\right)$$

(19)

operates on the Fourier series representation of Equation (18) the result is that

$$E'_{mn}(z+\Delta z/2) = E'_{mn}(z)\exp\left[\frac{j\Delta z}{4k}\left(\left(\frac{2\pi m}{L_1}\right)^2 + \left(\frac{2\pi n}{L_2}\right)^2\right)\right].$$

(20)

This technique allows the field to propagate forward by calculating new Fourier coefficients based on the spatial frequency propagator

$$\exp\left[\frac{j\Delta z}{4k}\left(\left(\frac{2\pi m}{L_1}\right)^2 + \left(\frac{2\pi n}{L_2}\right)^2\right)\right]$$

(21)

that is used in Equation (20). In effect this leads to the determination of a new Fourier series representation of $E'(x, y, z + \Delta z/2)$ utilizing Equation (18). The new representation of the complex field is then multiplied by the lens term

$$\exp\left[-\frac{jk\Delta z}{2}\left(\frac{n^2}{n_0^2}-1\right)\right]$$

(22)

of Equation (17). This in turn leads to the determination of another Fourier series representation of the field at $E'(x, y, z + \Delta z/2$ immediately after the lens, and the

8

propagation step is applied once more. The application of Equation (20) allows the use of Fast Fourier Transform algorithms to implement the propagation terms in Equation (17). This concept allows for a much easier algebraic implementation of the propagation term in the spatial frequency domain, while the phase or lens term is performed with simple multiplication in the spatial domain. Thus, the BPM consists of a set of Fourier transforms interspersed with complex multiplications in the spatial domain in an iterative algorithm that advances the solution in successive steps along the optic axis [5]. The Fourier transforms are carried out using the well known *Danielson-Lanczos* FFT algorithm and require transverse grids of $2^{m_1} \times 2^{m_2}$ in the spatial and spectral domains, where m_1 and m_2 are determined by N and M of Equation (18) and are subsequently analyzed.

2. Direct Solution to the Wave Equation

An alternate method of developing a split operator solution to the wave equation without initially making the Fresnel approximation has also been utilized [2]. If Equation (1) is rewritten in the form

$$\frac{\partial^2}{\partial z^2}\mathbf{E} + \left(\nabla_\perp^2 + \frac{\omega^2}{c^2}n^2(x,y)\right)\mathbf{E} = 0, \tag{23}$$

the representation of Equation (23) can be treated as a second order ordinary differential equation. The solution at $z = \Delta z$ may be written in terms of the field at $z = 0$ as

$$\mathbf{E}(x,y,\Delta z) = \exp\left[\pm j \,\Delta z\left(\nabla_\perp^2 + \frac{\omega^2}{c^2}n^2\right)^{1/2}\right]\mathbf{E}(x,y,0). \tag{24}$$

The square root in the exponent of Equation (24) can be written in the form

9

$$\left(\nabla_\perp^2 + \frac{\omega^2}{c^2}n^2\right)^{1/2} = \frac{\left(\nabla_\perp^2 + (\omega n/c)^2\right)^{1/2}\left[\left(\nabla_\perp^2 + (\omega n/c)^2\right)^{1/2} + (\omega n/c)\right]}{\left(\nabla_\perp^2 + (\omega n/c)^2\right)^{1/2} + (\omega n/c)} \qquad (25)$$

$$= \frac{\left(\nabla_\perp^2 + (\omega n/c)^2\right) + \left(\nabla_\perp^2 + (\omega n/c)^2\right)^{1/2}(\omega n/c)}{\left(\nabla_\perp^2 + (\omega n/c)^2\right)^{1/2} + (\omega n/c)} \qquad (26)$$

$$= \frac{\nabla_\perp^2}{\left(\nabla_\perp^2 + (\omega n/c)^2\right)^{1/2} + (\omega n/c)} + \frac{(\omega n/c)^2 + (\omega n/c)\left(\nabla_\perp^2 + (\omega n/c)^2\right)^{1/2}}{\left(\nabla_\perp^2 + (\omega n/c)^2\right)^{1/2} + (\omega n/c)} \qquad (27)$$

$$= \frac{\nabla_\perp^2}{\left(\nabla_\perp^2 + (\omega n/c)^2\right)^{1/2} + (\omega n/c)} + \frac{(\omega n/c)\left[(\omega n/c) + \left(\nabla_\perp^2 + (\omega n/c)^2\right)^{1/2}\right]}{\left(\nabla_\perp^2 + (\omega n/c)^2\right)^{1/2} + (\omega n/c)} \qquad (28)$$

$$= \frac{\nabla_\perp^2}{\left(\nabla_\perp^2 + (\omega n/c)^2\right)^{1/2} + (\omega n/c)} + (\omega n/c). \qquad (29)$$

If the variations in $n(x,y)$ are sufficiently small, then the n in the first right hand member

of Equation (29) can be replaced with n_o and utilizing Equation (3) we have

$$\left(\nabla_\perp^2 + \frac{\omega^2}{c^2}n^2\right)^{1/2} \cong \frac{\nabla_\perp^2}{\left(\nabla_\perp^2 + k^2\right)^{1/2} + k} + k\frac{n}{n_o} \qquad (30)$$

$$= \frac{\nabla_\perp^2}{\left(\nabla_\perp^2 + k^2\right)^{1/2} + k} + k + k\frac{n}{n_o} - k \qquad (31)$$

$$= \frac{\nabla_\perp^2}{\left(\nabla_\perp^2 + k^2\right)^{1/2} + k} + k + k\left(\frac{n}{n_o} - 1\right). \qquad (32)$$

10

If we now substitute Equation (32) into Equation (24) and assume a + z propagating wave, we can apply Equation (2) and we have

$$E(x, y, \Delta z) = \exp\left(-j\,\Delta z \frac{\nabla_\perp^2}{\left(\nabla_\perp^2 + k^2\right)^{1/2} + k} + k\left(\frac{n}{n_o} - 1\right)\right) E(x, y, 0). \tag{33}$$

At this point the resemblance to the Fresnel approximation solution given in Equation (15) is readily apparent. However, if $\nabla_\perp^2$ in the denominator of Equation (33) is neglected in comparison to k^2, an almost exact reproduction of Equation (15) is recovered. The representation of Equation (33) can now be written as

$$E(x, y, \Delta z) \cong \exp\left(-\frac{j\,\Delta z}{2k}\nabla_\perp^2\right) \exp\left[-j\,k\,\Delta z\left(\frac{n}{n_o} - 1\right)\right] E(x, y, 0). \tag{34}$$

Using the same split operator technique that was used in developing Equation (17)

$$E(x, y, \Delta z) = \exp\left(-\frac{j\,\Delta z}{4k}\nabla_\perp^2\right) \exp\left[-j\,k\,\Delta z\left(\frac{n}{n_o} - 1\right)\right] \exp\left(-\frac{j\,\Delta z}{4k}\nabla_\perp^2\right) E(x, y, 0)$$
$$+ O(\Delta z)^3, \tag{35}$$

where the same error term $O(\Delta z)^3$ used in Equation (17) is used here due to the commutation error of the transverse Laplacian. This expression is now seen to be almost identical to the split operator developed in Equation (17). The impact of the change in the lens parameter on optical structures is evaluated in subsequent sections. The only difference between the split operators of Equations (17) and (35) is a change in the lens term from

$$\exp\left[-\frac{j\,k\,\Delta z}{2}\left(\frac{n^2}{n_o^2} - 1\right)\right] \tag{36}$$

11

to

$$\exp\left[-j\,\Delta z\,k\left(\frac{n}{n_o}-1\right)\right].$$ (37)

However, it must be noted that approximations were made in deriving both equations (30) and (33). Subsequently, the Fresnel approximation leading to Equation (17) is used as the primary algorithm in this analysis.

3. Effective Index Method

One of the main objectives of this thesis was to develop and analyze the applicability of a fast, efficient BPM algorithm that is adaptable to varying structures. The first step in this process is to reduce the three-dimensional optical structure that is to be analyzed to a two-dimensional structure. Analyzing Equation (18) it is readily apparent that a two-dimensional ($M \times N$) point FFT must be carried out for each propagation step over the axial distance $\Delta z/2$. Assuming an effective step index change in the guiding structure allows the overall device to be reduced to one transverse component in x, so that the refractive index can be written as

$$n(x) = n_o + \delta n \cdot rect\left(\frac{x - x_o}{w}\right),$$ (38)

where $\delta n \equiv n_g - n_o$ is the index difference between the waveguide and the substrate and w is the width of the waveguide [3]. This obviously results in a reduction of M FFT's for each propagation step over a potentially long structure.

Implementing a one-dimensional cross-section results in a reduction of Equation (17) to

$$\mathbf{E}'(x, \Delta z) = \exp\left(-\frac{j\,\Delta z}{4\,k}\frac{\partial^2}{\partial x^2}\right)\exp\left(-\frac{j\,\Delta z\,k}{2}\left(\frac{n^2}{n_o^2}-1\right)\right)\exp\left(-\frac{j\,\Delta z}{4\,k}\frac{\partial^2}{\partial x^2}\right)\mathbf{E}'(x, y, 0)$$
$$+ O(\Delta z)^3,$$ (39)

12

and a reduction of Equation (18) to

$$\mathbf{E}'(x,z) = \sum_{m=-N/2+1}^{N/2} E_m'(z) \exp\left[j\left(\frac{2\pi mx}{L}\right)\right], \tag{40}$$

where L is the width of the computational grid in the transverse x direction. The number of gridpoints N must be determined based on physical constraints of the optical system. The number of grid points and therefore the transverse sampling interval Δx are determined for each structure and are developed in their respective sections.

The same concept that was used to propagate the three-dimensional solution is used on the two-dimensional solution. If the propagation term

$$\exp\left(-\frac{j\Delta z}{4k}\frac{\partial^2}{\partial x^2}\right) \tag{41}$$

of Equation (37) operates on the Fourier series representation of Equation (38) the result is that

$$E'_m(z + \Delta z/2) = E'_m(z)\exp\left[\frac{j\Delta z}{4k}\left(\frac{2\pi m}{L}\right)^2\right]. \tag{42}$$

Once again, this technique allows the field to propagate forward by calculating new Fourier coefficients based on a spatial frequency propagator

$$\exp\left[\frac{j\Delta z}{4k}\left(\frac{2\pi m}{L}\right)^2\right]. \tag{43}$$

One of the major contributions of this algorithm was developed at this point. Noting that the spatial frequency propagator depends upon physical parameters of the system, but not on the lens structure, the propagator can be determined at the initial stage and stored as a propagator array. If the propagator is predetermined it reduces the number of FFT's required in the two-dimensional structure by the number of propagation steps in the overall structure. The total number of steps in an optical

13

structure is typically on the order of several thousand steps, as is shown in the analysis performed in subsequent sections.

4. Algorithm Implementation

a. Absorption Window

The optical devices analyzed in this thesis are modeled using a step index profile, as mentioned previously. The step index profile is potentially problematic due to the discontinuities in the lens structure [3]. These discontinuities in the index profile excite spurious high spatial frequencies (i.e., radiation modes, and therefore energy leakage) when the BPM analysis is carried out [5]. The optical devices analyzed are primarily interferometers, but also include variations of Y-junction power dividers (YPD's). Interferometers inherently incorporate various branches in the guiding structures, as will be shown. These junctions and branches contribute significantly to the overall radiation losses of the device, and are therefore a major source of energy leakage.

Due to the periodic nature of the Fourier transform and the finite structure of the system, as these radiation modes propagate to the edge of the computational window in the transverse plane, they are folded back to the opposite edge of the window in subsequent propagation steps. This energy is seen as high frequency noise and may cause high frequency numerical instabilities [5] depending on the physical system being modeled. To avoid this potential problem, the radiation modes are absorbed at the edge of the window. This is seen as a valid approach since the radiation loss itself is calculated by measuring the contained power in the guiding structure.

The absorption window is implemented using a gradual field absorber near the window boundaries given by [2, 6]

$$absorb(x) = \begin{cases} 1, & |x| \leq |x_a| \\ 1/2(1 + \cos[\pi(x - x_a)/(x_a - x_b)]), & |x_a| < |x| \leq |x_b| \\ 0, & |x_b| < |x| \leq |x_r| \end{cases} \quad (44)$$

where x_r is the coordinate of the grid boundary, x_a represents the inner edge of the absorber, and x_b is the outer edge. The parameters of the absorbing window must be chosen for each device independently to ensure the field is absorbed over a sufficiently large region while ensuring that the absorber itself does not interfere with the guided modes of the device.

Although the absorption window is tailored for each device, as mentioned earlier, a generic absorber utilizing Equation (44) is shown in Figure 2 for illustrative purposes. In the example in Figure 2, the parameters $x_a = 200$, $x_b = 255$, and $x_r = 256$ are used.

b. Transverse Sampling Interval

An additional problem introduced by discretizing an optical circuit is discovered in determining the transverse and axial sampling intervals. This problem is of course compounded when attempting to implement a discontinuity such as a step index profile. Five factors must be considered [3, 5] when determining the transverse sampling interval Δx: (1) the size of the FFT window, (2) the range of the field's angular spectrum, (3) computer limitations, (4) the tolerable trapezoidal distortion of the step index caused
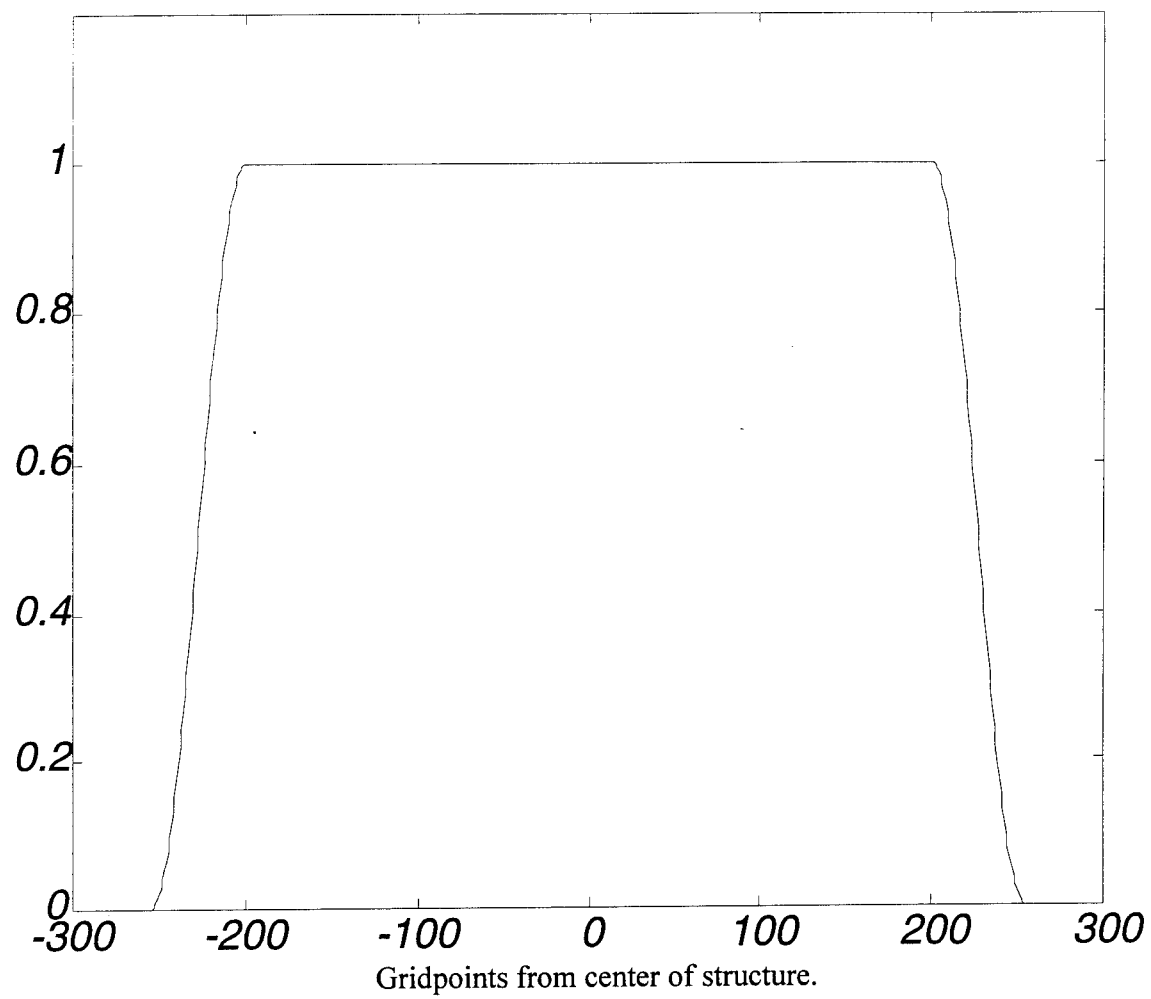
15

Figure 2. Typical absorption window.

16

by the finite grid, and (5) the tolerable index boundaries location uncertainty, also due to the discrete nature of the grid.

The first parameter determined is the window size W, which represents the physical dimension of the system being modeled. The window size must include the entire optical structure and must allow sufficient distance for decay of the evanescent fields and the absorption window. Since the window is dependent upon the specific system, W and therefore Δx must be determined separately for each device.

The propagation of the light in the waveguide is considered to be paraxial since the direction of propagation is predominantly forward. The physical spectral range is chosen to be that which corresponds to propagation within $|\theta| \leq \pi/4$ of the optical (z) axis. Utilizing this limitation on the spectral range, the highest angular frequency to be represented by the grid is given by [3, 5]

$$K_x = k \, \sin(\pi/4), \tag{45}$$

where k is given by Equation (3). However, the highest angular frequency that can be represented by an FFT with N points is given by

$$k_x^{FFT} = \left(\frac{2\pi N}{2W} \right) \tag{46}$$

Due to the limitation of the FFT

$$K_x \leq k_x^{FFT} = \left(\frac{2\pi N}{2W} \right) \tag{47}$$

Therefore the number of gridpoints N should satisfy

$$N \geq \frac{2n_0 W}{\lambda} \sin(\pi/4). \tag{48}$$

17

For a given structure of window size W, the transverse sampling interval is readily found to be

$$\Delta x = \left(\frac{W}{N}\right), \tag{49}$$

and as previously noted, must be determined for each device modeled.

c. Axial Sampling Interval

As previously mentioned the split operator development includes an error due to the commutation error and conditions on the maximum axial sampling interval must be determined. For the BPM to be applicable, the following four conditions must be satisfied [3, 5, 7]:

$$\left(2\frac{\delta n}{n_o}\right)^2 + \left(\frac{s}{k}\right)^4 + 2\frac{\delta n}{n_o}\left(\frac{s}{k}\right)^2 + 2\frac{\delta n}{n_o}\left(\frac{p+s}{k}\right)^2 << 8\frac{\delta n}{n_o} + 4\left(\frac{s}{k}\right)^2, \tag{50}$$

$$\Delta z << \frac{8\pi}{k}\left\{\left[\left(\frac{s}{k}\right)^2 + \frac{\delta n}{n_o}\right]^2 + 2\frac{\delta n}{n_o}\left(\frac{p+s}{k}\right)^2\right\}^{-1}, \tag{51}$$

$$\Delta z << \sqrt{12\frac{n_o}{\delta n}}\,(p+s)^{-1}, \tag{52}$$

$$\Delta z << 6k(p+s)^{-2}, \tag{53}$$

where δn is given in Equation (38) and s and p are the highest transverse spatial frequency components of the band-limited index profile and the propagating field, respectively. The Fourier transform of the step index profile defined by equation (38) is given as

$$\Im\{\delta n\ \text{rect}\,(x/w)\} = w\,\text{sinc}\,(wf_x), \tag{54}$$

18

where f_x is the angular frequency component. Since the majority of the *sinc* function's energy is contained within the first three lobes of the function (greater than 97%), p is taken to be the third zero crossing of the *sinc* function, so that

$$w \cdot f_{x_{0.97}} = 3 \tag{55}$$

or

$$p = \frac{(w \cdot f_{x_{0.97}})}{w} = \frac{3\pi}{w}. \tag{56}$$

Since the field distribution is much smoother than the index profile (due to the step index), we also take the value of p to be a more stringent requirement for s, so that

$$s = p \tag{57}$$

is a valid bound on s. Substituting the values of p and s into the applicability conditions of Equations (50) through (53), Equation (53) is found to be the most stringent and is subsequently used for determining the axial sampling distance Δz.

Now that a complete set of equations have been developed for the BPM algorithm and the expected limitations have been analyzed for general optical systems, the next step is to develop a practical implementation for the modeling system.

III. BPM IMPLEMENTATION OF A SINGLE SYMMETRIC MACH-ZEHNDER INTERFEROMETER

A. ARCHITECTURE OF THE MACH-ZEHNDER INTERFEROMETER

The architecture for the first system modeled is shown schematically in Figure 3 and consists of a single MZI with equal path lengths (symmetric) and Y-power dividers and combiners. The corresponding parameters are shown in Table 1. The separation distance d_a between the branches of the interferometer is varied by changing the length of *L2* and by changing the branching angle α. The index of refraction for the step index waveguide is given by Equation (38), where n_o = 2.2 is the LiNbO$_3$ substrate index and the static index difference between the waveguide and substrate δn = 5.1×10^{-3}. The input waveguide has a width of w_I = 3.0 μm and the maximum guide width in the YPD is given by w_o = 5.61 μm. The branching angle α is initially set at 1°, but is subsequently varied in the analysis in order to quantify the impact of branching angles on radiation losses.

1. Linear Electrooptic Effect

The linear electrooptic (Pockels) effect provides a change in the refractive index proportional to the applied electric field, which for LiNbO$_3$ corresponds to [8]

$$\Delta n_g = -\left(\frac{n_g^3 \, r_{33}}{2}\right) E, \tag{58}$$

where the electrooptic tensor element r_{33} = 30.8 $\times$ 10^{-12} (m/V). A typical electrode configuration [8] for an integrated optic device is shown in Figure 4. If a voltage V is applied to the electrode shown in Figure 4, the resultant electric field through the waveguide has an approximate magnitude of

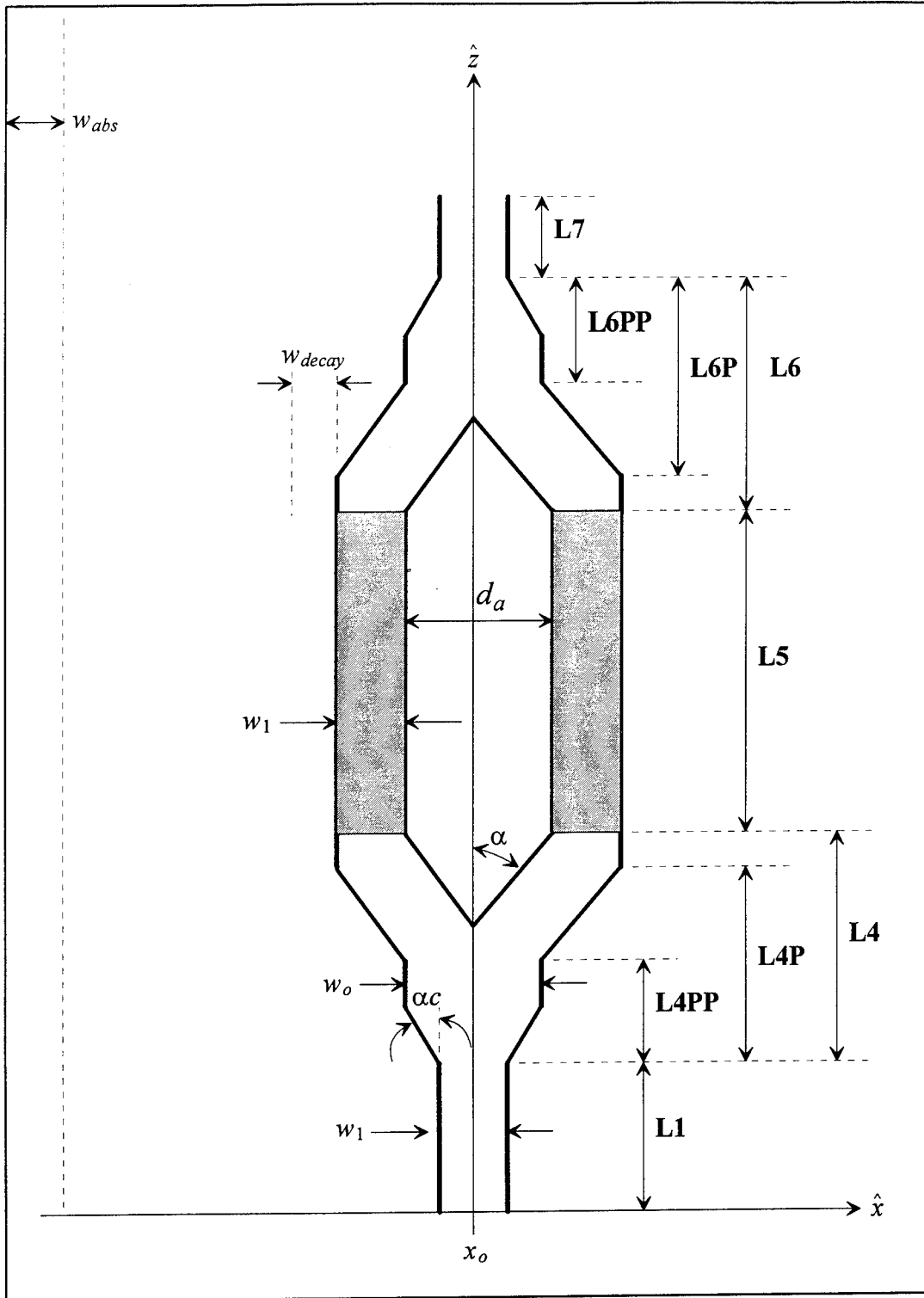$$|E| \cong \left(\frac{V}{G}\right), \tag{59}$$

21

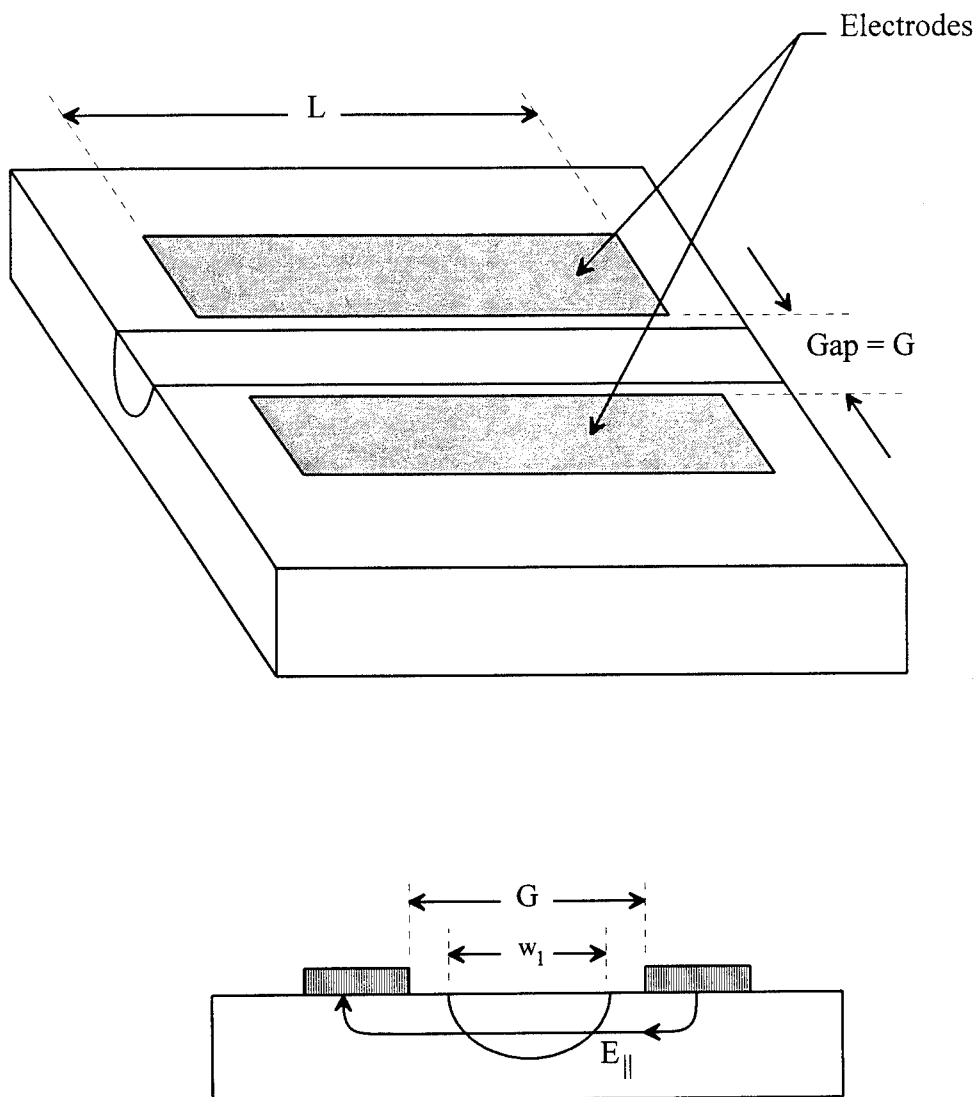Figure 3. Schematic diagram of a single symmetric Mach-Zehnder Interferometer.

Figure 4. Typical electrode configuration.

where G is the physical gap or separation between the electrodes, as shown in Figure 4.

However, neither the applied field nor the optical field is uniform. The effective electrooptically induced index change within a cross section of the waveguide is [8]

$$\Delta n_g(v) = -\frac{n_g^3 \, r_{33}}{2} \left(\frac{V}{G}\right) \Gamma, \tag{60}$$

where Γ is the overlap integral between the applied electric field and the optical field. Γ is defined as

$$\Gamma = \frac{G}{V} \iint E_{elec}(x, y) |E_{optical}(x, y)|^2 \, dx \, dy \tag{61}$$

w_1	3 µm
w_0	5.61 µm
d_a	20 µm
L1	12 µm
L4	$f(d_a)$
L5	1000 µm
L6	L4
L7	500 µm
αc	5°
α	1°

Table 1. Schematic parameter values.

For an electrode gap/mode width ratio of 1, the resultant overlap integral $\Gamma = 0.5$ [8]. The electrooptic effect can now be added to the lens equation for the region where electrodes are to be utilized, such as the $L5$ region of Figure 3. The total phase shift induced in the waveguide over the electrode length $L5$ is

$$\Delta\beta \, L_5 = -\frac{\pi \, n_g^3 \, r_{33}}{2} \left(\frac{V}{G}\right) \Gamma \left(\frac{L_5}{\lambda}\right). \tag{62}$$

24

If a push-pull configuration such as Figure 3 is utilized, the output intensity is given by [8]

$$P_o = \cos^2\left(\frac{\pi\, n_g^3\, r_{33}\, L_5\, \Gamma}{\lambda}\left(\frac{V}{G}\right)\right).$$ (63)

This gives an excellent theoretical prediction for the symmetric interferometer with which the BPM results can be compared. The theoretical output intensity of Equation (63) gives a prediction of the periodic output intensity that has a first null at

$$V_\pi = \frac{\lambda\, G}{2L_5\, \Gamma\, r_{33}\, n_g^3},$$ (64)

which for this device is calculated as

$$V_\pi = \frac{(900 \times 10^{-9})(3 \times 10^{-6})}{2(1000 \times 10^{-6})(0.5)(30.8 \times 10^{-12})(2.2)^3} = 8.17\,\text{V}.$$ (65)

This would produce a voltage folding period of approximately 16.34 V, which can be used to verify the accuracy of the BPM. However, Equation (63) does not take into account radiation losses due to branching angles or power dividers.

2. Structural Parameters

In developing structural parameters, and therefore BPM implementation parameters, the guidance or mode confinement characteristics of the waveguide must be considered. The guidance strength in a three-layer waveguide is determined by its normalized frequency V_n, defined by [5]

$$V_n = \frac{2\pi\, w}{\lambda}\sqrt{(2\, n_o\, \delta n)}.$$ (66)

A higher V_n means stronger guidance and therefore better mode confinement. For a given V_n, a waveguide can support M guided modes, where

$$(M-1)\pi < V_n < M\pi.$$ (67)

25

For this device $\lambda = 0.9$ μm was used. Since n_o and δn have already been determined, the choice of w_1 determines V_n. In this analysis strong guidance with single mode operation was desired, therefore $w_1 = 3.0$ μm was chosen. This results in a normalized frequency $V_n = 3.137$, which provides single mode operation. The next step in implementation is to determine the overall grid size. The grid size is needed in Equation (40) for the spatial frequency propagator and is also utilized in Equation (46) when determining the transverse sampling interval. In the initial analysis, the arm separation distance d_a shown in Figure 4 is forced to be 20 μm by choosing the appropriate length for $L4$, with a fixed branching angle α. If an absorption window of 7 μm is implemented on each side of the grid and a radiation mode decay distance w_{decay} is chosen as 10 μm, we can determine an appropriate grid size as

$$W = d_a + 2\,w_1 + 2\,w_{decay} + 2\,w_{absorb} = 60\,\mu m. \tag{68}$$

In this analysis the MZI structural parameters will be manipulated so an additional buffer of 20 μm is proposed to be added to Equation (68), resulting in $W = 80$ μm.

3. Sampling Interval

At this point, all of the information required to determine the transverse sampling interval Δx as given by Equations (48) and (49) is available. Since we know from Equation (48) that

$$N \geq \frac{2\,n_o\,W}{\lambda}\sin(\pi/4), \tag{69}$$

we therefore have

$$N \geq \frac{2(2.2)(80\,\mu m)}{900\,nm}\left(\frac{1}{\sqrt{2}}\right) = 276. \tag{70}$$

26

Since the algorithm is to be implemented using FFT's, as previously mentioned, this would require $N = 512$ for this circuit. Noting that $W = 80$ μm provides much more radiation mode decay distance than is required by Equation (68), if $W = 69.81$ μm is chosen, an additional 9.81 μm additional distance over the Equation (68) requirement is still provided, the significance of which will be shown directly. Applying $W = 69.81$ μm to Equation (69) we now have

$$N \geq 241, \tag{71}$$

so $N = 256$ is chosen. The significance of the relationship between N and W is shown by utilizing Equation (49), where

$$\Delta x = \left(\frac{69.81\,\mu m}{256} \right) = 0.2727\,\mu m. \tag{72}$$

Since the guide width must be implemented in discrete steps and has been chosen as 3.0 μm, we can determine the actual discrete guide width w_d by finding the number of grid steps

$$w_d = \left\lfloor \left(\frac{3.0\,\mu m}{\Delta x} \right) \right\rfloor \Delta x = 2.996\,\mu m, \tag{73}$$

where $\lfloor \ \rfloor$ denotes an integer value. This demonstrates the importance of choosing the correct relationship between W, N, Δx, w_i and w_d. As an example, if the grid size of $W = 60$ μm developed in Equation (68) had been used, then the result would be $\Delta x = 0.234$ μm and using Equation (73), $w_d = 2.8$ μm. This would reduce the guidance strength of the model structure. Therefore the parameters chosen for this analysis are: $N = 256$, $W = 69.81$ μm, and $\Delta x = 0.2727$ μm.

Since the guide width has been chosen to be 3.0 μm, and the discrete guide width w_d has been designed to be approximately 3.0 μm as well, the requirements for the axial sampling interval can now be determined. Solving Equation (56) we find

$$p = \left(\frac{3\pi}{3\,\mu m}\right) = \frac{\pi}{\mu m}, \tag{74}$$

and as noted in Equation (57), $p = s$. As previously noted, the most stringent criterion is given by Equation (53) so that

$$\Delta z \ll 2.4\,\mu m \tag{75}$$

In order to reduce computation time $\Delta z = 2.4$ μm is used in these simulations, which provides valid results when compared to the theoretically expected values. All of the structural parameters for the BPM implementation have now been developed. The last factor to be determined is the mode distribution of the optical input field.

B. SYMMETRIC EIGENFUNCTION INPUT

The input eigenfunction $u_n(x, z = 0)$ to the interferometer is computed analytically using an algorithm implemented in a C^{++} program. The normalized field distribution in the input waveguide is given by [3, 5]

$$u_n(x, z = 0) = \begin{cases} \cos(k_{10}\,x), & |x| \leq w_1/2 \\ \cos(k_{10}\,w_1/2)\exp[-k_{20}(|x| - w_1/2)], & |x| \geq w_1/2 \end{cases} \tag{76}$$

where

$$k_{10} = \left[\left(\frac{2\pi n_g}{\lambda}\right)^2 - \beta_o^2\right]^{1/2} \tag{77}$$

and

$$k_{20} = \left[\beta_o^2 - \left(\frac{2\pi n_g}{\lambda}\right)^2\right]^{1/2}. \tag{78}$$

28

The fundamental mode eigenvalue β_o is extracted from the transcendental eigenvalue equation

$$\tan\left(k_{10}\frac{w_1}{2}\right) = \frac{k_{20}}{k_{10}} \qquad (79)$$

For the 3.0 μm waveguide used in this analysis $\beta_o = 15381674$ cm^{-1}. The input field that is to be launched in the BPM algorithm is calculated numerically. Figure 5 depicts the symmetrical mode eigenfunction that is launched into the guiding structure.

C. BPM IMPLEMENTATION

1. Program Structure and Implementation

Now that all of the parameters of the BPM algorithm have been determined, the structure to be simulated has been chosen and the input field has been selected, the final step is to implement and demonstrate the BPM. A detailed flow diagram of the BPM algorithm is shown in Figure 6. As mentioned previously, one of the key contributions of this thesis was the reduction in computational time produced by implementing a global propagator. Since the propagator is applied in the spatial frequency domain, an analysis of the optical field in the frequency domain provides invaluable insight into the operation. The optical field is stored in an array during each propagation step along the optical axis and the FFT is applied to the optical field. The Fourier transform of the optical field demonstrates the symmetry that is intuitively expected and is shown in Figure 7. Another major reduction in computation time is achieved by noting the effect of this symmetry of the Fourier transform. If the propagator array is prefolded then it can be directly multiplied by the optical field in the frequency domain, eliminating the need for bit
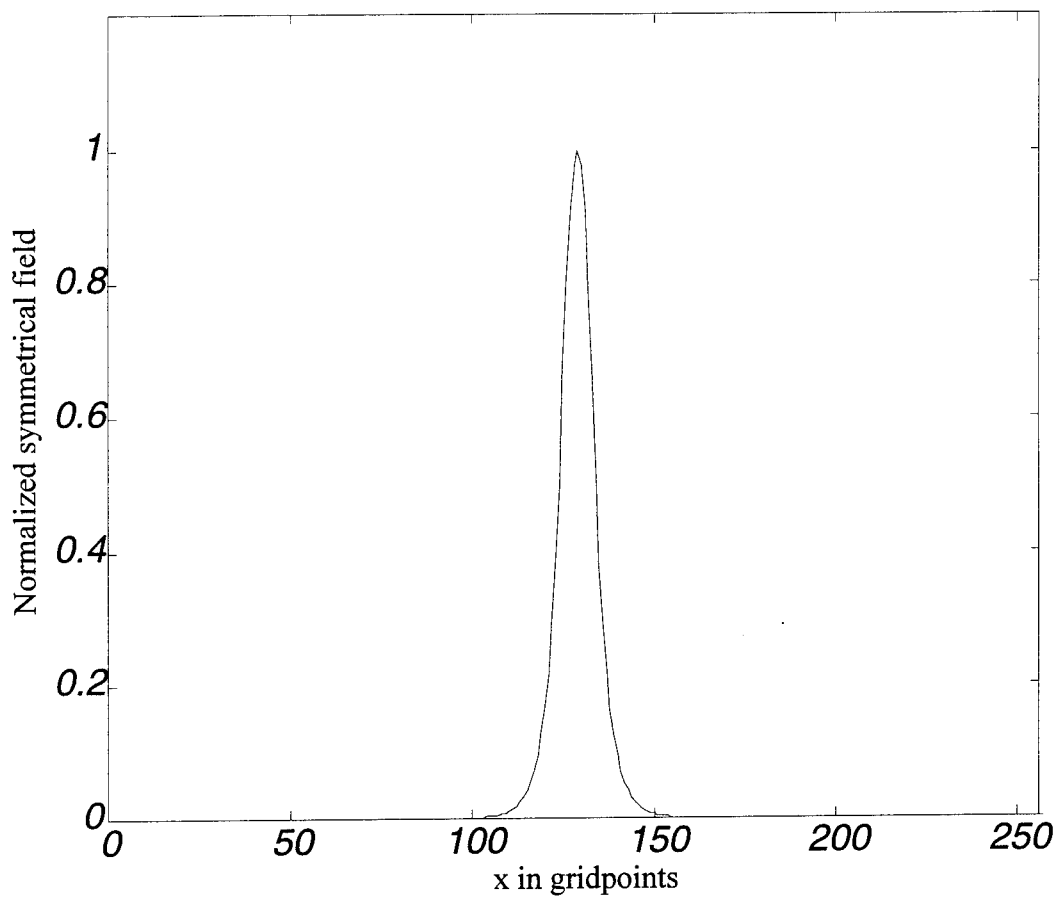
29

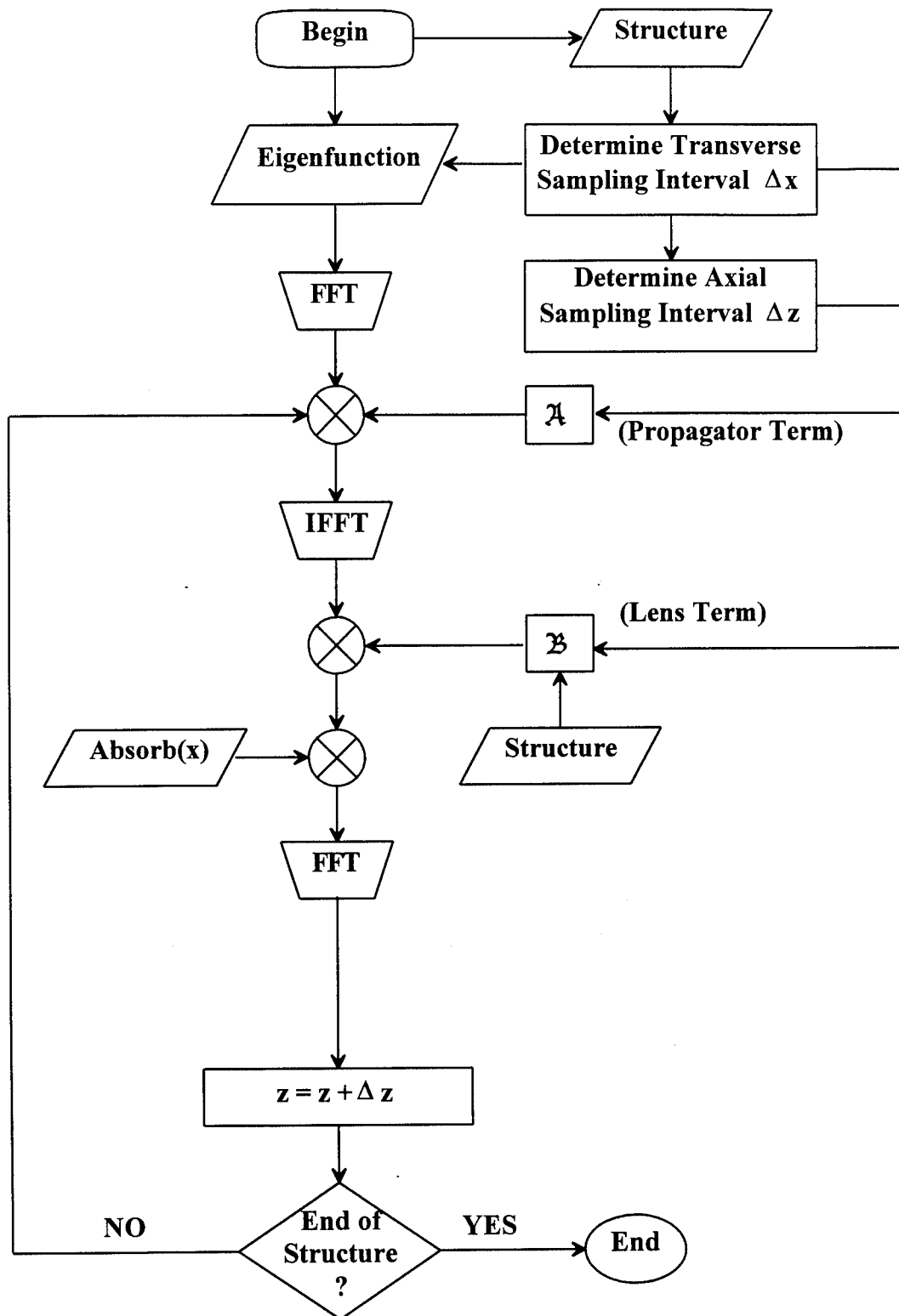Figure 5. Normalized symmetric eigenfunction input.
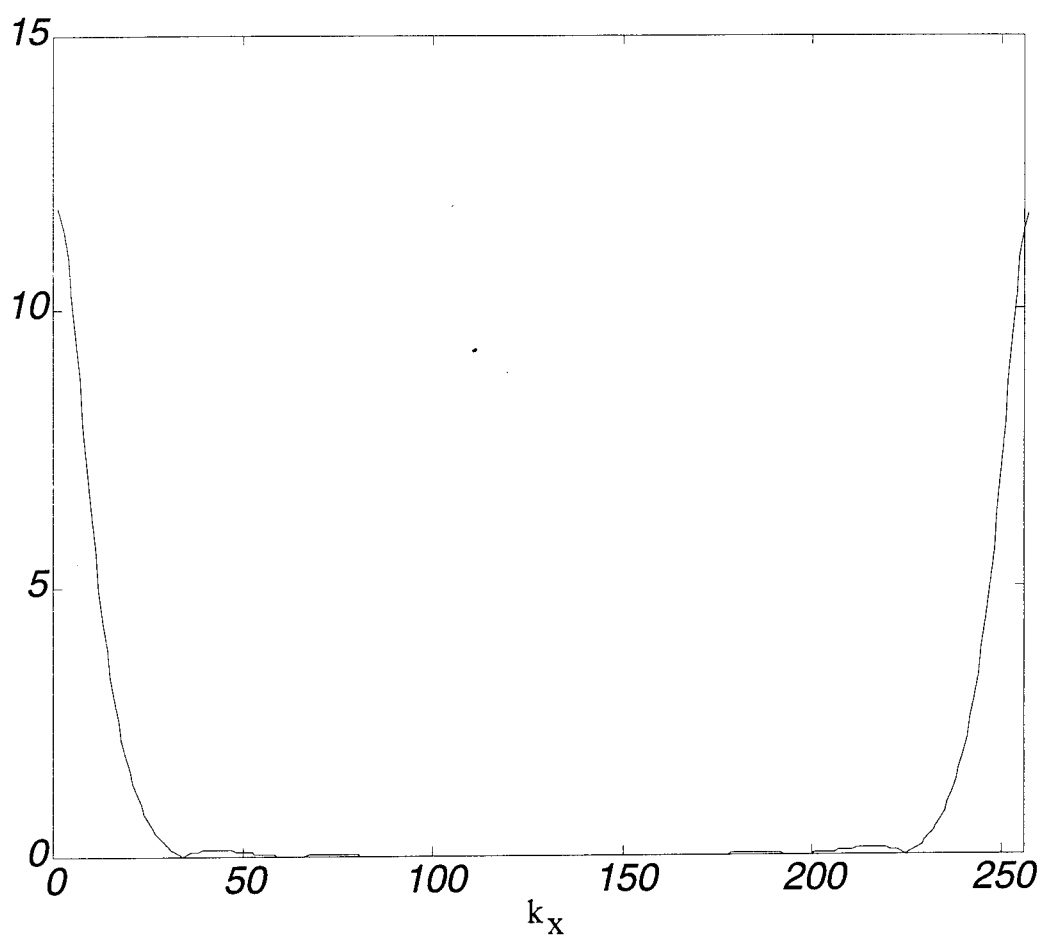
Figure 6. Detailed BPM flow diagram.

31

Figure 7. Fourier transform of the symmetric eigenfunction input.

32

reversal during the propagation loop. The normal and prefolded complex propagators are shown in Figure 8(a) and 8(b) respectively.

The beam propagation method of analysis provides a convenient method of viewing the launched eigenfunction as it propagates down the optical structure. The BPM implementation of the guide structure shown in Figure 3 is detailed in Figure 9(a). To demonstrate the radiation modes being studied, Figure 9(b) details the magnitude of the optical field $|\mathbf{E}'(x,z)|$ as it propagates down the interferometer. The spacing between the arms of the MZI is $d_a = 20$ μm. From these figures the periodic radiation mode coupling between the arms of the interferometer is readily apparent. Figure 10 shows a cross-sectional view of the center of the interferometer superimposed upon a scaled model of the step index profile (for reference), and shows the mode distribution within each waveguide with 0 volts applied. A detailed view of the Y-power divider designed for this interferometer is shown in Figure 11. The BPM implementation of the index structure is shown in Figure 11(a) and the BPM calculated optical field distribution is shown propagating through the structure in Figure 11(b). A key insight into the mechanics of the MZI can be obtained by viewing the output characteristics. Figure 12 is a detailed view of the output power combiner for this device. The output characteristics are demonstrated in Figures 13(a) and 13(b), with 0 volts and 8.17 volts applied to the electrodes receptively. The theoretical null predicted by Equation (65) is verified through the demonstration in Figure 13(b). The impact of the modulation voltage is clearly demonstrated by viewing an instantaneous cross-section of the device. A cross-sectional
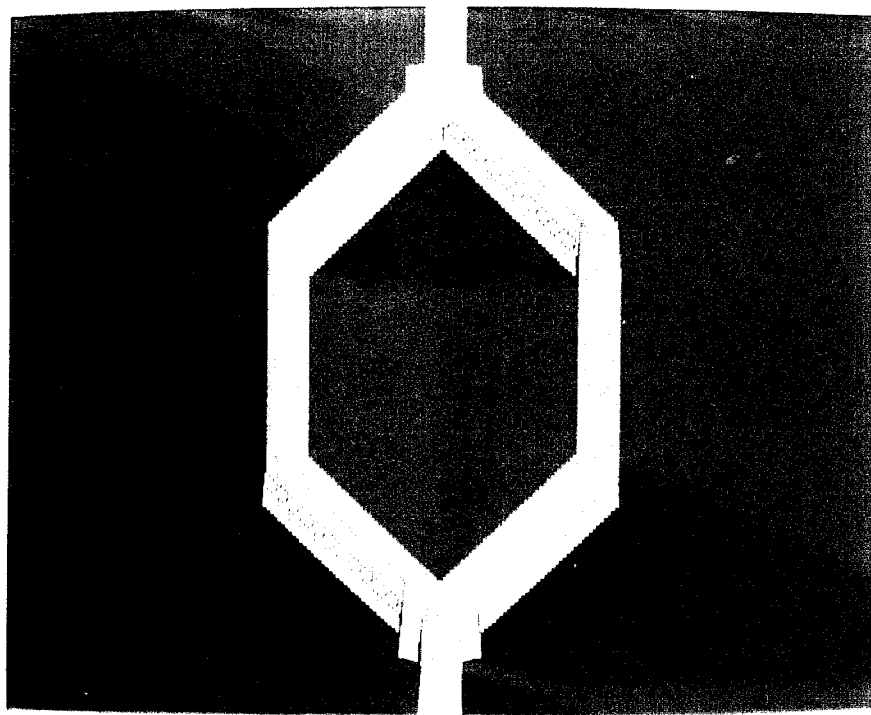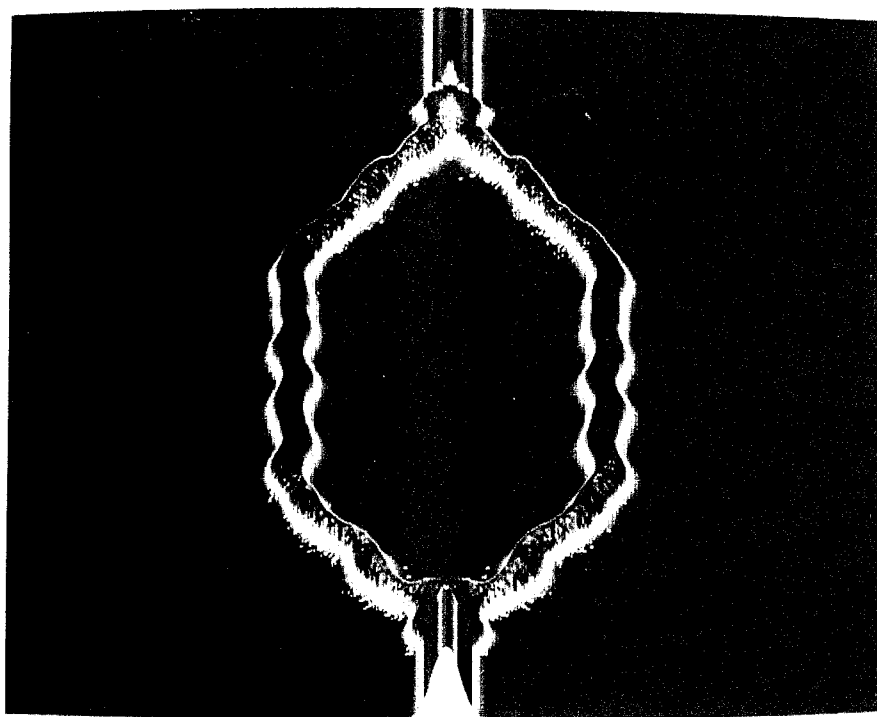
33
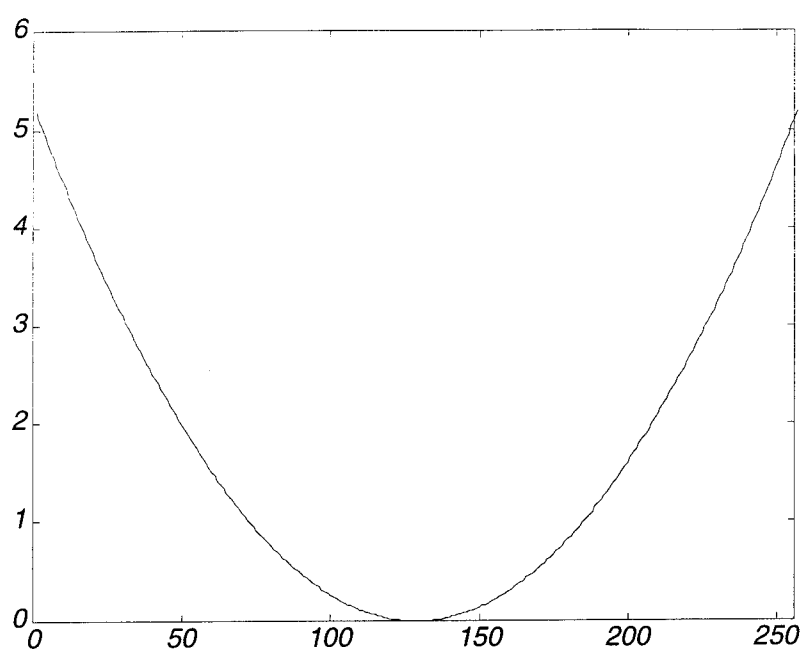
(a)
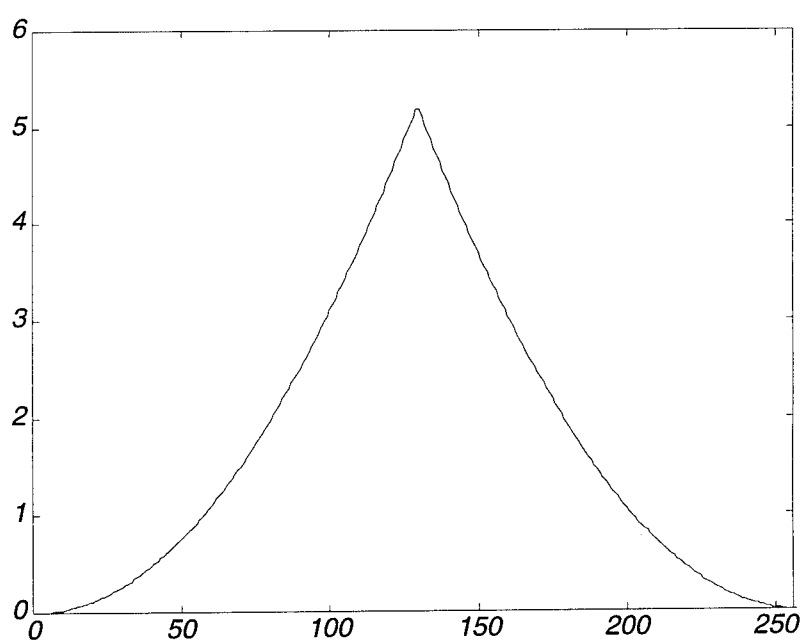
(b)

Figure 8. Global propagator: (a) normal; (b) prefolded.

34

(a)

(b)

Figure 9. Single symmetric MZI: (a) step index profile; (b) BPM analysis.
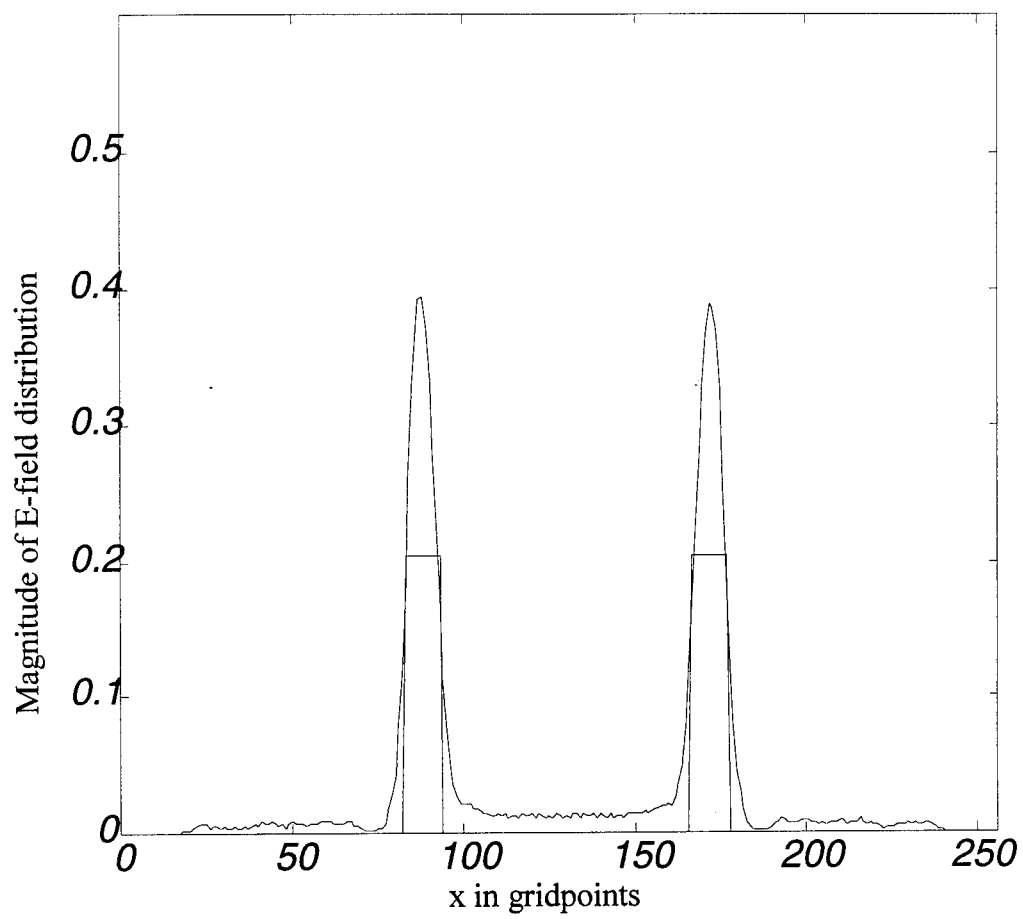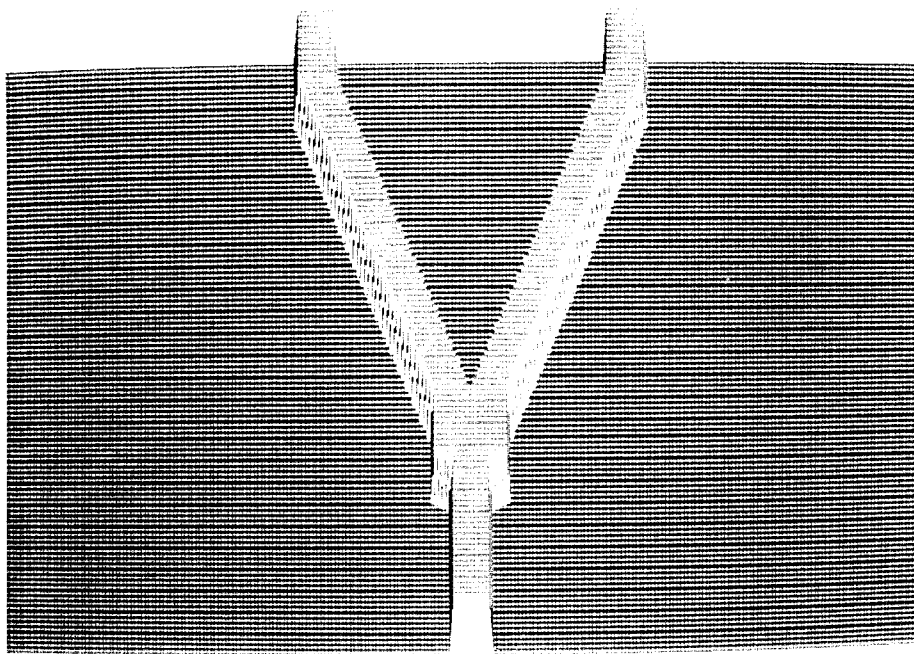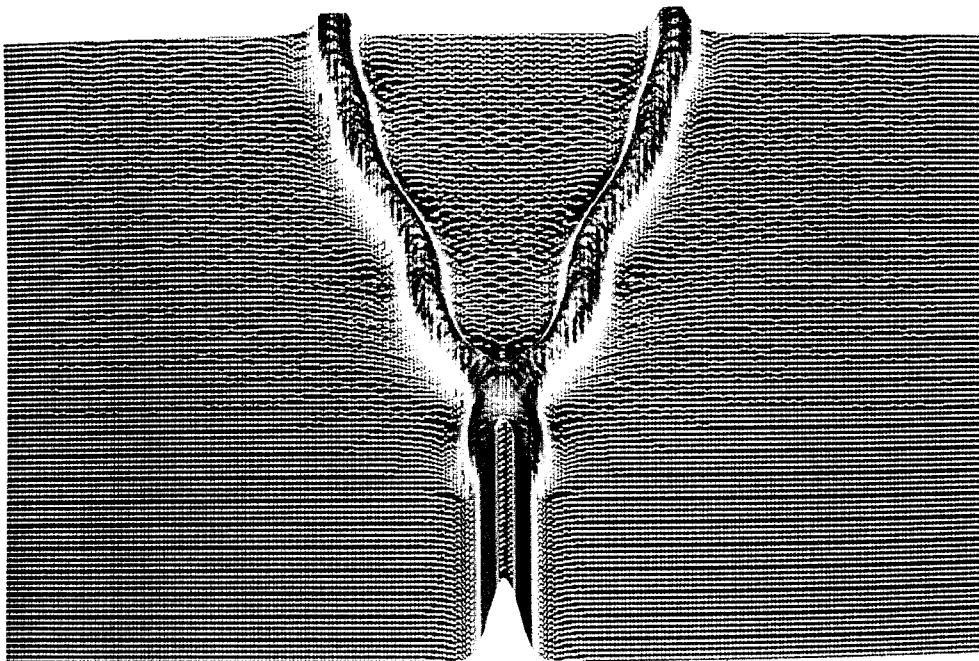
Figure 10. Cross-sectional view at the center of L5 with V = 0.

(a)

(b)

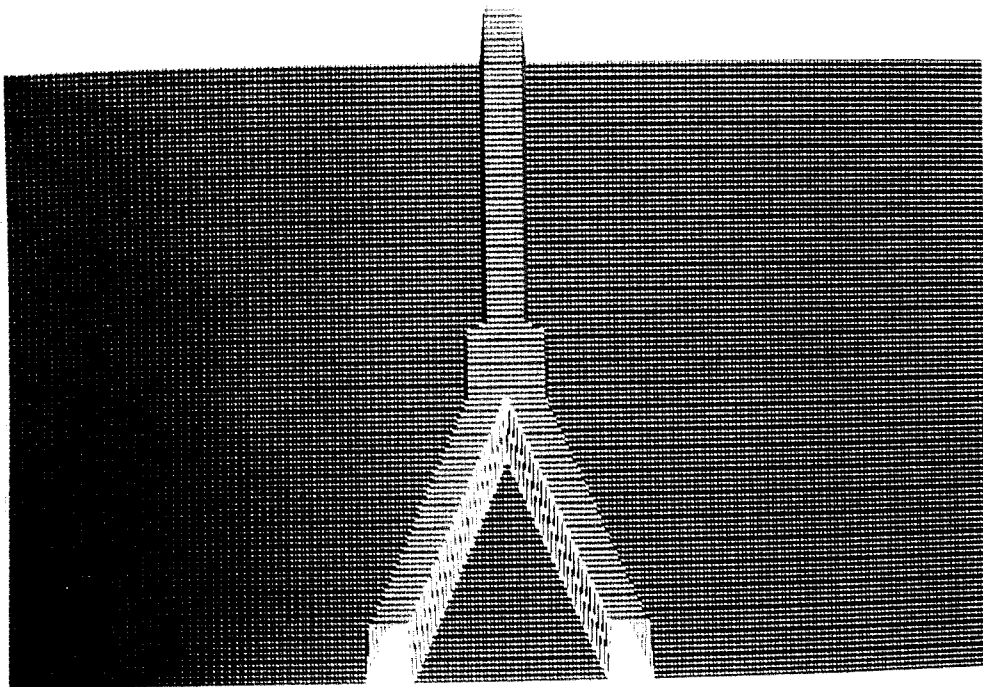Figure 11. Input YPD design analysis: (a) step index profile; (b) BPM analysis.
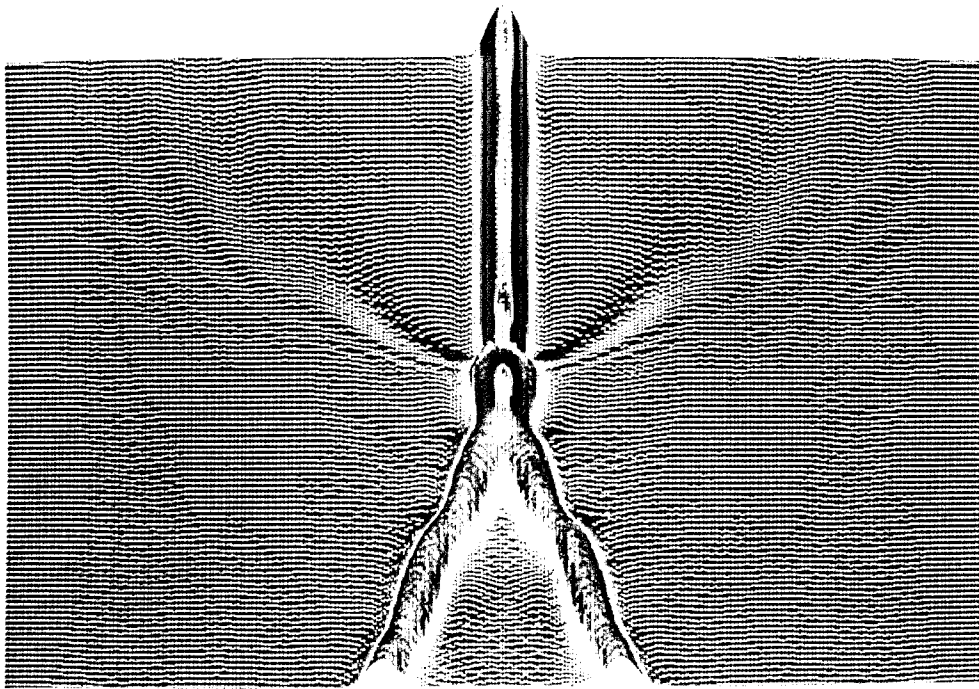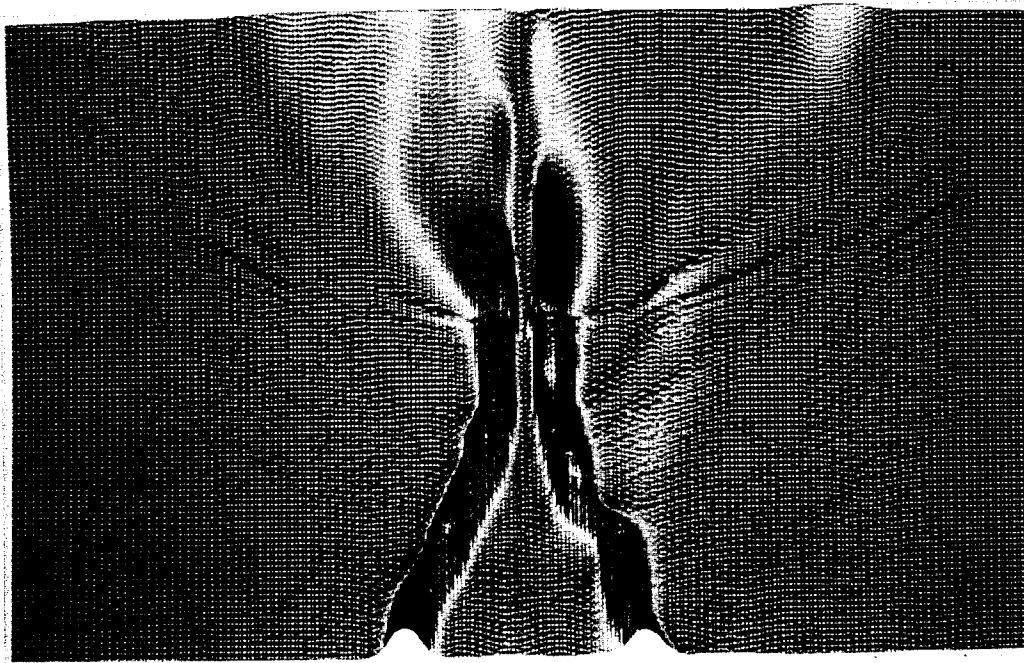
37

Figure 12. Output power combiner design: step index profile.

Figure 13. Output power combiner BPM analysis: (a) V = 0 volts; (b) V = 8.17 volts.

view of the output section *L7* is shown in Figure 14(a) and 14(b) for 0 volts and 8.17 volts applied. This view clearly shows the desired interference effect introduced by the modulating voltage

The BPM propagation algorithm is implemented in a C^{++} program. The implementation allows branching angles, structural lengths and electrode voltages to be input through external script files. This enables rapid assessment of the impact of changing design parameters on the overall device performance without recompiling. This gives the potential for a stand alone, platform independent design package. A typical flow chart of a BPM analysis showing the usual sequence of implementation and analysis is shown in Figure 15 As shown in Figure 15, once the eigenfunction is calculated for a specific structure it is stored for repeated analysis. A command line script file is utilized to provide structural or electrode voltage parameters so that detailed analysis of system performance can be performed without continual user input. A set of script files used for manipulating voltage and structure parameters for the devices in this thesis are shown in the Appendix.

2. Validity and Applicability of the BPM

The theoretical output intensity of the interferometer being modeled is given by Equation (63). Varying the electrode voltage from 0 to 20 volts and comparing the BPM output intensity to the theoretical intensity of Equation (63) gives a good analysis of the validity of the BPM. The BPM calculated output intensity is shown versus the theoretical output intensity in Figure 16. The 16.34 volt folding voltage predicted by Equation (65)

40
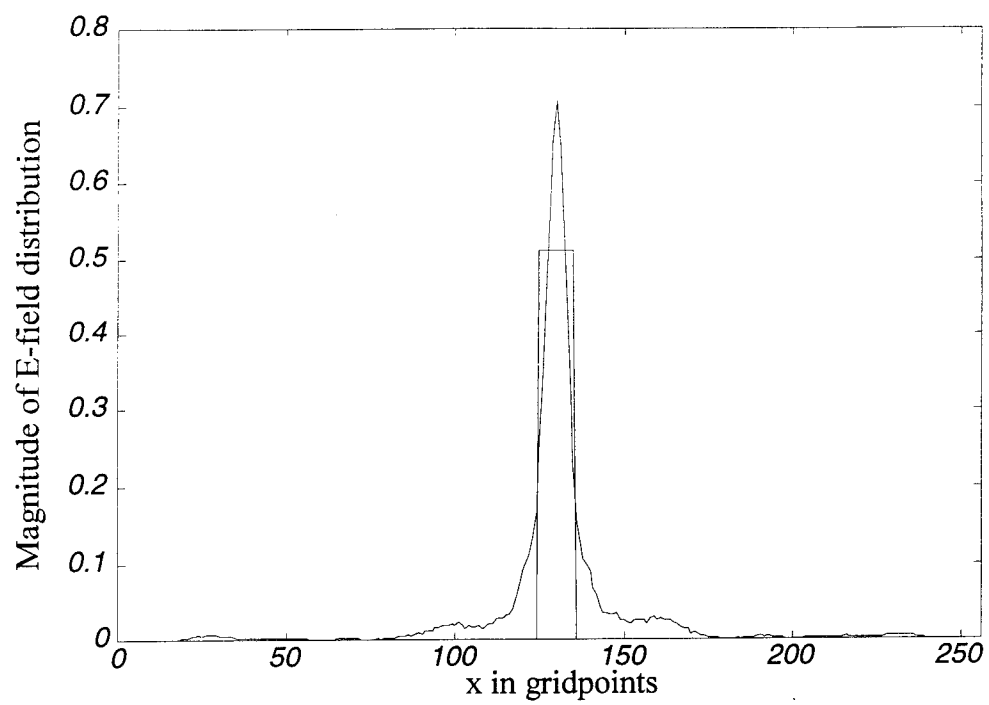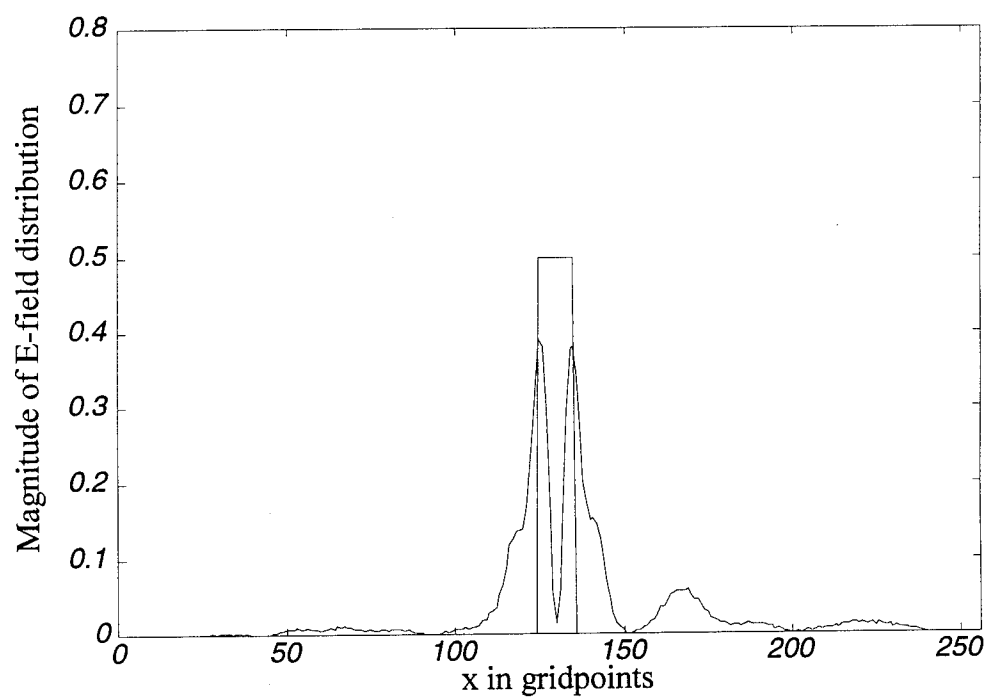
Figure 14. Cross-sectional view of the output: (a) V = 0; (b) V = 8.17.
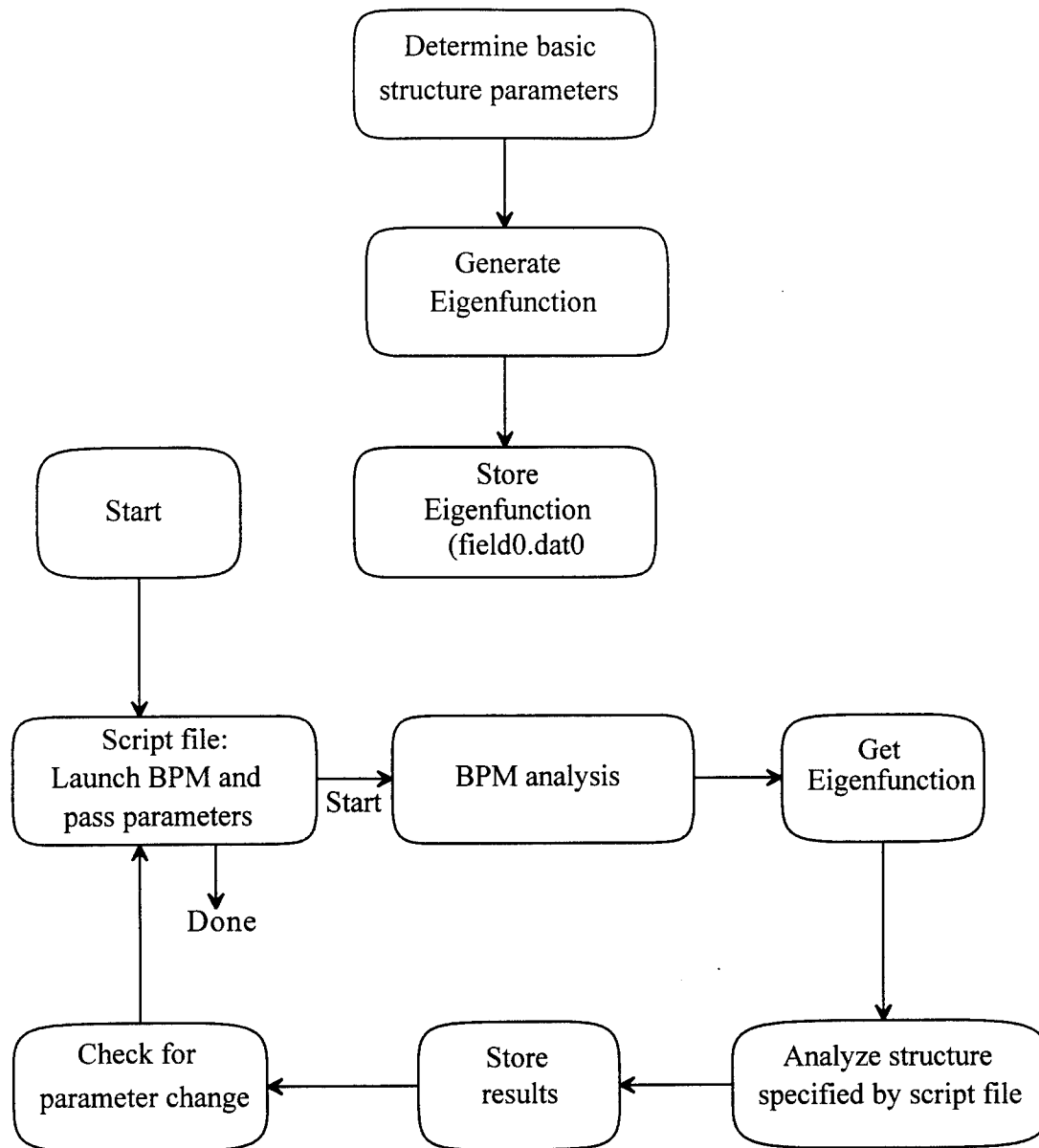
41

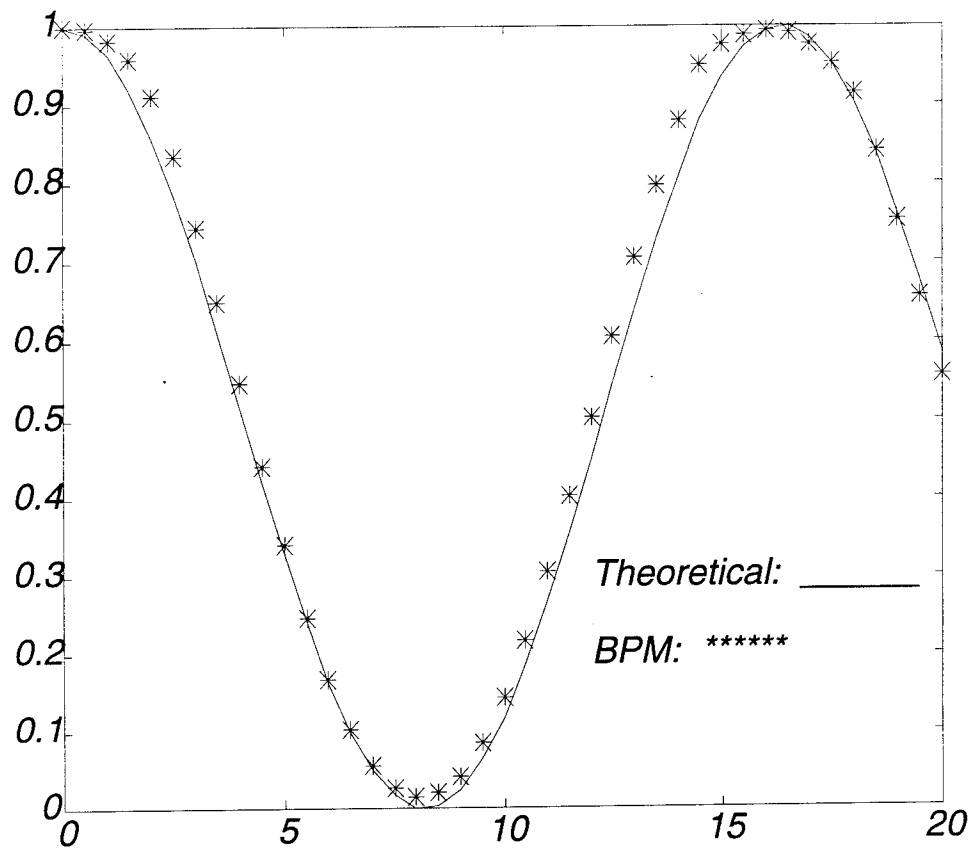Figure 15. Flow diagram of BPM analysis sequence.

Figure 16. Theoretical versus BPM calculated output intensity.

43

is in fact closely tracked by the BPM analysis. The results of Figure 16 imply that the BPM provides an accurate prediction of interferometer performance. The alternate lens equation developed in Equation (35) was also used to analyze the symmetric MZI. As demonstrated in Figure 17, the alternate lens equation has little effect on the analysis.

Design parameters of an MZI can have dramatic effects on optical device system performance, and can be easily modeled using the BPM. Varying the length of section *L4* in Figure 3, while holding the branching angles constant, changes the arm separation distance d_a. The impact on radiation mode losses and coupling can be significant. The radiation mode coupling with arm spacing $d_a = 5$ μm is shown in Figure 18, while the results shown in Figure 19 demonstrate the effect of increasing the spacing to $d_a = 10$ μm. It would seem that by increasing arm separation radiation mode coupling would be eliminated. However, a major problem in system design is performance optimization. As arm spacing is increased, so is the overall device length. The device length has a direct impact on loss, which is normally to be minimized. The overall device loss through the interferometer is calculated as

$$\text{Loss} = 10 \log \left(\frac{P_{out}}{P_{in}} \right). \tag{80}$$

The device loss for arm spacing $d_a = 5$ μm, 10 μm, and 20 μm was calculated as 1.6, 0.49, and 0.72 dB respectively. However, by reducing the splitting angle α of the device the loss can be reduced. The loss with α = 0.6 degrees was calculated for arm spacing $d_a = 5$ μm, 10 μm, and 20 μm as 0.7, 0.1, and 0.2 dB respectively. The effects of reducing the splitting angle on loss are clearly evident and the reduction in radiation mode coupling

44
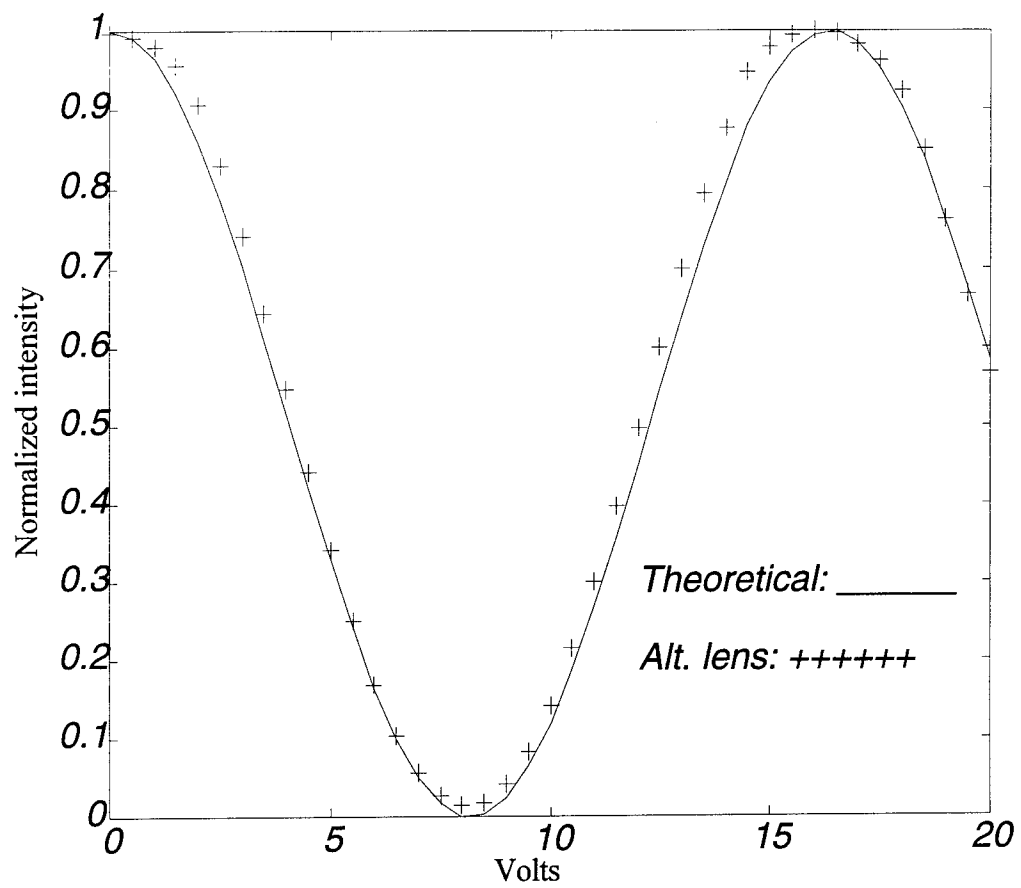
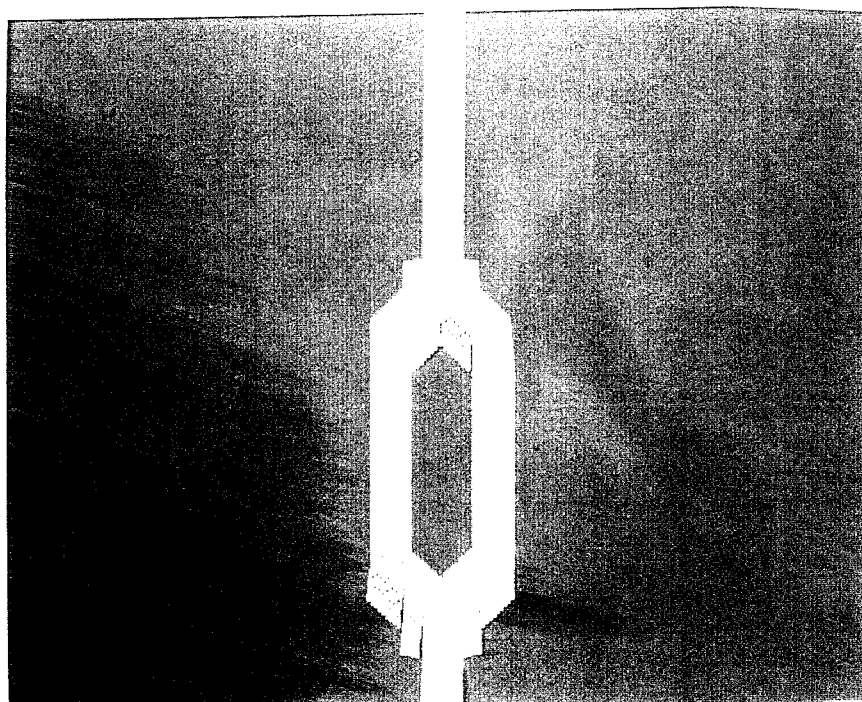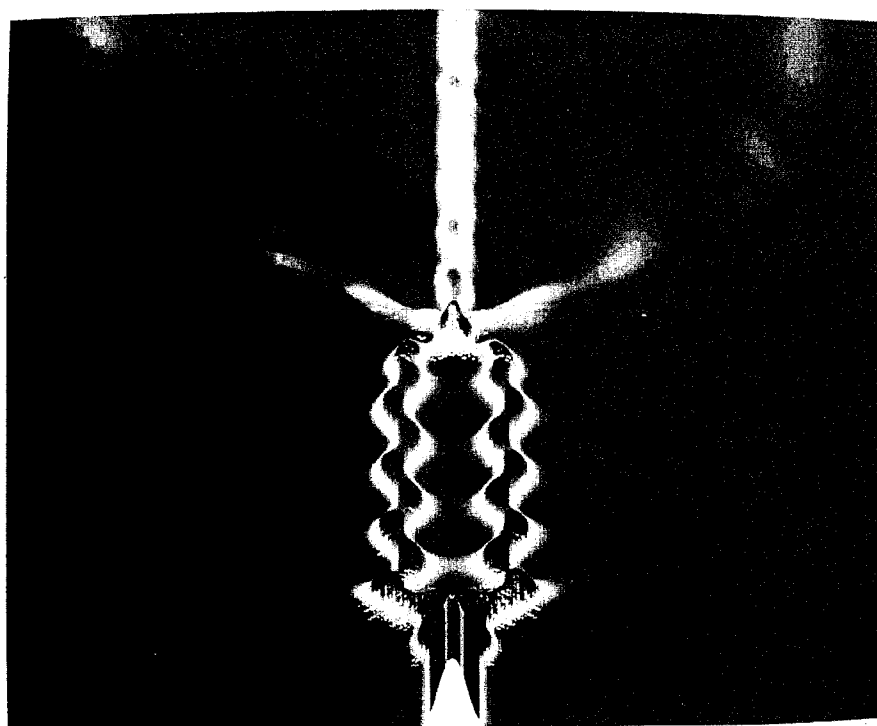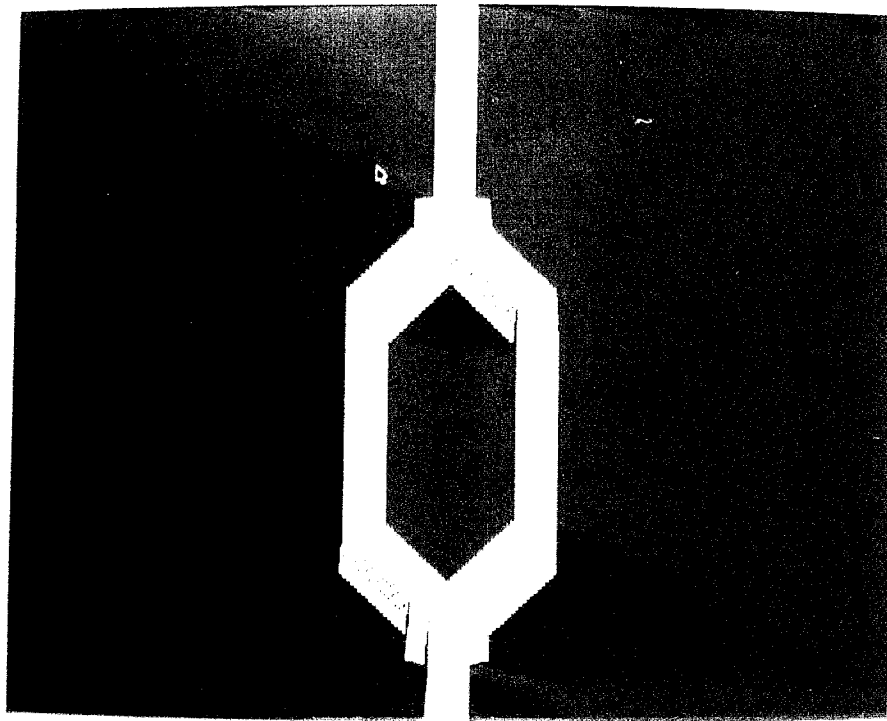Figure 17. Alternate lens equation analysis of output intensity.

Figure 18. MZI with spacing $d_a = 5$ μm: (a) step index profile; (b) BPM analysis.

(a)

(b)

Figure 19. MZI with spacing $d_a = 10$ μm: (a) step index profile; (b) BPM analysis.

can easily be seen utilizing the BPM. An analysis of the reduction in radiation mode coupling is shown in Figures 20, 21, and 22 for arm spacing $d_a = 5$ μm, 10 μm, and 20 μm respectively. The most notable difference is achieved for $d_a = 5$ μm; comparing Figure 18 to Figure 20 it is apparent that increasing branching angles has a dramatic effect on device loss due to the lack of energy containment at increased branching angles. The BPM is an excellent tool for minimizing these types of loss prior to fabrication.

The BPM has now been demonstrated as a viable tool for optical system design and has been validated through comparison of calculated results to theoretical predictions. However, as was noted previously, the theoretical prediction of Equation (63) does not include radiation losses and thus gives no indication of expected device loss, such as Equation (80).

(a)
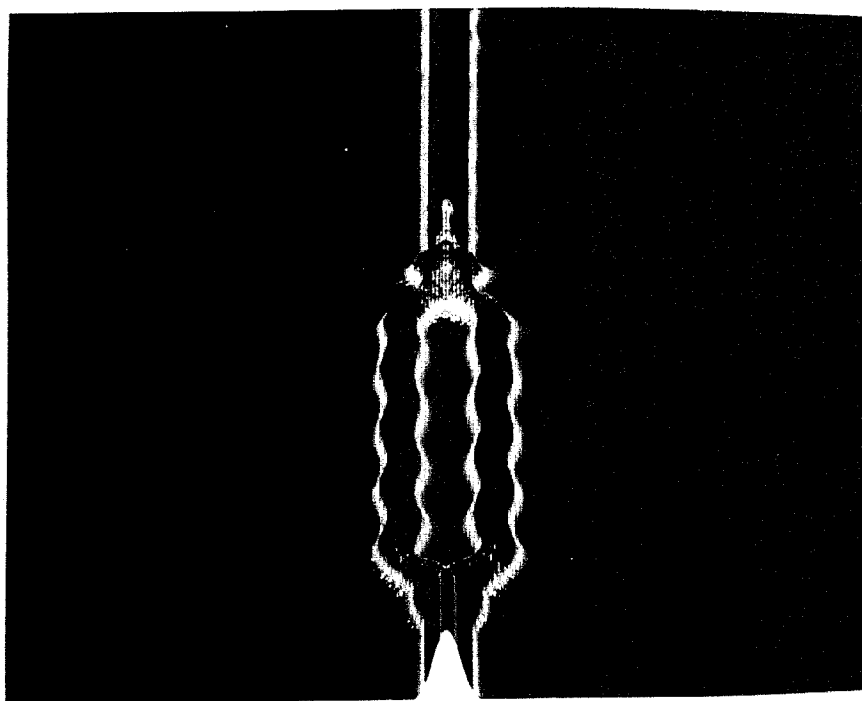
(b)

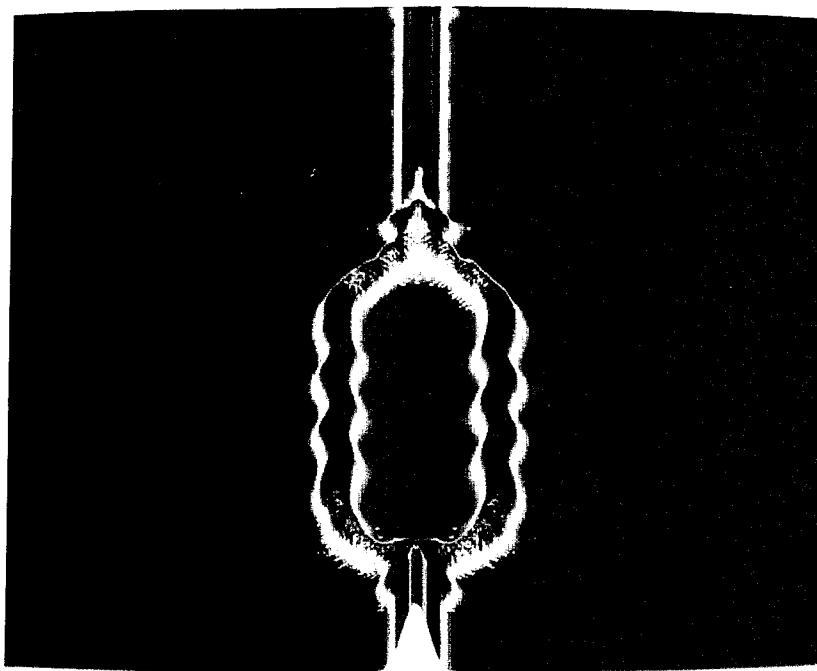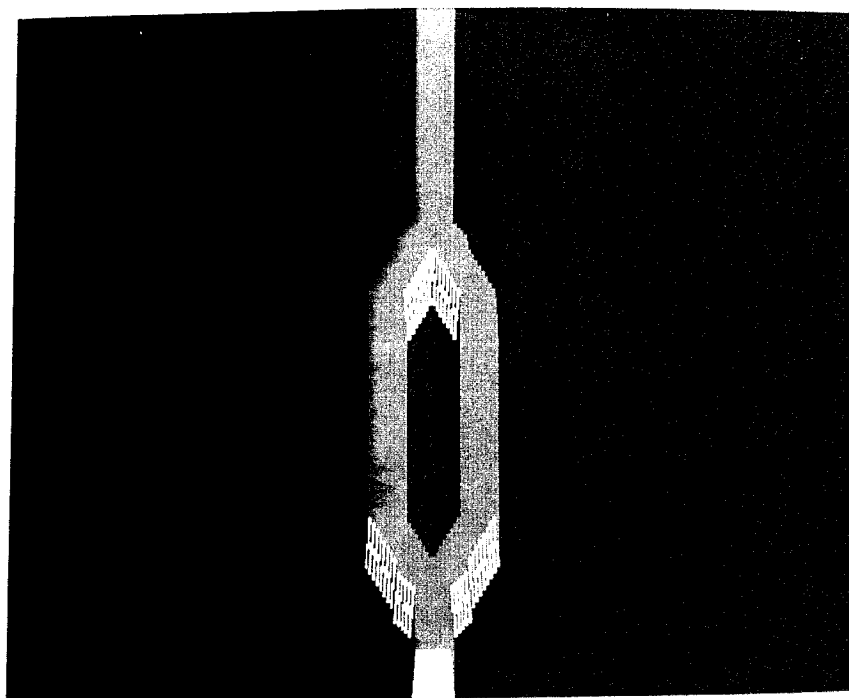Figure 20. MZI with spacing $d_a = 5\,\mu m$: (a) step index profile; (b) BPM analysis.

49

Figure 21. MZI with spacing $d_a = 10\ \mu$m: (a) step index profile; (b) BPM analysis.
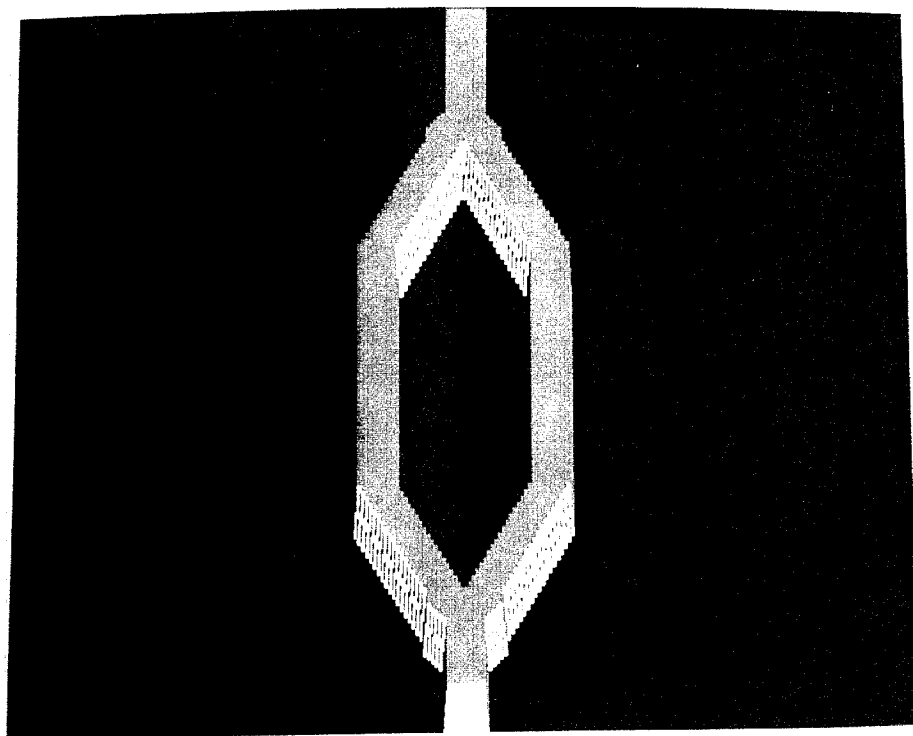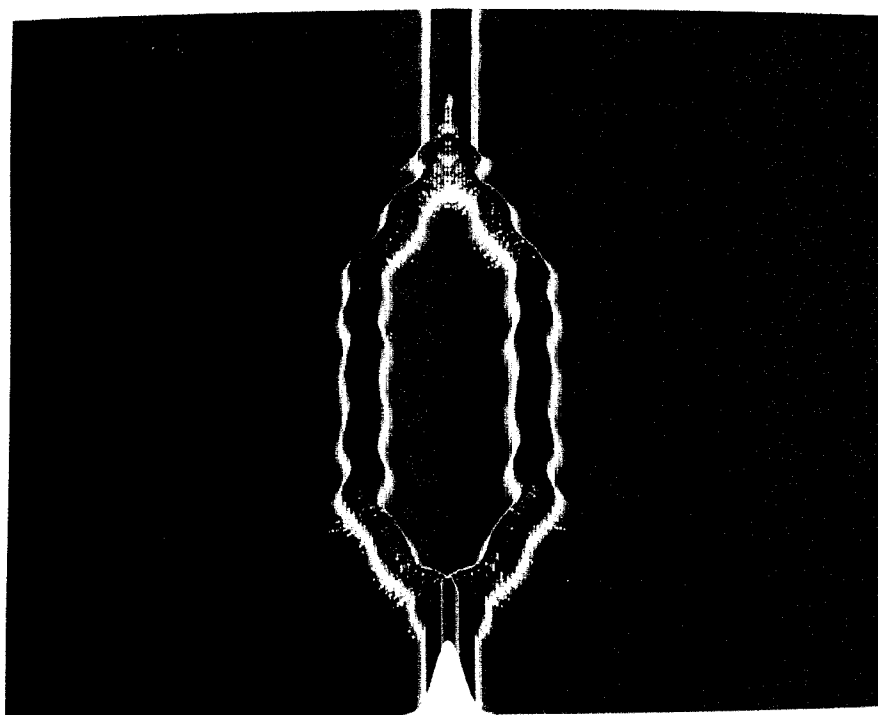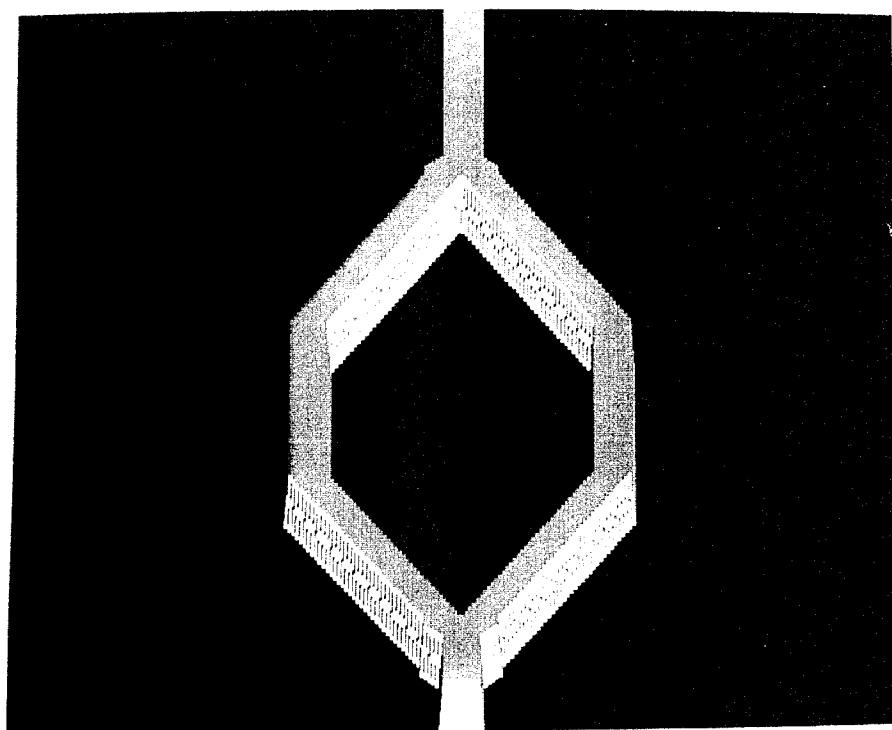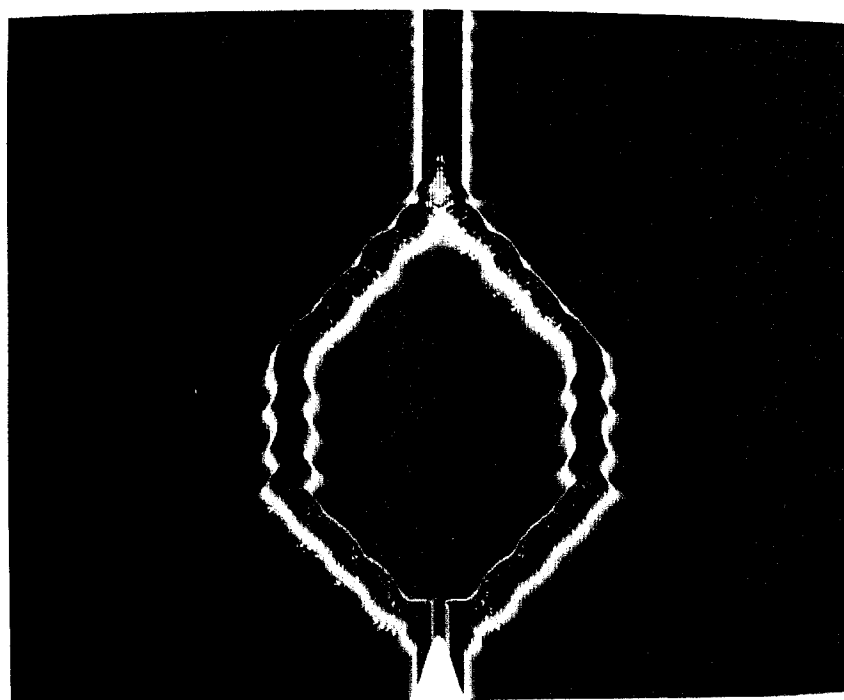
(a)

(b)

Figure 22. MZI with spacing $d_a = 20$ μm: (a) step index profile; (b) BPM analysis.

IV. SINGLE ASYMMETRIC MACH-ZEHNDER INTERFEROMETER

A. DEVICE PARAMETERS

A true test of the validity of the BPM is achieved through modeling a physical device that can be tested in the laboratory. An asymmetric Mach-Zehnder Interferometer fabricated by the Naval Research Laboratory [9] is used for this purpose. A schematic representation of the physical device, showing electrode placement, is shown in Figure 23. The representation used to develop the BPM implementation of the physical device is shown in Figure 24. The physical dimensions of the asymmetric device are given in Table 2. A major increase in computational time is intuitively expected from the overall device length of 21.96 mm compared to 1.32 mm for the symmetric device.

The first step in implementing the asymmetric structure is to once again determine the grid parameters. Since in this case a reverse engineering process is utilized, some flexibility would seem to be removed. However, the discrete guide width w_d must still match the physical guide width w_l. Using Equation (68) the overall grid width requirement is determined to be

$$W \geq 128 \ \mu m \tag{81}$$

However, using previously gained knowledge of the relationship between N, W and Δx, the grid size is chosen as $W = 139.264 \ \mu m$. Since this device was designed to operate at a wavelength of 1300 nm, the number of grid points is determined using Equation (69) so that

$$N \geq \frac{2(2.2)(139.264 \mu m)}{1300 nm} \frac{1}{\sqrt{2}} = 333 \tag{82}$$
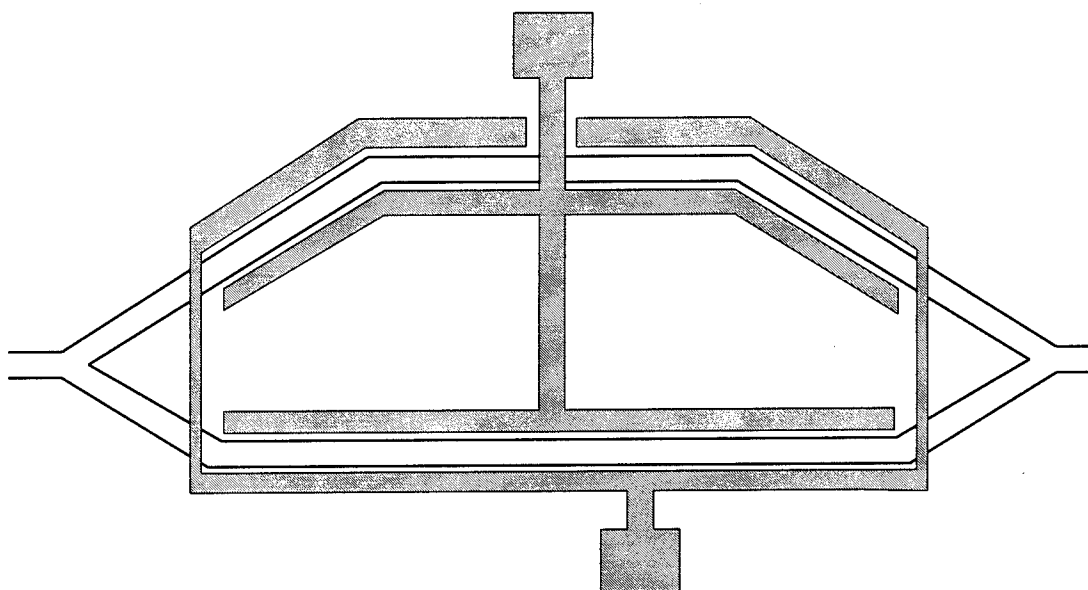
Figure 23. Asymmetric interferometer showing electrode placement.
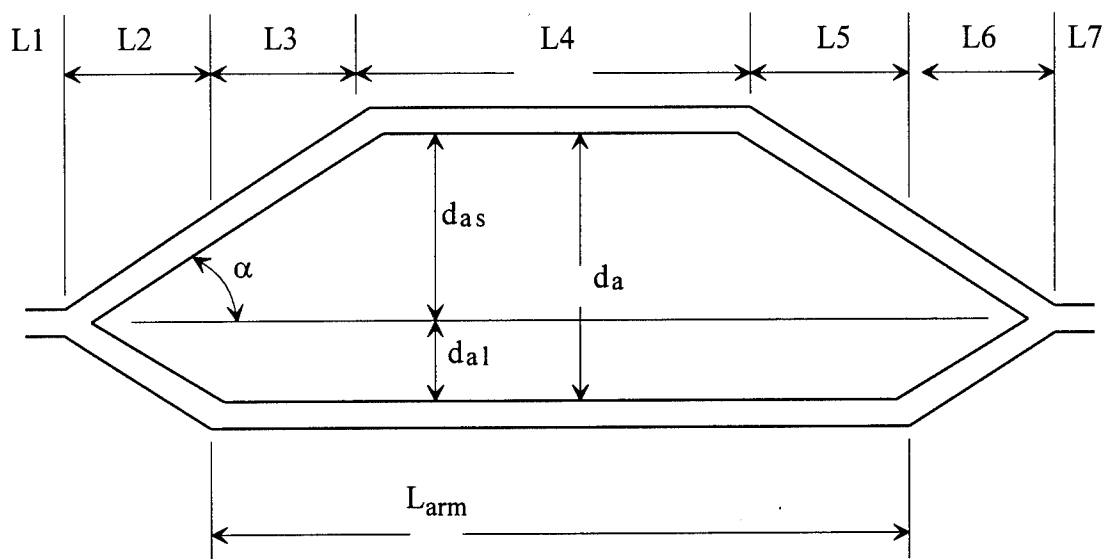
Figure 24. Schematic representation of an asymmetric interferometer.

Therefore, for the asymmetric interferometer we must choose $N = 512$ points. This results in a transverse sampling interval

$$\Delta x = 0.272 \ \mu m.$$

(83)

w_1	6.8 μm
d_a	80 μm
α	0.6°
L1	125 μm
L2	3170 μm
L3	1300 μm
L4	11.4 mm
Larm	14mm
L5	1300 μm
L6	3170 μm
L2	1500 μm
Total Length	21.96 mm

Table 2. Device parameters.

Since the guide width $w_1 = 6.8$ μm is given [9], the discrete guide width is now forced to be $w_d = 6.8$ μm as well. The discrete guide width is calculated from Equation (73) as

$$w_d = \left\lfloor \frac{6.5 \mu m}{\Delta x} \right\rfloor \Delta x = 6.8 \mu m$$

(84)

This is achieved by choosing the appropriate value for W in Equation (68). Although Equation (68) requires a minimum value for W, extra range can be added to ensure the correct desired discrete guide width, while minimizing N. An axial sampling interval of $\Delta z = 2.4$ μm is used in this simulation as well.

B. BPM IMPLEMENTATION

The BPM implementation of the physical structure is shown in Figure 25. The step index profile is shown in Figure 25(a), while Figure 25(b) shows the magnitude of the optical field as it propagates through the device with 0 volts applied to the electrodes. The asymmetric MZI shown in Figure 23 has an inherent difference in the interferometer arm lengths, ΔL, which gives rise to an intrinsic phase bias ϕ_o given by [9]

$$\phi_o = 2\pi\, n_{eff} \Delta L/\lambda, \tag{85}$$

where n_{eff} is the mode effective index. The BPM algorithm is implemented using the same basic flow diagram shown in Figure 6, utilizing the known physical parameters of the device [9].

The output characteristics of the physical device were recorded and are compared to the BPM analysis in Figure 26. This gives an excellent validation of the BPM methodology. However, device loss must still be addressed.

C. COUPLER DESIGN

The Y-power divider (YPD) of Figure 23 is notably different than the YPD of Figure 11. One of the main advantages of the BPM is the flexibility of implementing various design concepts rapidly and analyzing the effect. A more detailed view of the input YPD for the asymmetric device is shown in Figures 27. The BPM implementation of the YPD index profile is shown in Figure 27(a) and the optical field distribution is shown in Figure 27(b). The optical field interaction at the output combiner is of major interest, and effects the overall dive characteristics. Due to the inherent phase offset of
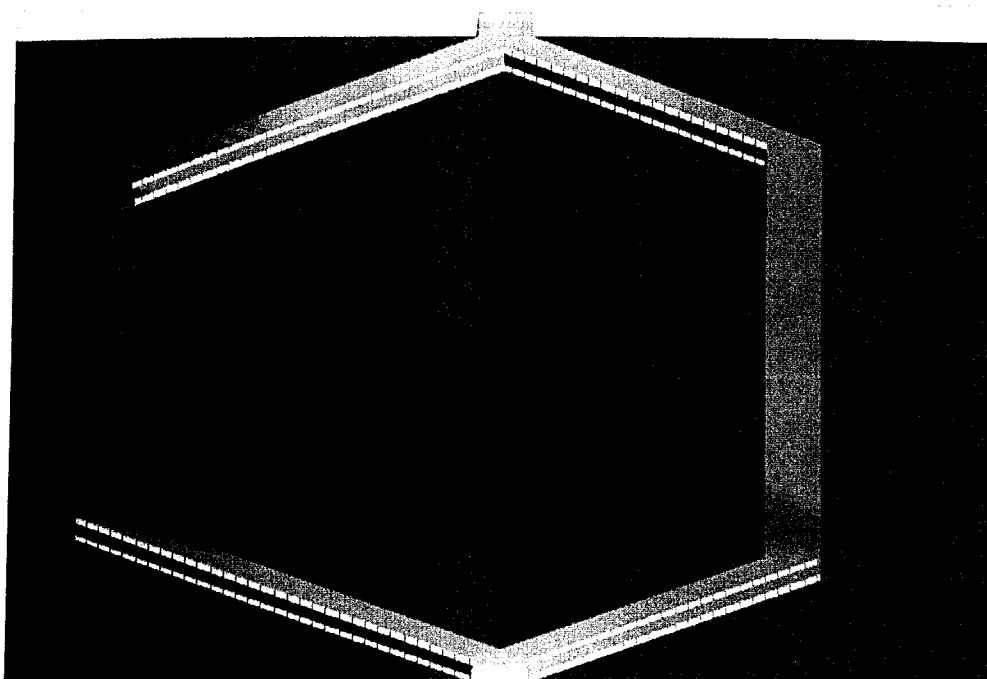
(a)
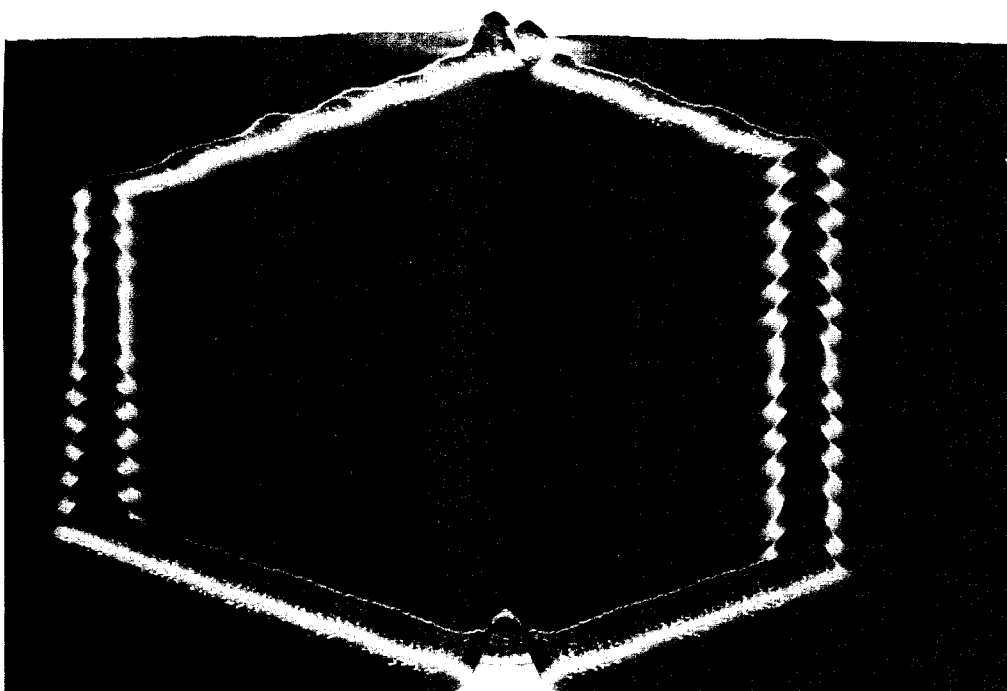
(b)

Figure 25. Single asymmetric MZI: (a) step index profile; (b) BPM analysis.

(a)

(b)

Figure 26. (a) Measured output intensity; (b) BPM calculated output.

59
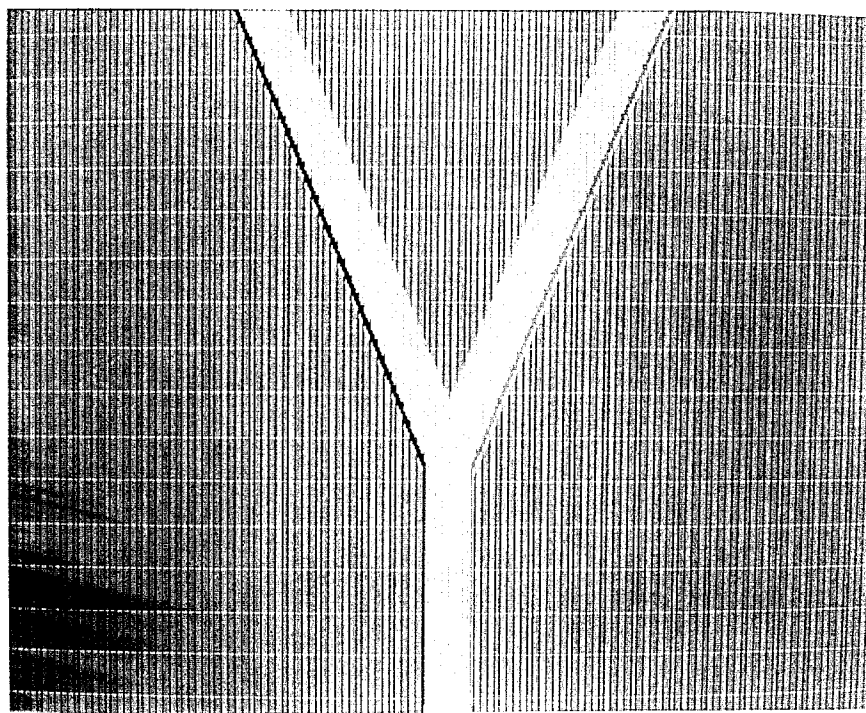
(a)
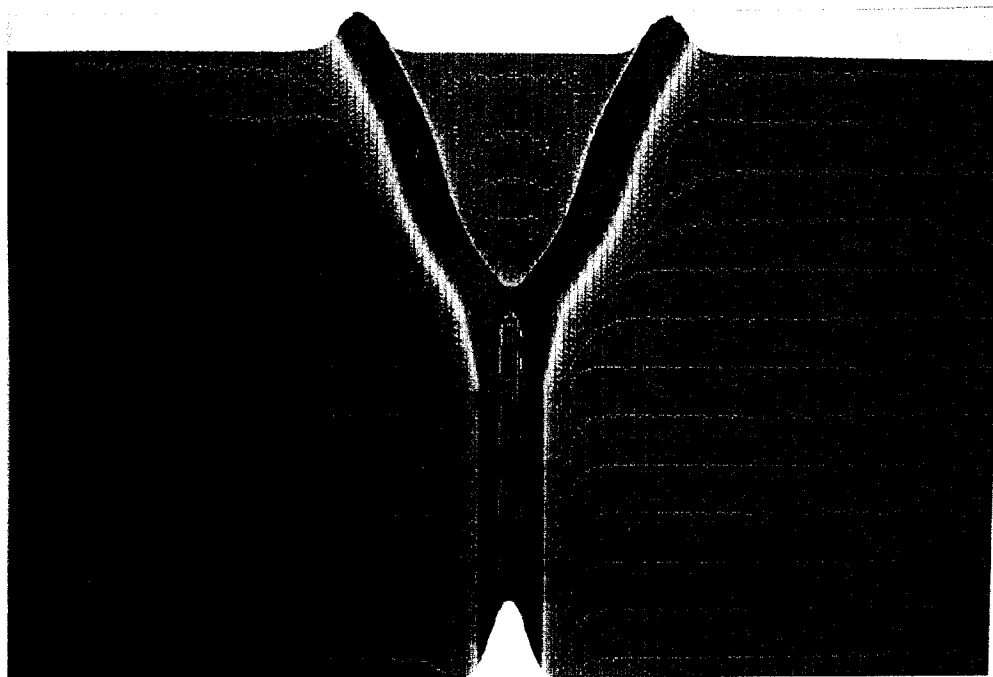
(b)

Figure 27. Input YPD analysis: (a) step index profile; (b) BPM analysis.

the asymmetric device the first null occurs at V= 1.0 volts and the first maximum occurs at V = 3.1 volts. The BPM profile of the output power combiner index profile is shown in Figure 28 while the optical field distribution in the combiner is shown in Figures 29(a) and 29(b) for V = 1.0 volts and V = 3.1 volts, respectively. An easier interpretation of the effe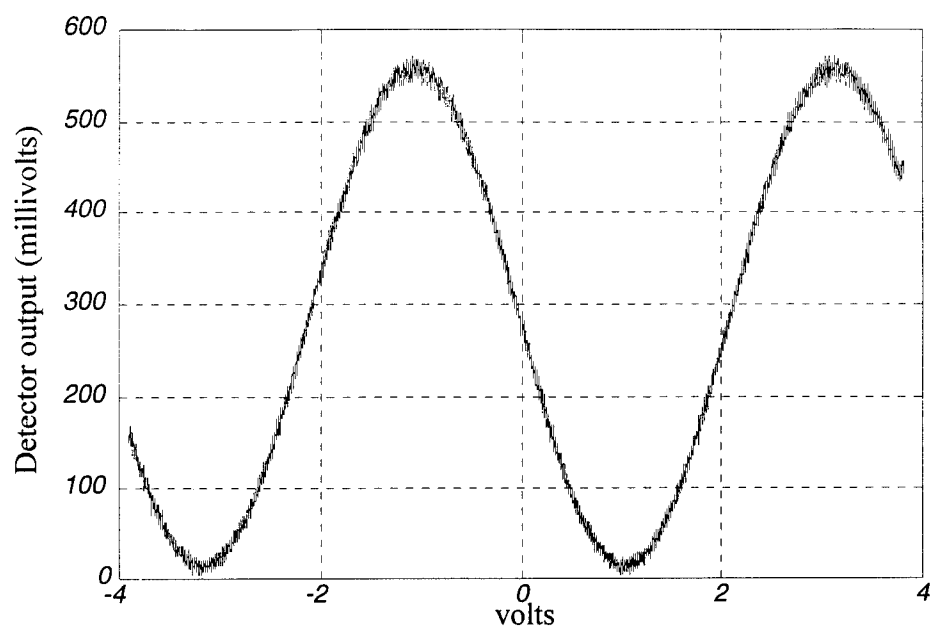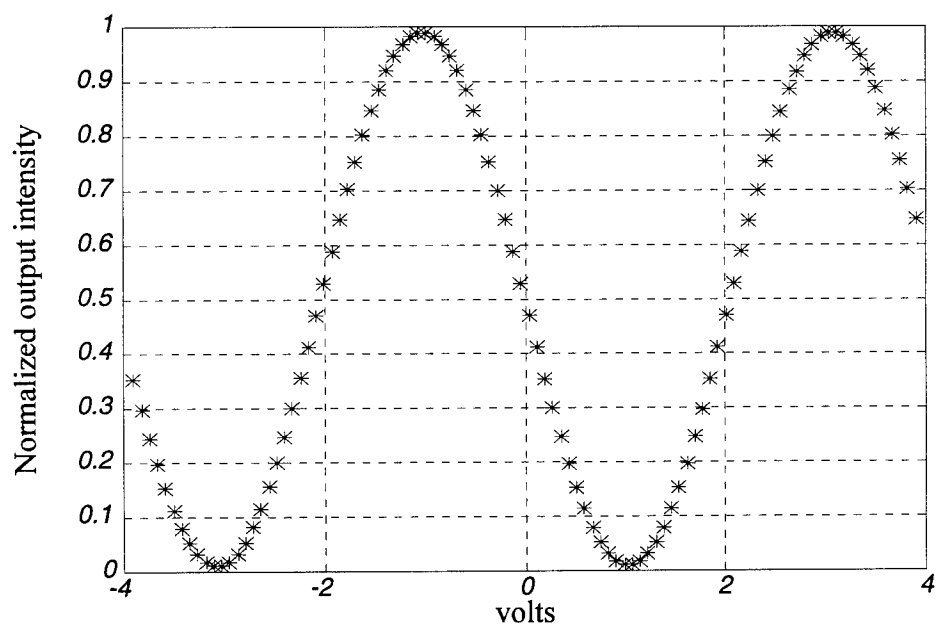cts at the output combiner is seen as a cross-section of the optical field is superimposed upon a scaled version of the index structure. The cross-section of *L7* shown in Figures 30(a) and 30(b) show the effects of an applied voltage of V = 1.0 volts and V = 3.1 volts, respectively.

D. VALIDATION

Utilizing the BPM calculations of the output power characteristics, the overall device loss can be projected using Equation (80) as Loss = 3.42 dB. The actual device loss was reported [9] as approximately 3 dB. This is a significant validation of the BPM ability to properly include radiation mode losses due to device length and branching angles. Since the arm separation distance was substantial in the asymmetric device the actual radiation coupling between branches is minimal. However, many parallel processing architectures require multiple parallel devices in which radiation coupling may be even more significant than radiation losses in the substrate.

Now that the BPM has been shown to be a valid tool for analysis of optical devices, more complex systems may be analyzed with confidence.

61

Figure 28. Output power combiner design: step index profile.
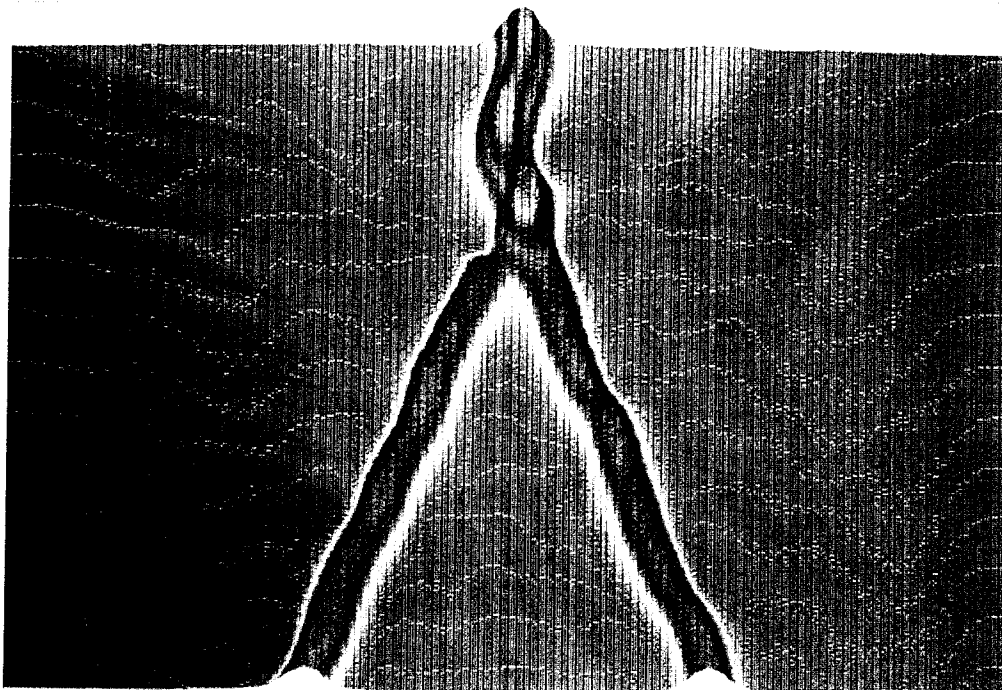
(a)
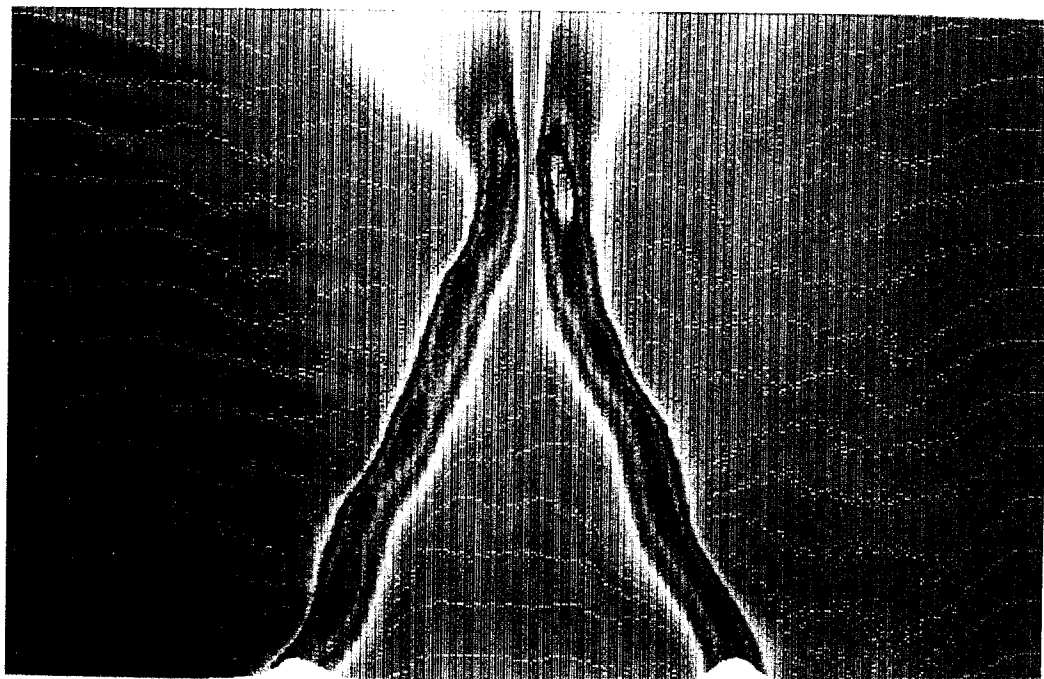
(b)

Figure 29. Output power combiner BPM analysis: (a) V = 1.0 volts; (b) V = 3.1 volts.

63
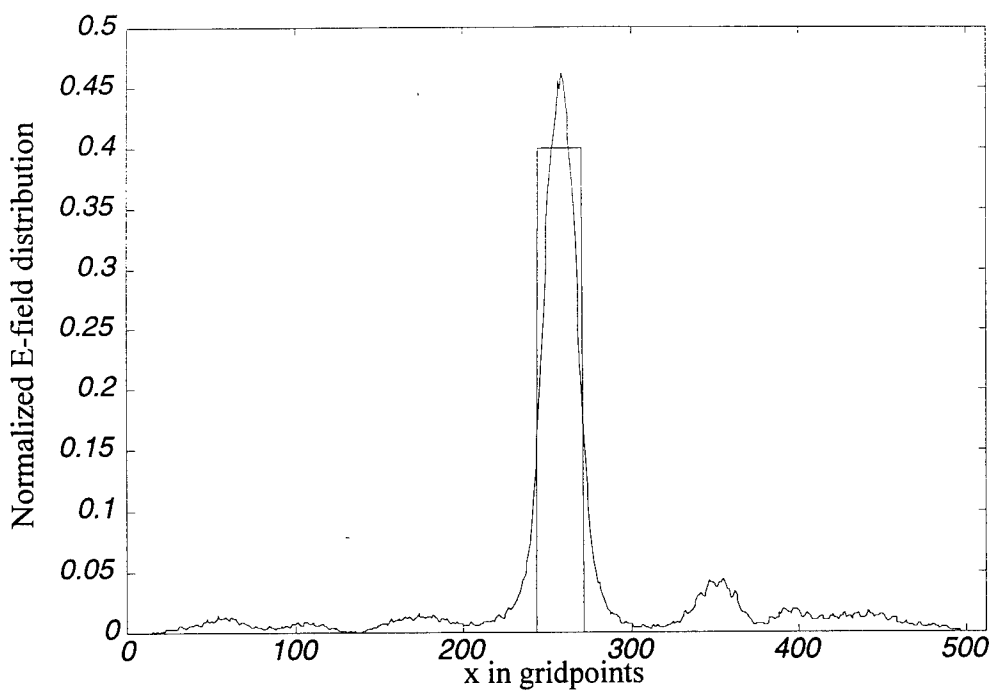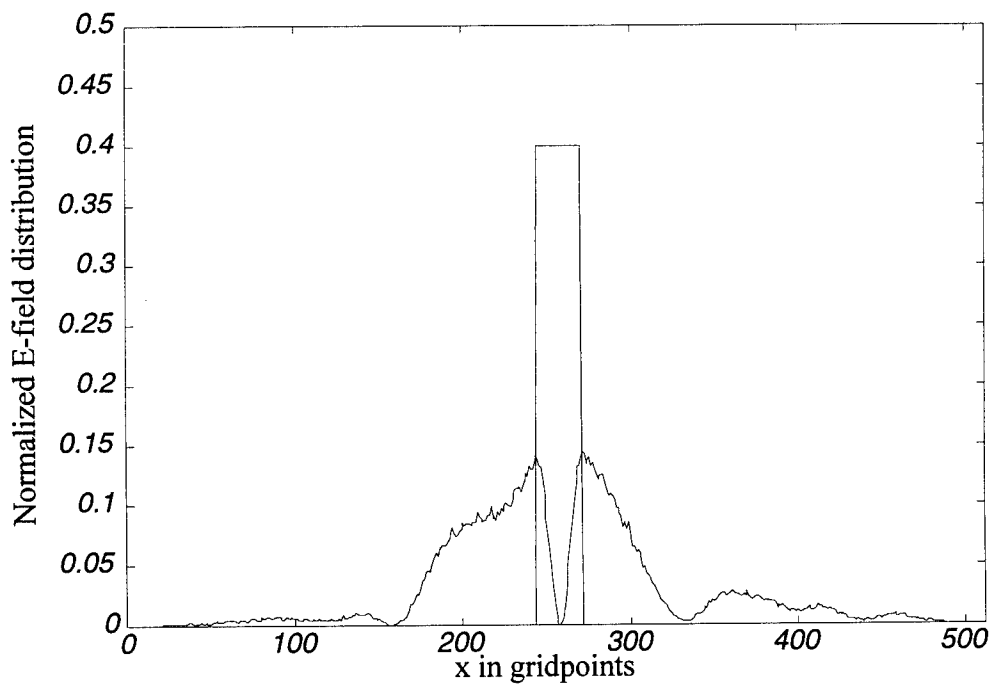
Figure 30. Cross-sectional view of L7 region: (a) V = 1.0 volts; (b) V = 3.1 volts.
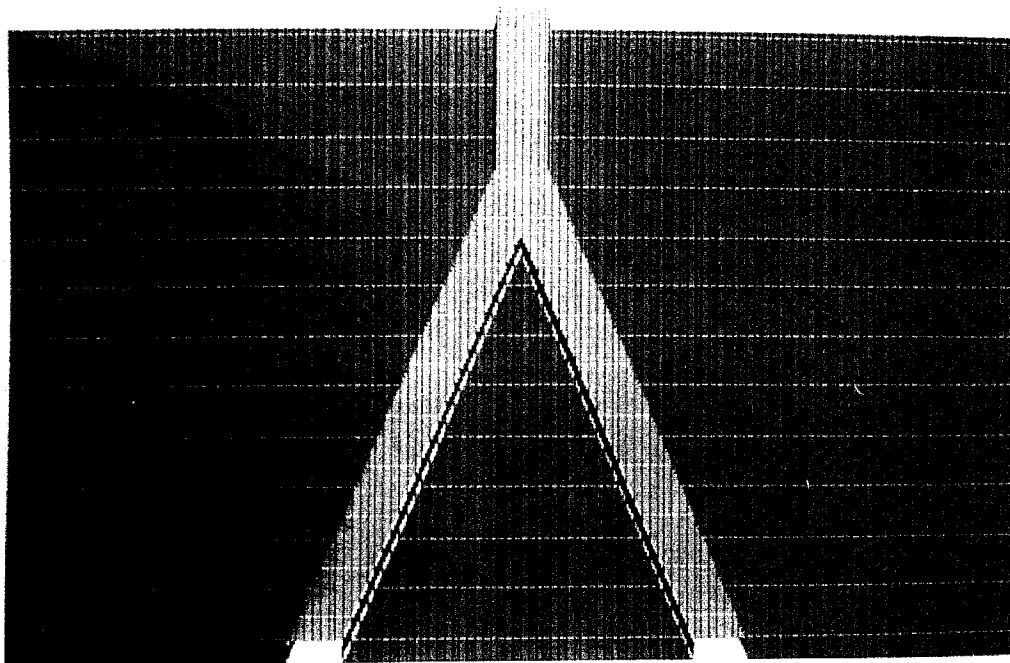
64

V. PARALLEL CONFIGURATION OF MACH-ZEHNDER INTERFEROMETERS

Parallel configurations of MZIs are important in many signal processing architectures. They can efficiently couple wideband rf signals into the optical domain making them useful for such applications as high-speed analog-to-digital converters, temperature sensing, and real time optical correlators [5]. In these types of architectures the interferometers are arranged in parallel configurations containing many successive bends and branches that distribute the optical power to the various sections of the circuit. A significant problem with the parallel integration of these devices is the limited efficiency due to radiation loss [5]. The BPM is a useful tool in designing and analyzing these types of systems.

A. DEVICE PARAMETERS

The initial architecture is shown schematically in Figure 31 and consists of two parallel interferometers that employ YPD's and combiners that have been analyzed earlier in this thesis. The corresponding parameter values are shown in Table 3. The separation distance d_i between the interferometers is varied by changing the length of $L2$ while holding the branching angle constant. The individual interferometers are configured identically to those analyzed previously. However, the overall grid width must be increased to accommodate the parallel array. The window size is again calculated using Equation (66); $W = 106$ μm would allow for the decay distances, absorption windows, separation distances $d_i = 20$ μm, and $d_a = 20$ μm. Once again, the impact of the window
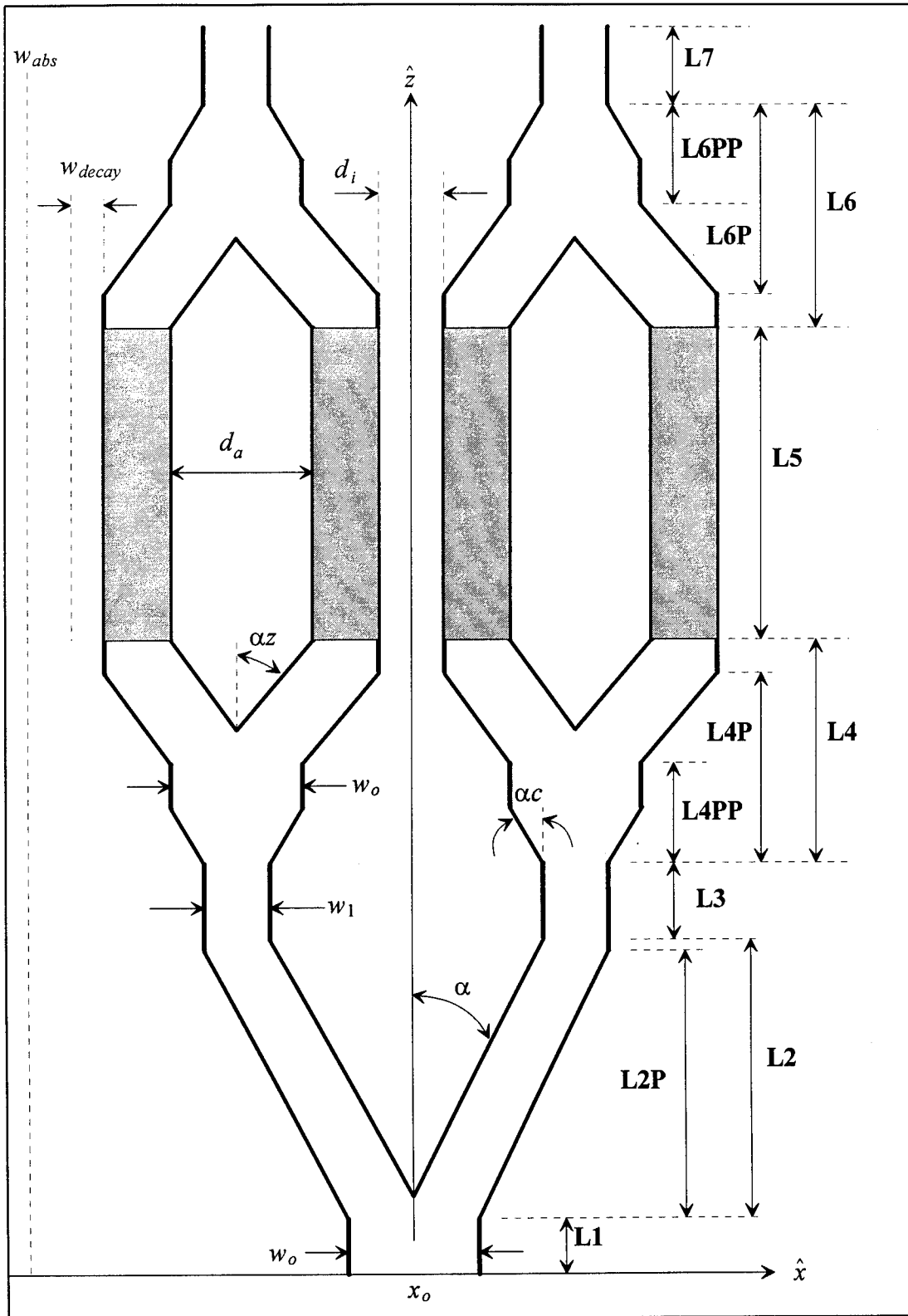
Figure 31. Schematic diagram of two parallel MZIs.

66

size must be evaluated in relation to the desired discrete guide width w_d. In this case the guide width is desired to be 3.0 μm, so the appropriate adjustment must be made to the grid size W. It is anticipated from previous evaluations that the number of grid points will be 512, due to the grid size, so $W = 102.4$ μm is chosen. Using Equation (48) we solve for N as

$$N \geq \frac{2(2.2)(102.4\mu m)}{900nm} \frac{1}{\sqrt{2}} = 354, \tag{86}$$

and as expected $N = 512$ is chosen. The next step is to determine the transverse sampling interval using Equation (49)

$$\Delta x = \left(\frac{W}{N}\right) = 0.2\,\mu m. \tag{87}$$

w_o	5.81 μm
w_1	3.0 μm
α	1.0°
α_z	1.0°
α_z	5.0°
L1	12 μm
L2	$f(d_i)$
L3	280 μm
L4	350 μm
L5	1000 μm
L6	350 μm
L7	280 μm

Table 3. Schematic parameter values.

The discrete guide width w_d can now be verified utilizing Equation (71) we have

$$w_d = \left\lfloor \frac{3.0\mu m}{0.2\mu m} \right\rfloor 0.2\mu m = 3.0\mu m. \tag{88}$$

The validation of the guide width is important in ensuring the correct mode distribution and guidance strength. The axial sampling interval is maintained at $\Delta z = 2.4$ μm for this analysis.

B. BPM IMPLEMENTATION

The BPM implementation of the parallel array index structure is shown in Figure 32(a) and the optical field distribution is shown in Figure 32(b). In the analysis shown, the spacing between the interferometers $d_i = 10$ μm and the radiation losses of the individual interferometers is the same as previously noted. However it is apparent from the optical field distribution the radiation mode coupling between the adjacent interferometers does exist. A clear view of the radiation mode coupling is given in the cross-sectional of the $L5$ region shown in Figure 33. The cross-sectional view shows the optical field distribution super-imposed upon a scaled version of the waveguide index structure and clearly demonstrates the existence of power coupling.

C. RADIATION MODE EFFECTS

The radiation modes shown in Figure 32(b) may extend to the point that interference with adjacent interferometers exists. The effects the radiation modes have on the interferometer outputs and the respective change in the mode propagation constant ($\Delta \beta$) are a function of the separation distance d_i. The radiation modes of one interferometer may also affect the radiation modes of the other interferometer. This interference effect produces a finite $\Delta \beta$ within the affected interferometer. The radiation can be eliminated by extending the separation distance d_i to infinity. However this is
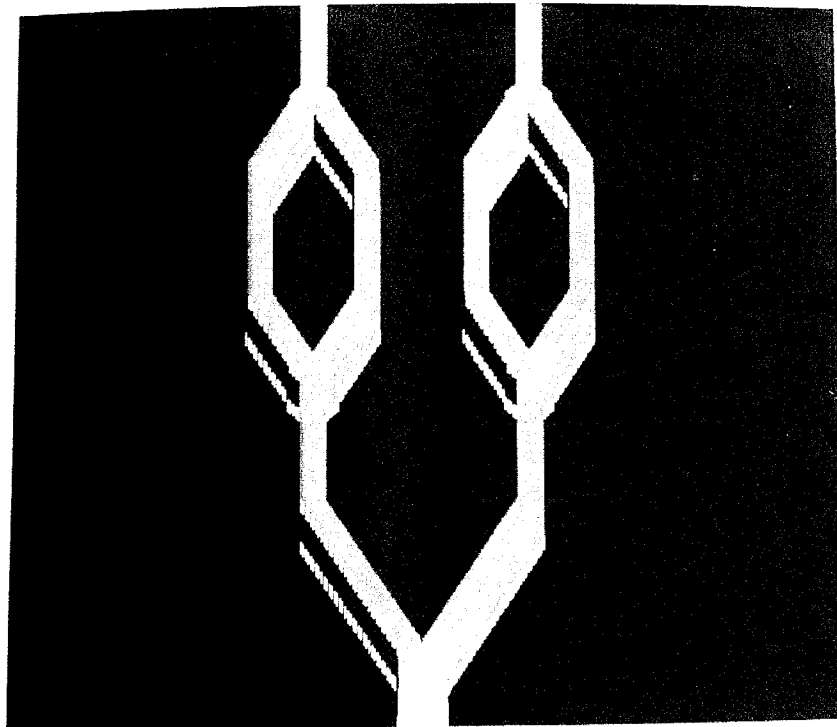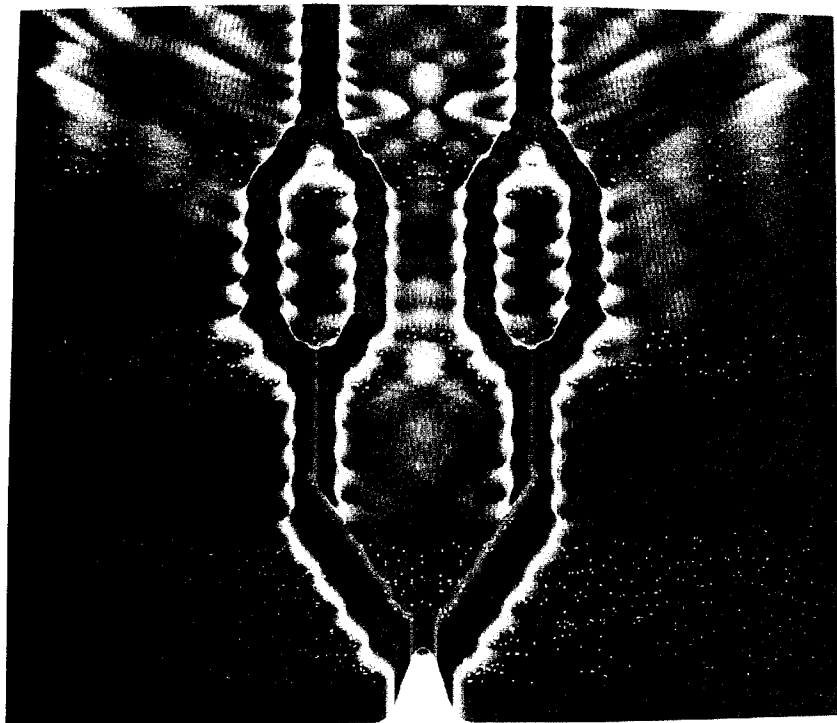
Figure 32. Radiation mode coupling between two parallel interferometers: (a) step index profile; (b) BPM analysis.
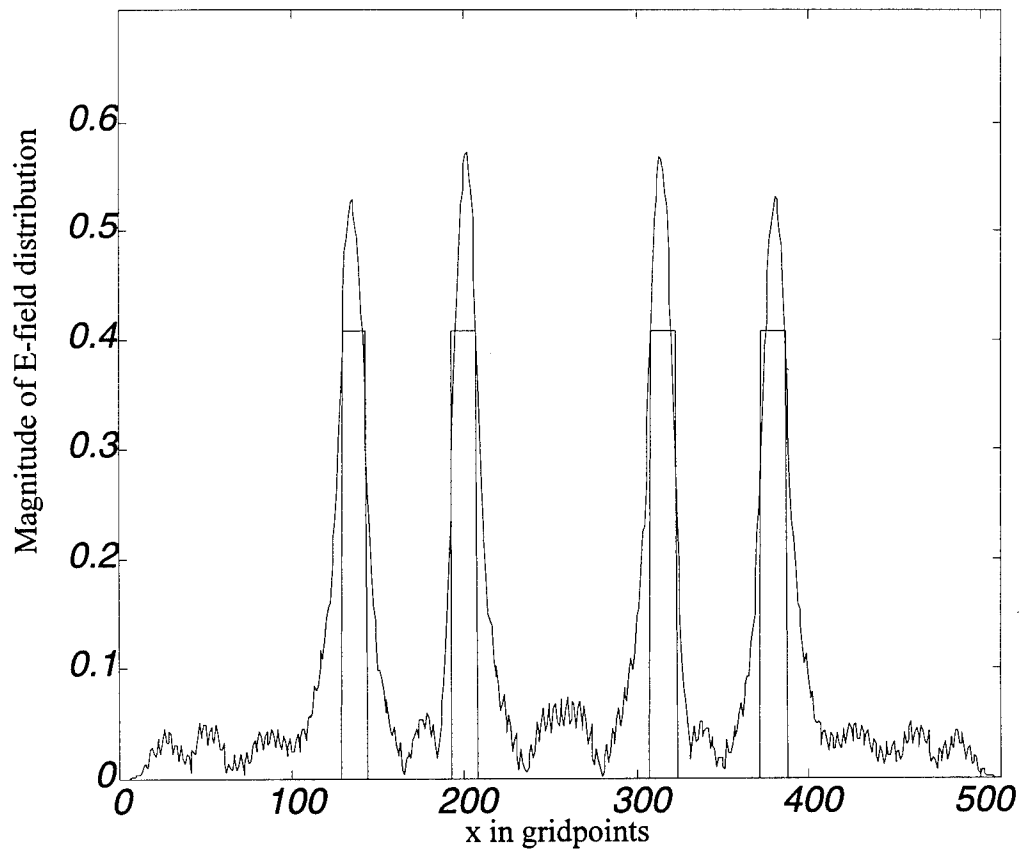
Figure 33. Cross-sectional view at the center of L5 (V = 0).

obviously impractical. The BPM provides an excellent method for analyzing the effects of the radiation mode coupling and is a useful tool for minimizing radiation mode effects while optimizing the interferometer spacing. The dependence of radiation mode coupling on interferometer spacing d_i are clearly demonstrated through Figures 34(a) and 34(b). The interferometer spacing in the index profile of Figure 34(a) is reduced to $d_i = 5$ μm and the effects are directly demonstrated in the field distribution of Figure 34(b). Although extending the interferometers to infinity is not practical, it is anticipated that radiation coupling effects will drop off rapidly as d_i is increased. The results of increasing the separation distance to $d_i = 20$ μm are clearly shown in Figures 35(a) and 35(b). It is apparent from this representation that radiation mode coupling can be minimized utilizing the BPM as a design tool.

1. Input/Output Characteristics

The effects of radiation mode coupling can be quantified using the BPM algorithm. The two interferometers are initially spaced very close together. For each separation distance d_i the input power to each interferometer and their respective output powers are recorded with V = 0. Due to the symmetry of the input power distribution equal power is delivered to the input of each interferometer. Figure 36 shows the input power and the output power for the left interferometer as a function of d_i (normalized to the input power at the smallest separation distance). At small separation distances the output power is severely degraded due to the radiation coupling between the interferometers. The effects of the radiation mode coupling go through regions of

71
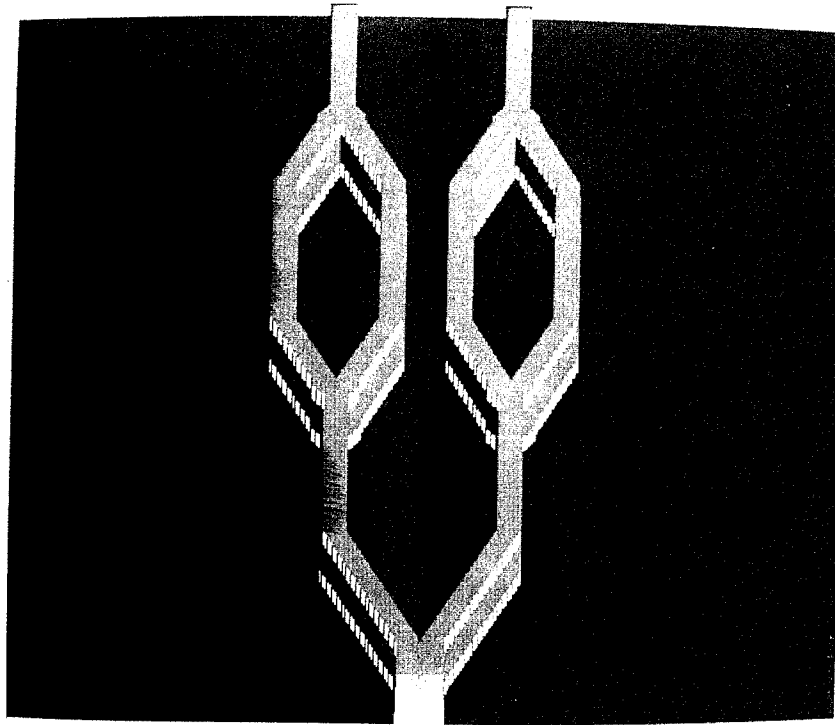
(a)
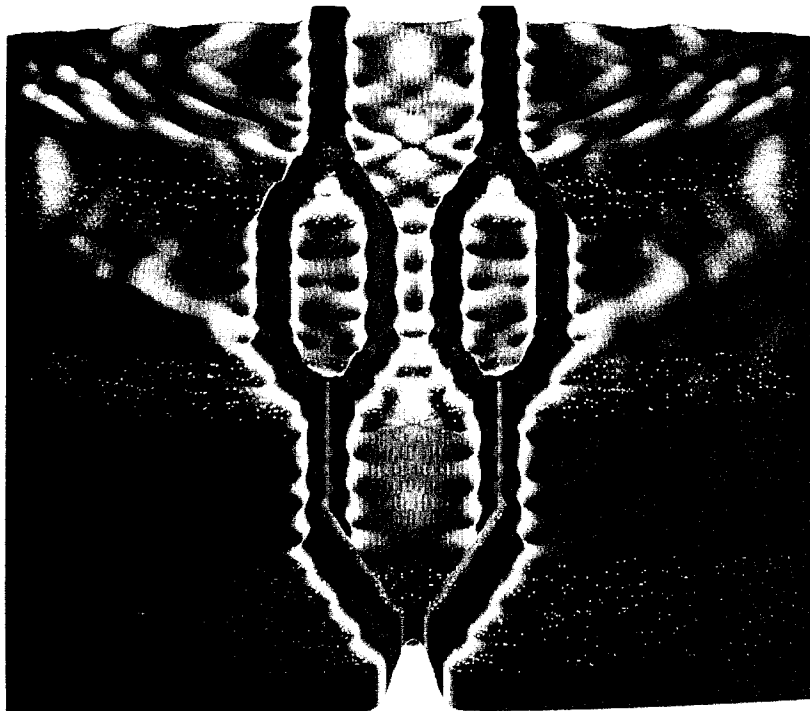
(b)

Figure 34. Parallel interferometers with spacing $d_i = 5\,\mu m$: (a) step index profile; (b) BPM analysis.
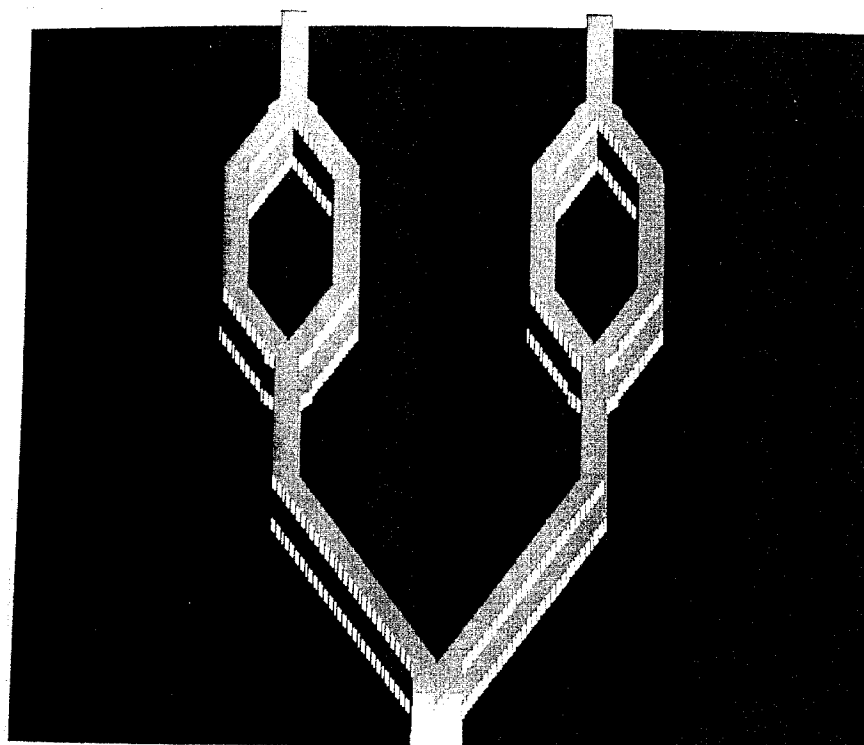
(a)
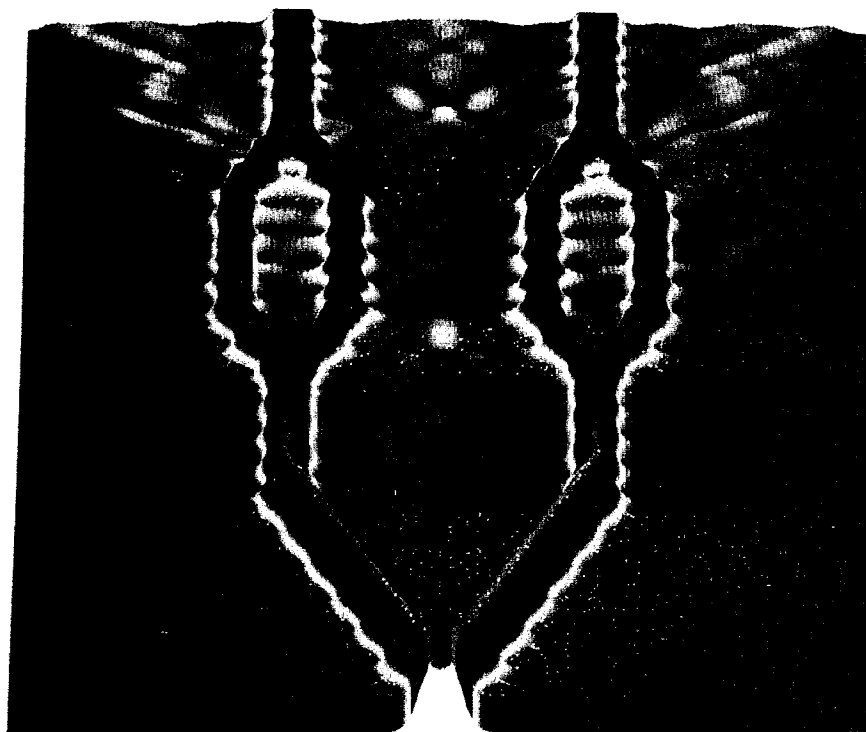
(b)

Figure 35. Parallel interferometers with spacing $d_i = 20 \mu m$: (a) step index profile; (b) BPM analysis.

73
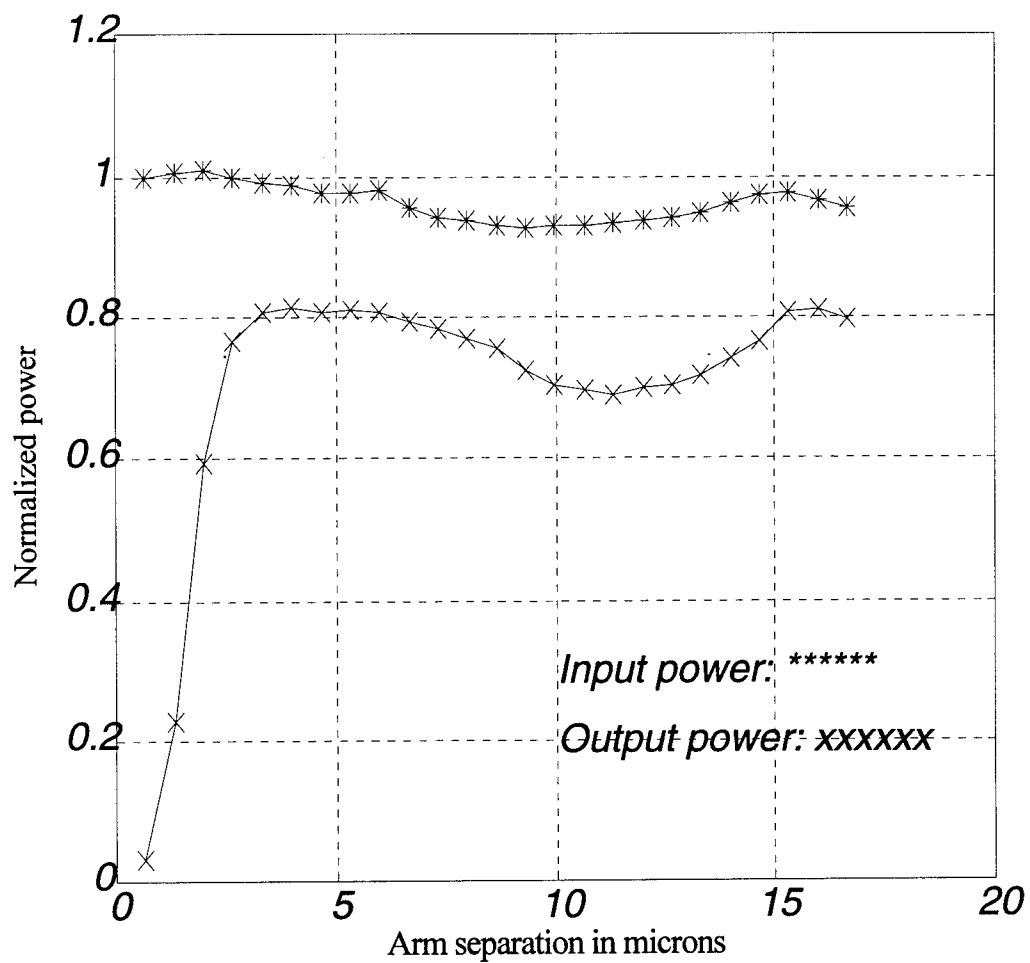
Figure 36. Input versus output power for the left interferometer.

constructive and destructive interference as d_i is increased. However, these evaluations are performed with V = 0. The arm separation must be at least large enough to minimize the interference effects.

2. Insertion Loss

Insertion loss is also an important characteristic of optical interferometers. The induced $\Delta\beta$ due to the radiation mode interference tends to decrease the power transmitted and is reflected in the insertion loss calculation [5]

$$L_{1,2}(d_i) = 10 \log\left(\frac{P_t}{P_{1,2}}\right), \tag{89}$$

where P_t is the optical power that would be transmitted by the waveguide if the modulator were absent, and $P_{1,2}$ is the intensity transmitted with the modulator in place and V = 0. To calculate the insertion loss a special index structure was constructed and is shown in Figure 37(a). The right interferometer has been replaced with a straight section of the waveguide. The magnitude of the optical field is shown in Figure 37(b). It can be noted from Figure 37(b) that even though the interferometer is replaced, the bends from the initial YPD and the branching angle cause perturbations in the optical field. The subtle insight obtained from this structure reinforces the fact that radiation losses have a direct dependence on branching angles. The insertion loss as a function of the separation distance d_i is shown in Figure 38. As the distance between the interferometers increases, the insertion loss due to the induced $\Delta\beta$ decreases. Insertion loss of less than 1/2 dB is obtained at a separation distance of 4 μm. For separation distances of greater than 4 μm the radiation modes start to interfere constructively as was noted in the analysis of the

75
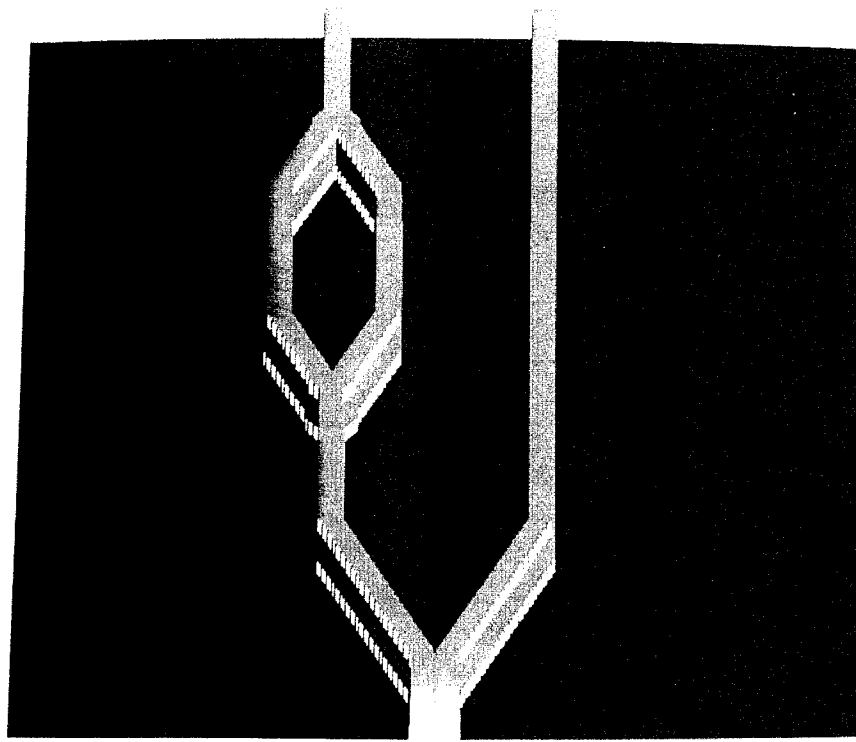
(a)
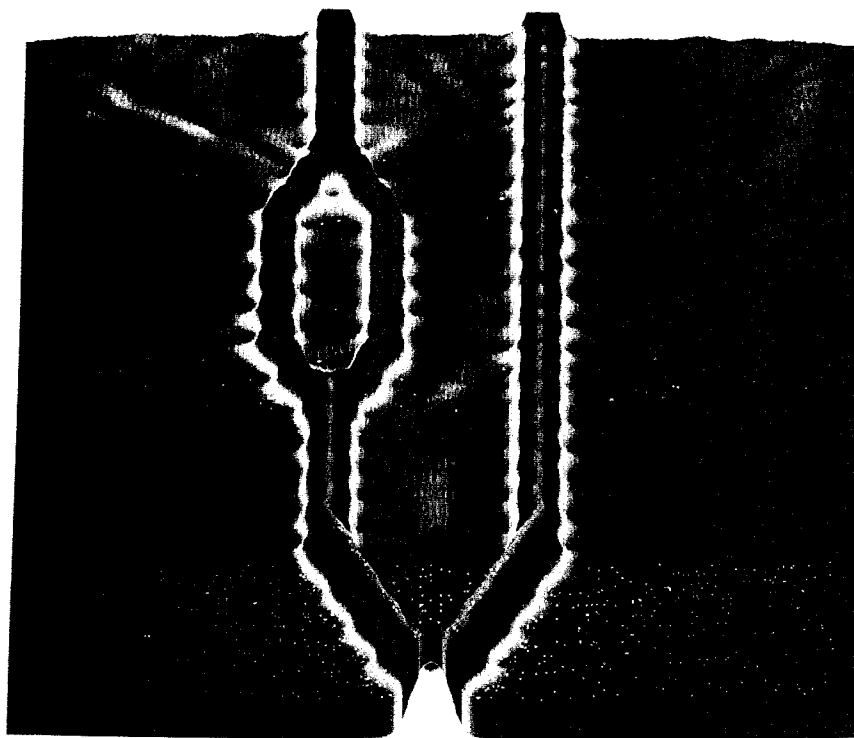
(b)

Figure 37. Modified architecture for insertion loss and mode coupling calculations: (a) step index profile; (b) BPM analysis.

76
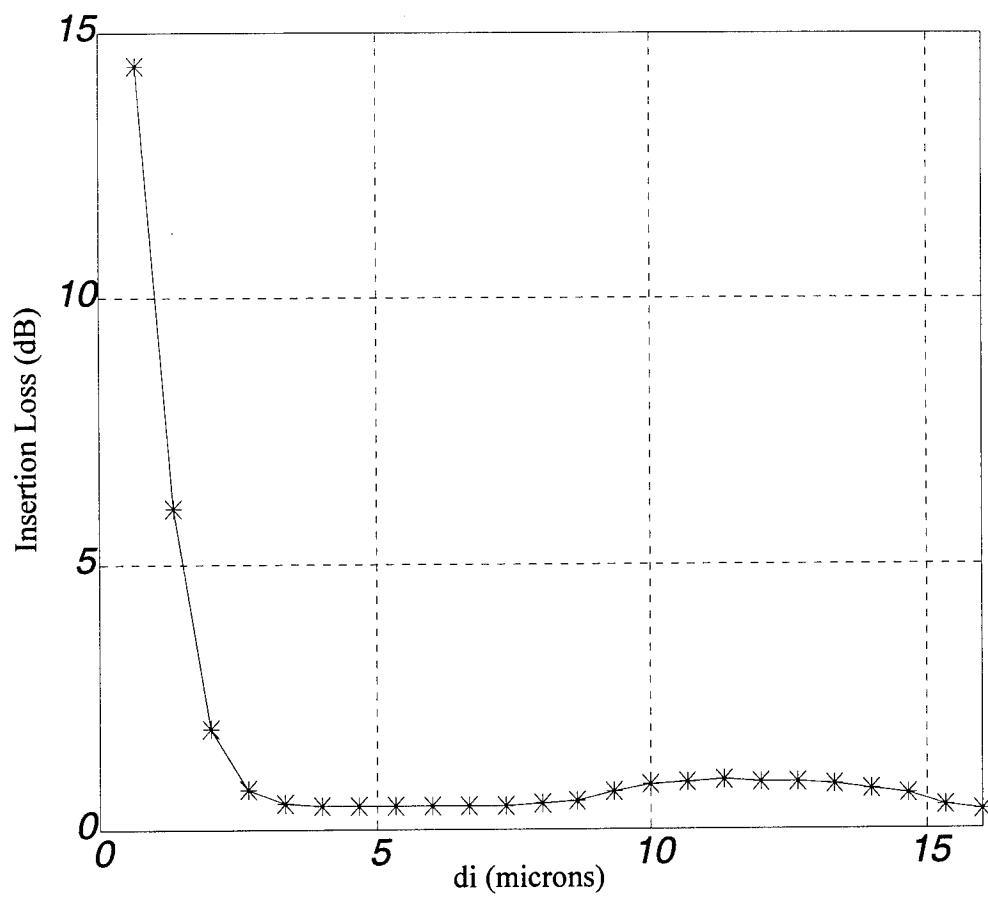
Figure 38. Insertion loss as a function of the separation distance.

output characteristics. This constructive interference increases the insertion loss somewhat and then tapers off at larger d_i [5].

3. Radiation Mode Dependent Finite $\Delta\beta$

As previously mentioned, the induced $\Delta\beta$ due to the radiation mode interference gets smaller as d_i gets larger. The expression that relates the transmission efficiency and the degradation in output intensity due to the radiation losses P_{loss} is given as [5]

$$P_{loss} = P_{in}\,\cos^2(\Delta\beta\,L/2) - P_{1,2}.$$

(90)

An approximation for $\Delta\beta$ can be found as [5]

$$\Delta\beta = \left(\frac{2}{L}\right)\cos^{-1}\left(\frac{P_{1,2} + P_{loss}}{P_{in}}\right)^{1/2}.$$

(91)

Since the input power changes for each d_i due to the increase in path length, a normalization procedure is needed so that the induced $\Delta\beta$ can be monitored. First, the power loss through a stand-alone interferometer is computed, using the architecture of Figure 3 or Figure 37. The percent power loss incurred (assumed to be all radiation mode losses) is calculated to be $p_L = 5.8\%$. The output power at the given d_i is then normalized using the respective input power and the loss value through the device p_L. To normalize P_{loss} to the input power at each separation distance we set

$$P_{loss} = p_L\,P_{in}.$$

(92)

The approximation for $\Delta\beta$ is evaluated for several separation distances with the resulting $\Delta\beta$ shown in Figure 39. The induced $\Delta\beta$ drops off exponentially as the separation distance is increased. However the effects of the periodic interference are clearly shown in the 10 μm to 14 μm separation range.

78
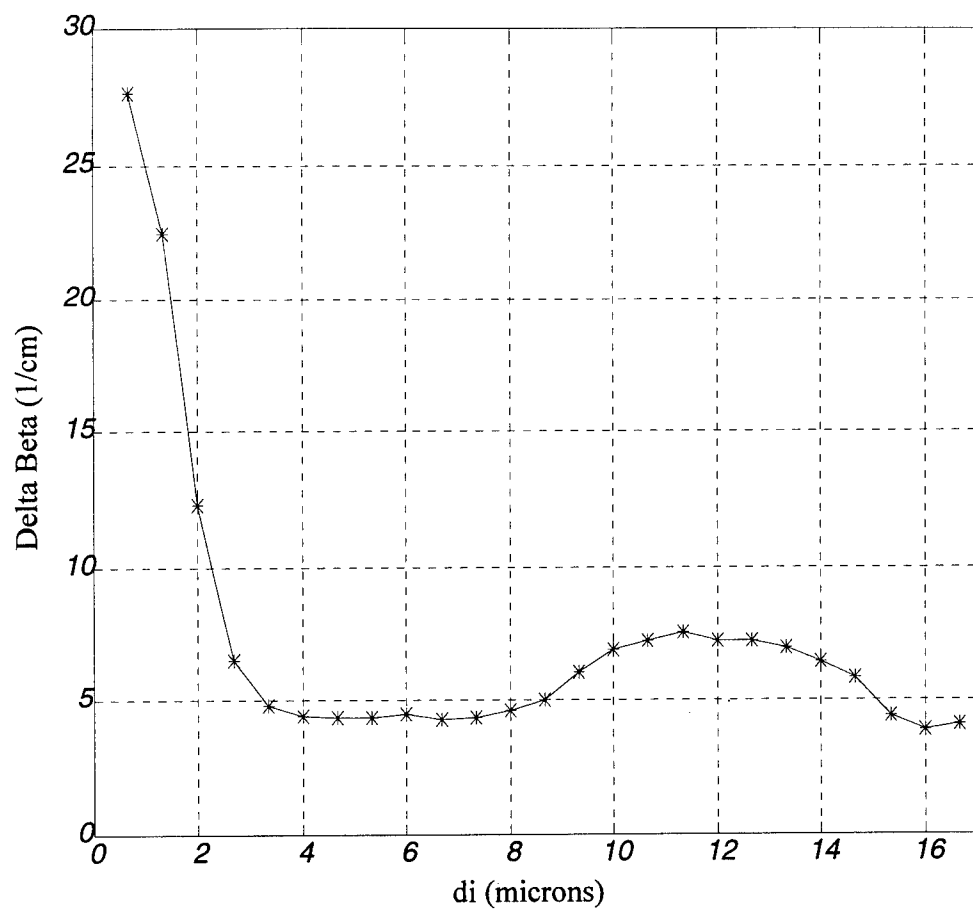
Figure 39. Delta Beta as a function of the separation distance.

4. Modulation Depth

The modulation depth of the individual interferometers and the corresponding effect that the radiation modes have on these modulation depths is also of concern. As mentioned earlier, the Input/Output analysis did not include the effects of radiation coupling with electrode voltages applied. The radiation-actuated $\Delta\beta$ reduces the modulation depth below 100%. A small amount of radiation interference can be tolerated if the performance of one interferometer does not adversely affect the other interferometer. Using the theoretical output intensity of Equation (63) for the symmetrical MZI the first electrode voltage point that produces output intensity extinction occurs at

$$V_\pi = \frac{\lambda w_1}{2 L_5 \Gamma r_{33} n^3},\tag{93}$$

where Γ, r_{33}, and n are the same parameters defined for the single symmetric interferometer analyzed previously. The theoretical V_π is calculated to be 8.17 V for the structural parameters given in Table 3. The BPM is used to examine the modulation depth of the left interferometer and the effect that the electrode voltage has on the adjacent interferometer as well. Figures 40, 41, 42, 43, and 44 show both the theoretical modulation characteristics and the BPM calculated outputs for the left and right interferometers for d_i = 0.66 μm, 1.33 μm, 2.0 μm, 4 μm, and 10.66 μm, respectively. Figures 40, 41, and 42 demonstrate the adverse effects of the radiation mode coupling from the left interferometer into the right interferometer. At greater separation distance the behavior closely follows the theoretically expected performance. However, the
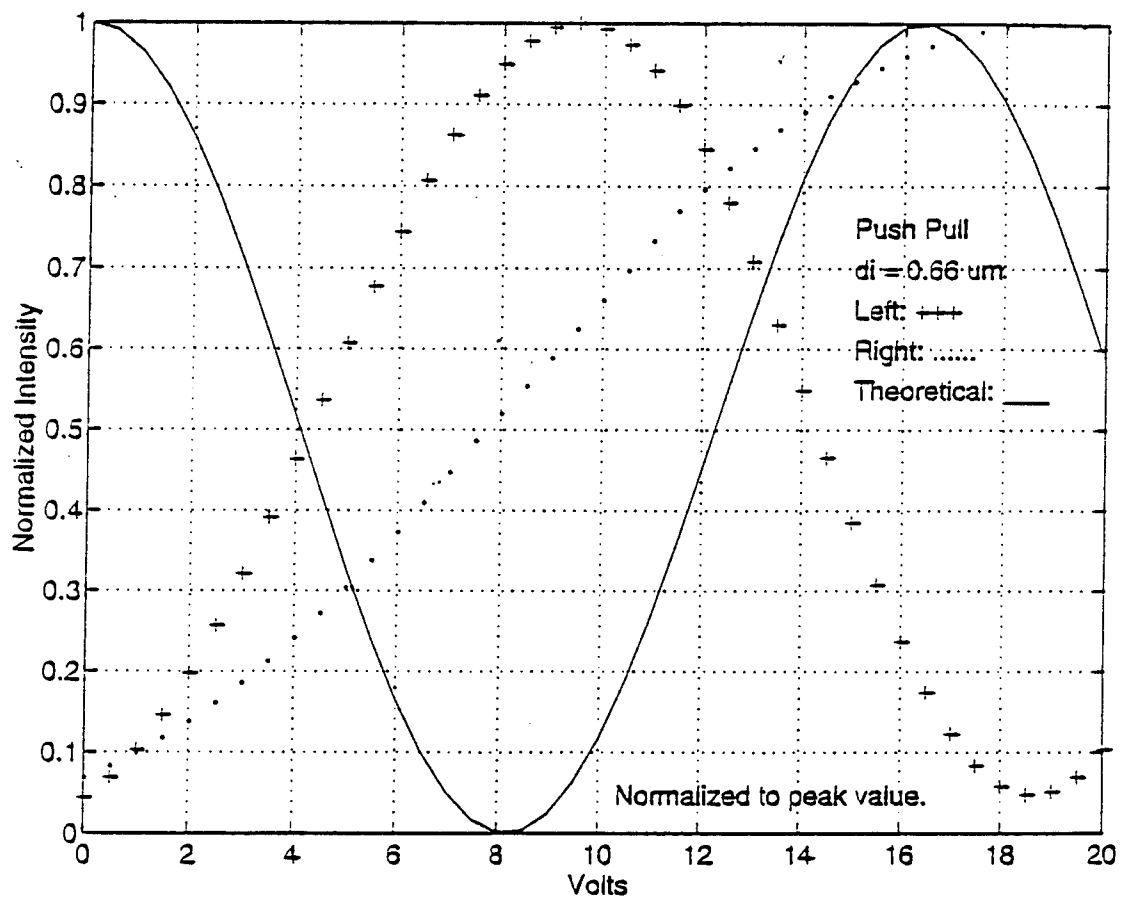
Figure 40. Modulation characteristics (di = 0.66 μm).
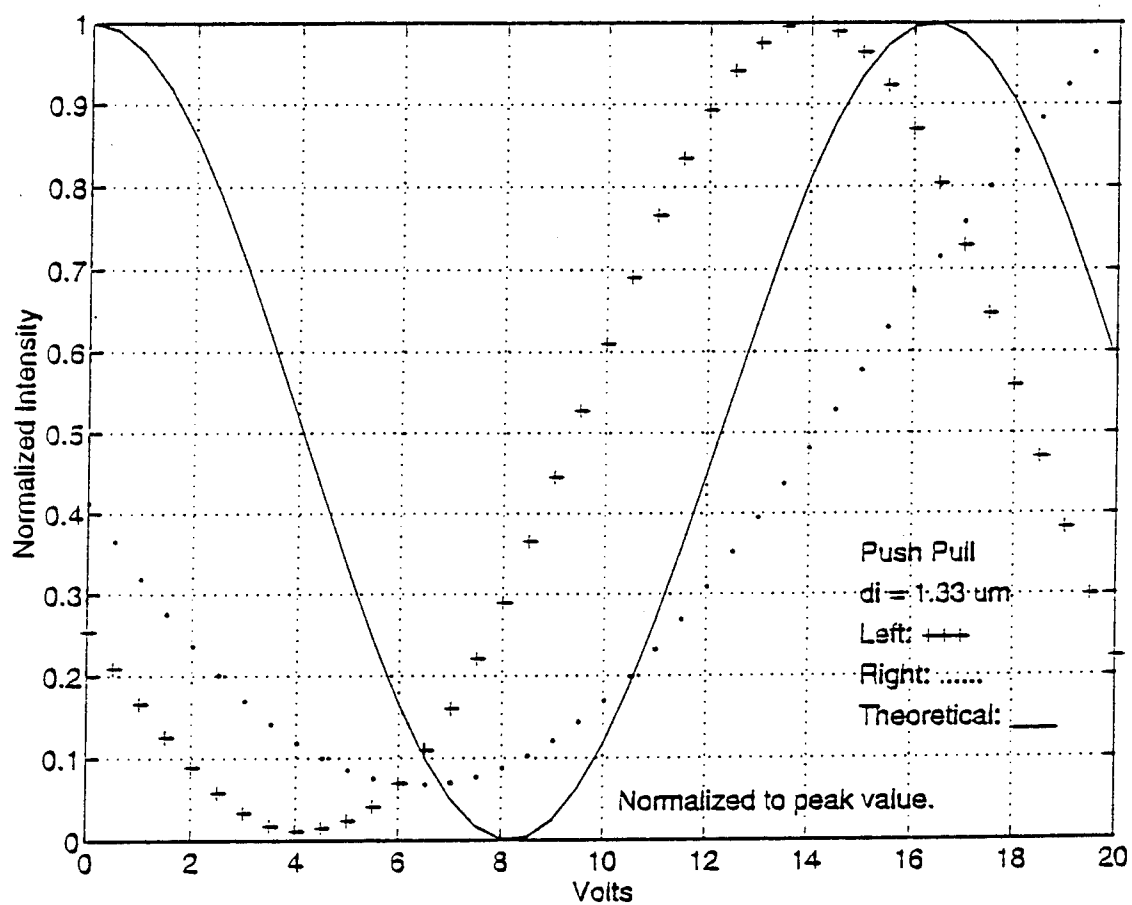
Figure 41. Modulation characteristics (di = 1.33 μm).

82
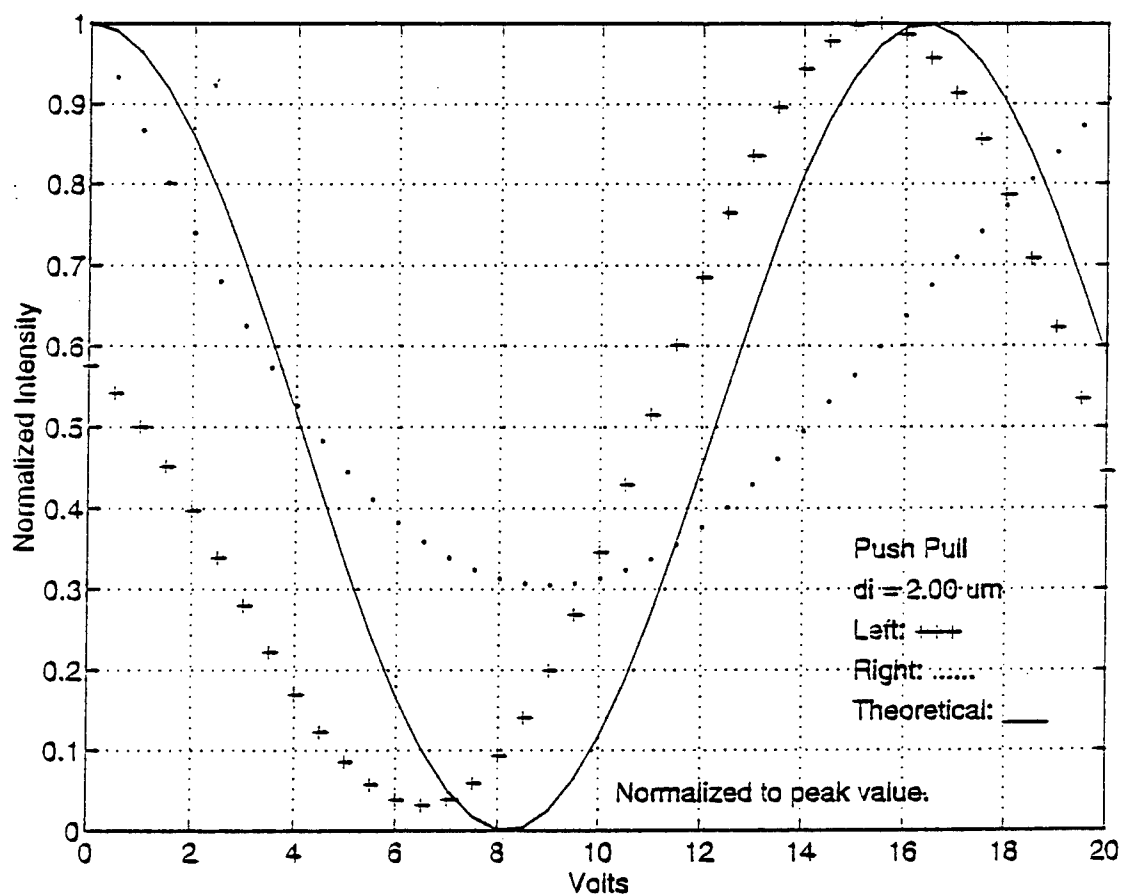
Figure 42. Modulation characteristics (di = 2.0μm).
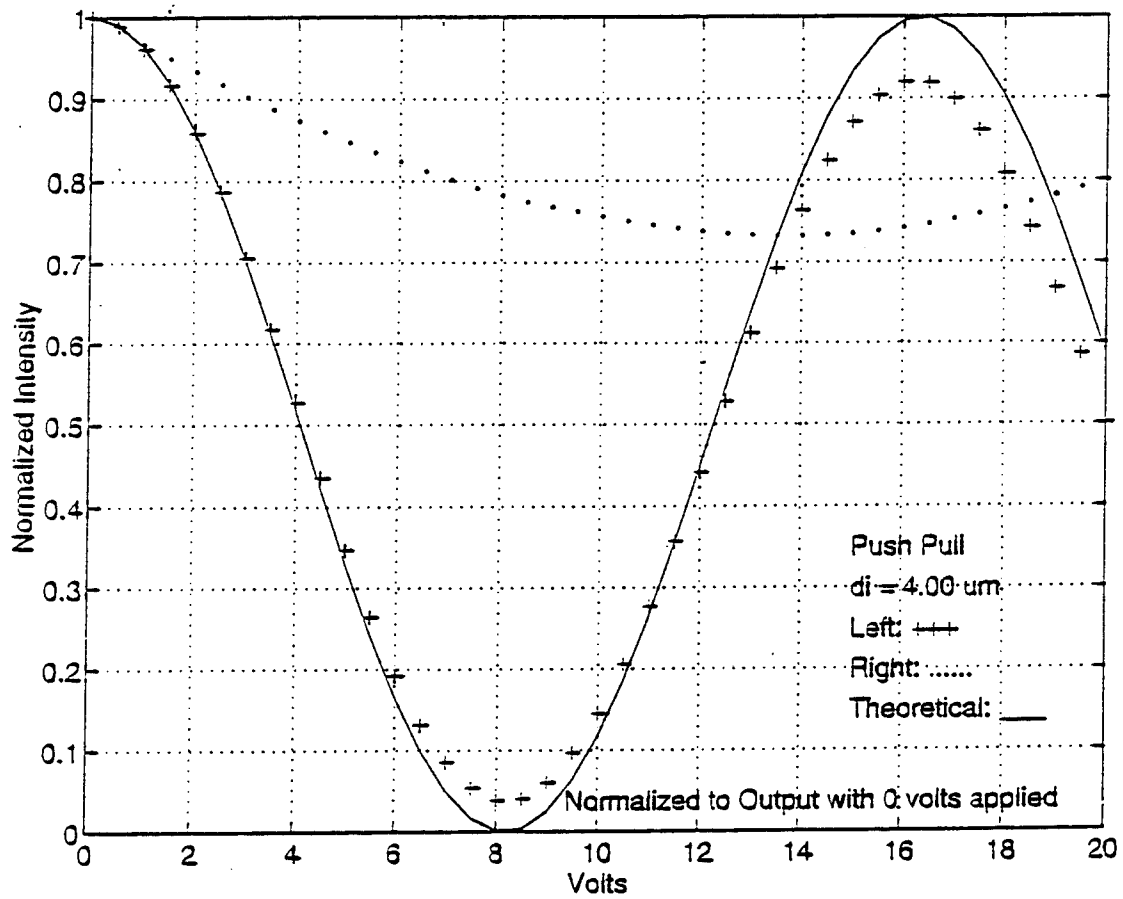
Figure 43. Modulation characteristics (di = 4.0 μm).

84
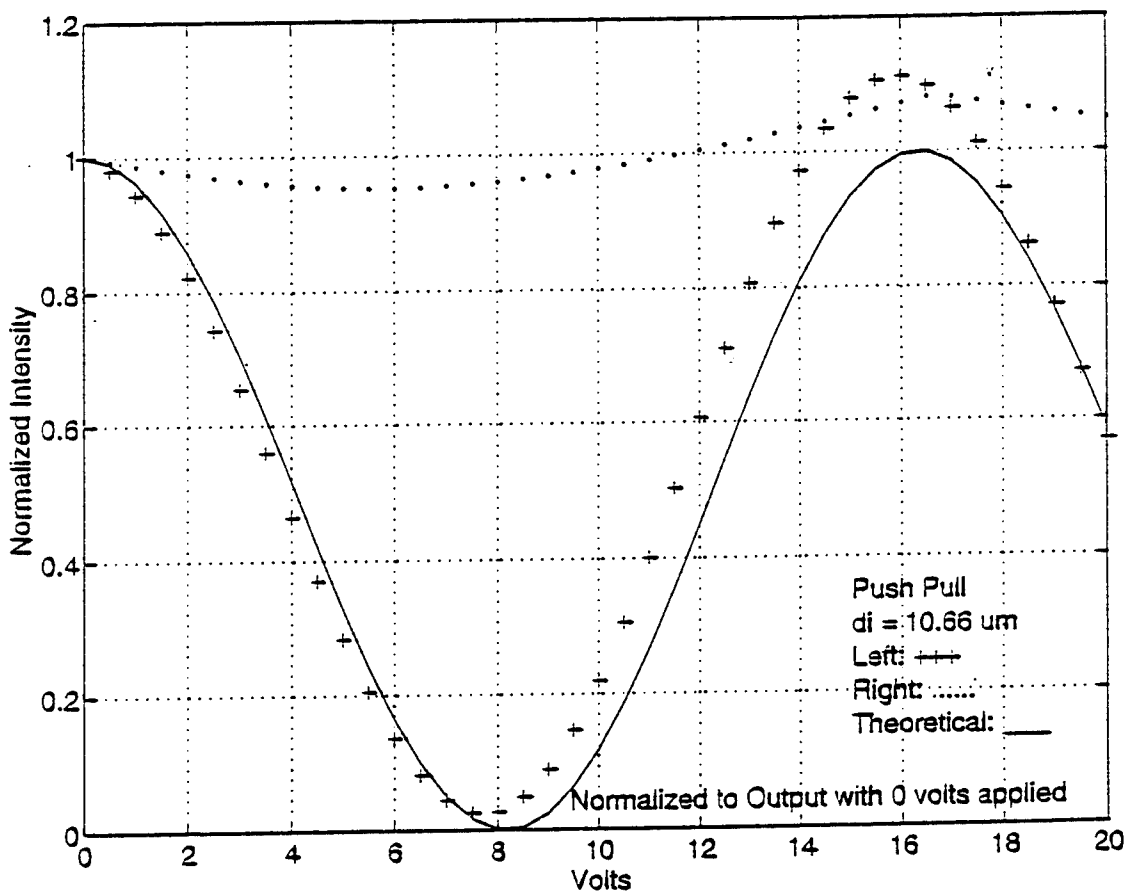
Figure 44. Modulation characteristics (di = 10.66μm).

modulation depth does not quite reach the zero limit predicted by theory. The output intensity of the right interferometer is also affected severely at small separation distance, even though no electrode voltage is applied to the right interferometer. At larger distance the radiation mode coupling causes only a slight rise in the output intensity.

The effects of the radiation mode coupling with applied electrode voltages are readily apparent when a cross section of the output optical field distribution is viewed. Figure 45 shows a cross-sectional view at the output, $L7$ section, of the parallel array with V_π applied to the left interferometer and $V = 0$ applied to the right interferometer. The mode power in the left interferometer has been coupled into the radiation modes as shown by the increased radiation modes adjacent to the left interferometer vice the radiation modes that exist due to the right interferometer. The effect of the absorption window is also readily apparent in Figure 45 as the radiation at the boundary is absorbed continuously. The total impact of the increased radiation modes due to applied electrode voltages is seen by comparing the view of Figure 45 to Figure 46, which is the same cross-sectional area with $V = 0$ on both interferometers.
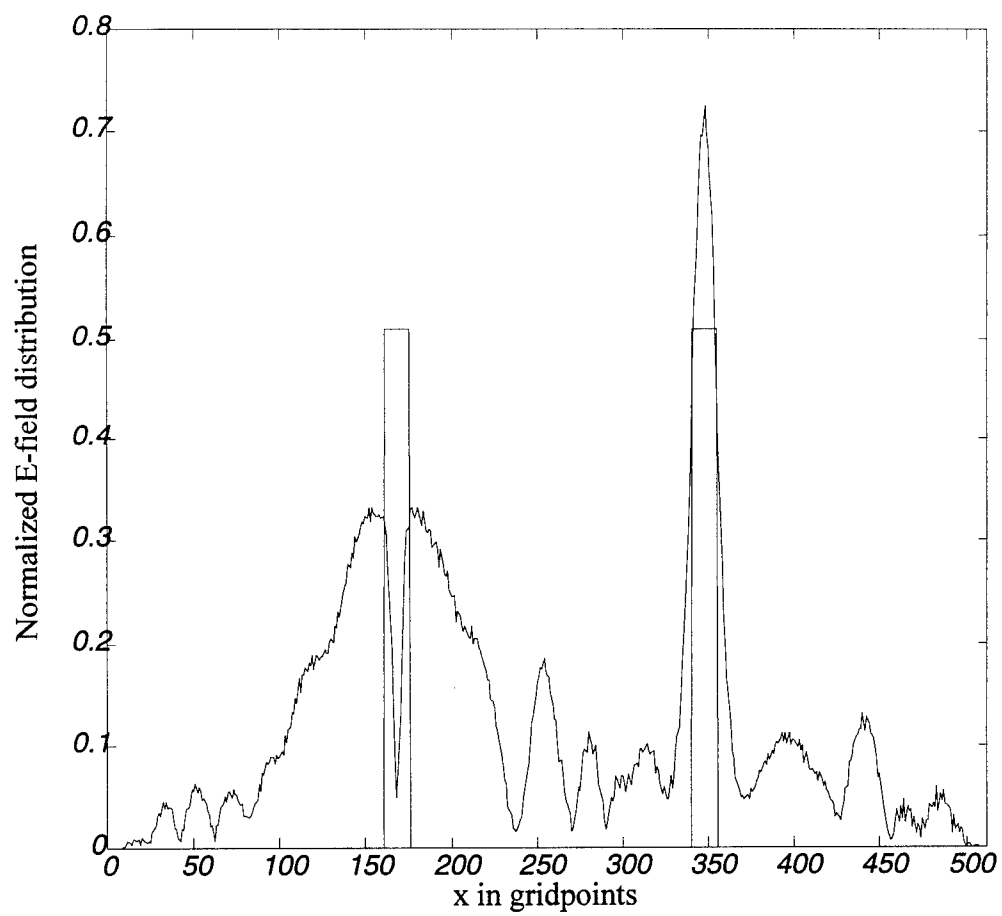
Figure 45. Cross-sectional view at the output of the array (V = 8.17 volts).
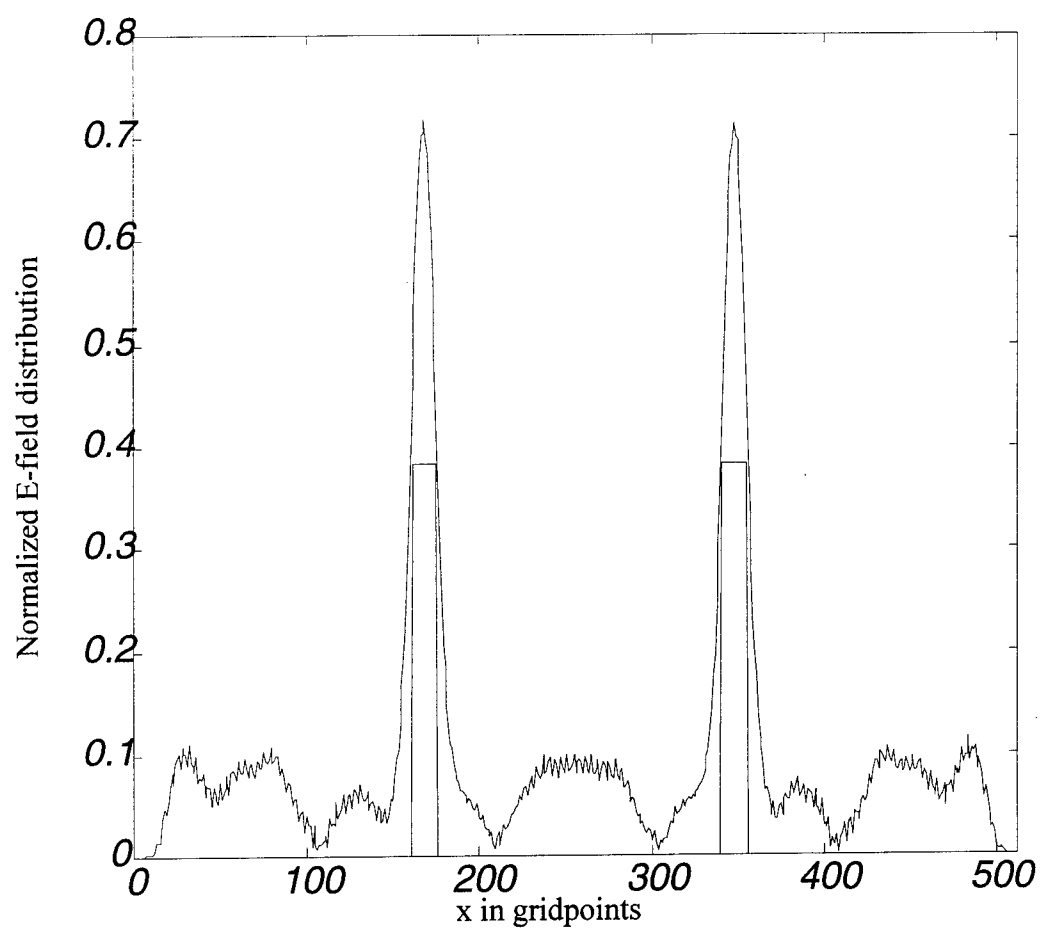
Figure 46. Cross-sectional view at the output of the array (V = 0).

VI. CONCLUSIONS AND RECOMMENDATIONS

A. CONCLUSIONS

The BPM has been previously utilized for integrated optical device analysis [4], however, the applicability of the 2-dimensional effective index method to these structures had not been shown empirically. The validation of the effective index approximation using the BPM through comparison to lab recorded data of a physical device was a major validation of this method. The BPM has been demonstrated as not only an effective analysis tool, but a potentially useful design tool as well.

The development of the prefolded global propagator has made the BPM not only applicable, but computationally efficient. The BPM algorithm is written in a C^{++} code that can be ported to personal computer platforms. The memory and computational time requirements have been reduced sufficiently to make this analysis an attractive method of optical circuit analysis.

B. RECOMMENDATIONS FOR FUTURE RESEARCH

Although the BPM has been developed into a very effective simulation tool, the effective index method does not take into account variations in the vertical transverse plane that may have significant effects. New technologies in integrated optics are now taking advantage of laser trimming technology to modify slightly the physical structures of optical devices in order to make fine adjustments to inherent phase bias during the post-fabrication phase [10]. The asymmetric device modeled in this thesis was phase tuned by laser ablation as shown in Figure 47. The laser trimming is performed after

Ablation area
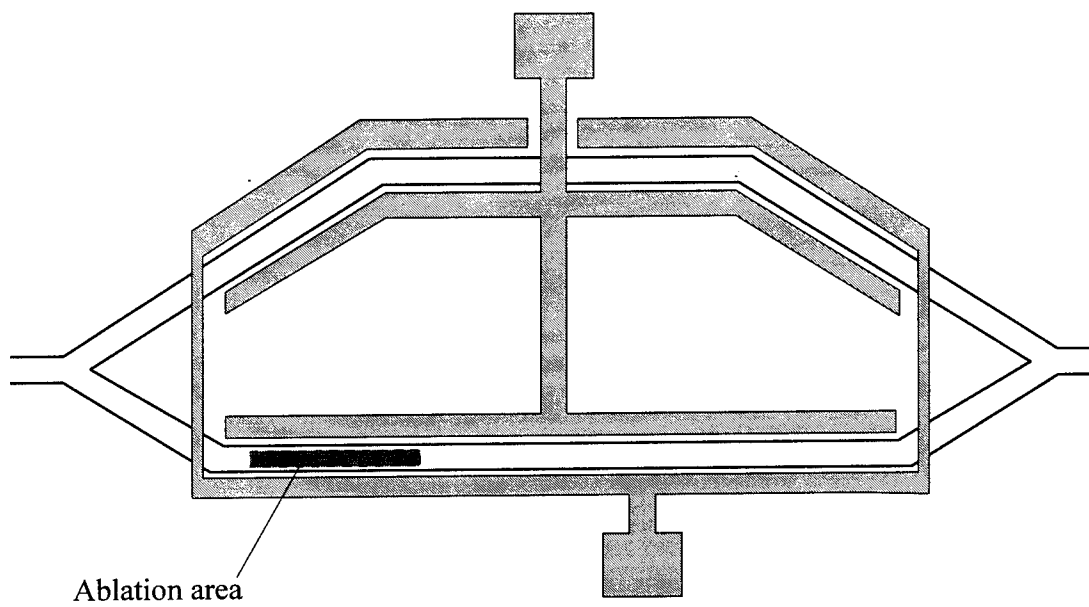
Figure 47. Asymmetric interferometer showing laser ablation region.

90

manufacture in order to optimize linearity [10]. Due to variations in temperature or other imprecise fabrication results the inherent phase bias desired in such a device may not be exact, therefore some method of post manufacture processing is highly beneficial. The BPM could easily be extended to a 3-dimensional structure in order to model these types of devices. The global propagator scheme would still be applicable to the 3-dimensional scheme so that computational requirements would only increase by the number of cross sections in the vertical grid. The power distribution through 3-dimensional devices would be viewed through cross-sections or the vertical dependence could be integrated out after the analysis so that total optical distributions could be viewed, such as the views generated in this thesis.

The BPM could also be utilized to determine the feasibility of electrooptic switches that take advantage of the linear Pockels effect. A proposed design of a digital electrooptic switch is shown in Figure 48. A switching device such as Figure 48 could easily be simulated using the BPM method, and may have potential uses in future integrated optical components. Many potential applications of optical devices are constantly emerging and the BPM may have many uses in design and analysis of these devices. The key to the success of the BPM analysis on these new technologies are validity, speed of computation, and flexibility.

Output waveguides

Digitally controlled electrodes

Input waveguide
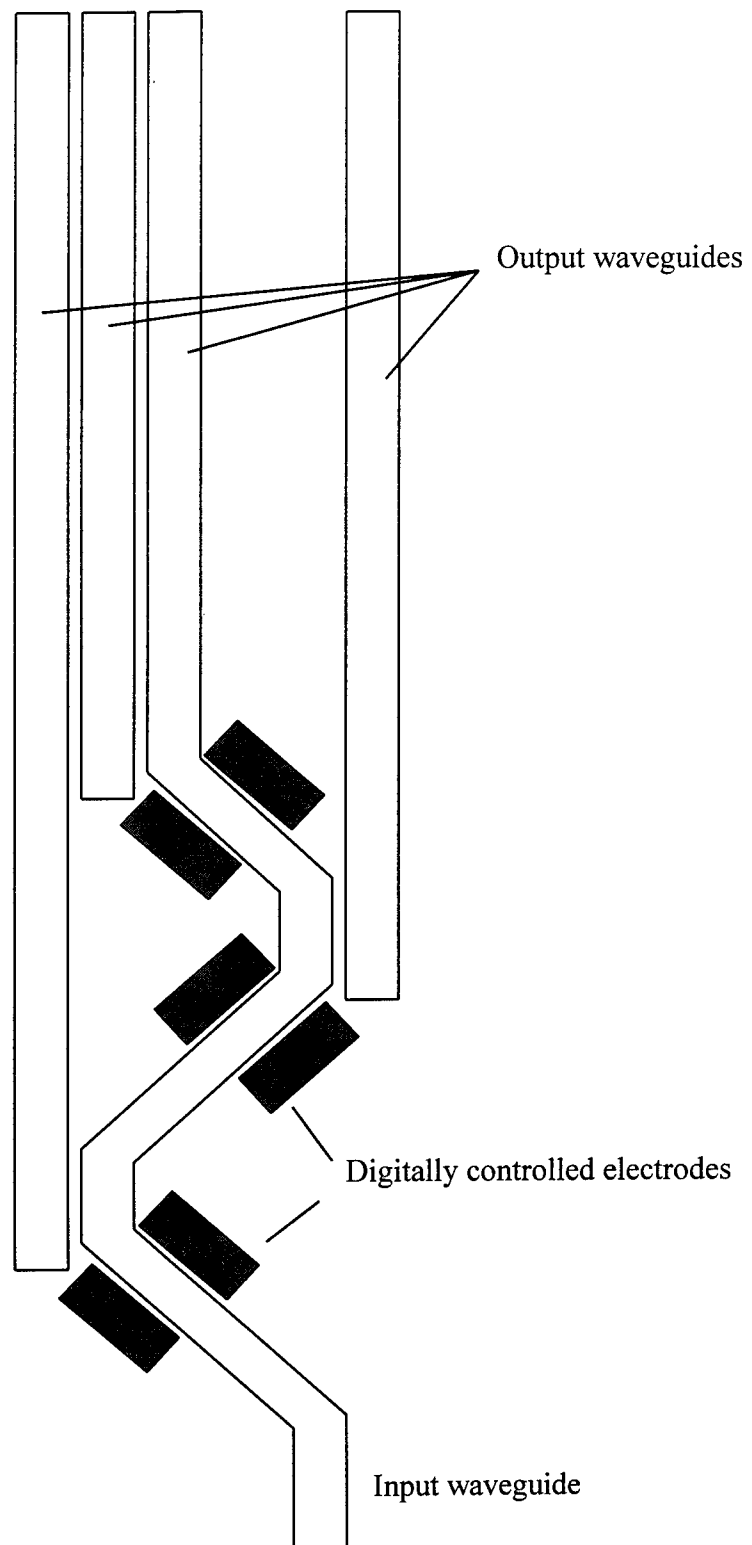
Figure 48. Proposed digital electrooptic switch.

APPENDIX. COMMAND LINE SCRIPT FILES

This appendix contains some examples of typical command line script files that were used to run extended iterations of BPM analysis on the Sun workstations.

1. EXAMPLE FOR SINGLE SYMMETRIC CODE

This file passes lengths for $L2$ and $L3$ which are in microns. The 410 is for section $L4$, the 120 is for $L4P$ coupler length, the 1000 is the electrode or $L5$ length, the 0 0 are the left and right voltages, and the last digit tells the code that the entire index and optical field data sets should be saved to disk. However, note that in this case although the right voltage is passed, it is not used, it was left in for ease of use when changing from single to parallel systems.

```
Zsing.h
#! /bin/csh -f
bpmP 12 12 410 120 1000 0  0  1
```

Table 4 below gives a breakdown of the input line items.

	L2	L3	L4	L4P	L5	VoltsL	VoltsR	Save
bpmP	12	12	410	120	1,000	0	0	1

Table 4. Input items.

2. EXAMPLE FOR ASYMMETRIC CODE

This is a much simpler case. Although Dr. Bulmer of the Naval Reasearch Laboratory gave me the arm separation of 80 microns [10], I built the code to take any arm separation distance and calculate what the $L2$ and $L3$ lengths would be to support that structure. So the parameters passed in for the example are: arm separation is 80 μm, V =

4.00 volts, and the data is to be kept. Caution should be exercised in this case. These data sets can run over 20 MB per run. It can shut the whole network down if caution is not exercised.

Zasymmetric.h
#! /bin/csh -f
 bpmP 80 400 1

3. EXAMPLE FOR PARALLEL CODE

This set up is in the exact same format as for the single symmetric case. The one item that should be observed in particular is the voltage input. The voltage is multiplied times 10^{-2}, so that $400 = 4.00$ volts.

Zparallel.h
#! /bin/csh -f
bpmP 1630 1000 1595 440 1000   0 0 1

4. EXAMPLE FOR MULTIPLE RUNS

The file name is left off the following example. The only real constraint in file names on the Unix system is that the file must have the executable flag enable in the file properties section. Typically "Z.h", "Z1.h" or some short variation was used. The following example makes 6 runs of the code and varies the left interferometer voltage from 0:0.1:0.5 volt.

```
#! /bin/csh -f
bpmP 1630 1000 1595 440  1000   0    0 0
bpmP 1630 1000 1595 440  1000   10   0 0
bpmP 1630 1000 1595 440  1000   20   0 0
bpmP 1630 1000 1595 440  1000   30   0 0
bpmP 1630 1000 1595 440  1000   40   0 0
bpmP 1630 1000 1595 440  1000   50   0 0
```

94

LIST OF REFERENCES

1. C. LeForestier, R. Bisseling, C. Cerjan, M. D. Feit, R. Friesner, A. Guldberg, A. Hammerich, G. Jolicard, W. Karrlein, H. D. Myer, N Lipkin, and O. Roncero, "A comparison of different propagation schemes for the time dependent Schrödinger equation," *J. Comput. Phys.*, Vol. 94, pp. 59-80, (May 1991).

2. M. D. Feit and J. A. Fleck, Jr., "Light propagation in graded-index optical fibers," *Applied Optics*, Vol. 17, pp. 3990-3999 (Dec. 1978).

3. Z. Weissman, A. Hardy, and E. Marom, "Mode-dependent radiation loss in Y junctions and directional couplers," *IEEE J. of Quantum Electronics*, Vol. 25, pp. 1200-2246 (July 1989).

4. M. D. Feit and J. A. Fleck, Jr., "Mode properties and dispersion for two optical fiber-index profiles by the propagating beam method," *Applied Optics*, Vol. 19, pp. 3140-3150 (Sept. 1980).

5. P. E. Pace and C. C. Foster, "Beam propagation analysis of a parallel configuration of Mach-Zehnder interferometers," *Optical Engineering*, Vol. 33, pp. 2911-2921 (Sept. 1994).

6. L. Thylen, "The beam propagation method: An analysis of its applicability," *Optical and Quantum Electronics*, Vol. 15, pp. 433-439 (1983).

7. J. Saijonmaa and D. Yevick, "Beam-propagation analysis of loss in bent optical waveguides and fibers," *J. Optical Society of America*, Vol. 73, pp. 1785-1791 (Dec. 1983).

8. R. C. Alferness, "Waveguide Electrooptic Modulators," *IEEE Trans. Microwave Theory Tech.*, Vol. MTT-30, pp. 1121-1135 (Aug. 1982).

9. C. H. Bulmer, "Sensitive, highly linear lithium niobate interferometers for electromagnetic field sensing," *Appl. Phys. Lett.*, Vol. 53, pp. 2368-2370 (Dec 1988).

10. C. H. Bulmer, W. K. Burns, and A. S. Greenblatt, "Phase Tuning by Laser Ablation of $LiNbO_3$ Interferometric Modulators to Optimum Linearity," *IEEE Photonics Tech. Lett.*, Vol. 3, pp. 510-512 (June 1991).

BIBLIOGRAPHY

R. A. Becker, C. E. Woodward, F. J. Leonberger, and R. C. Williamson, "Wideband electro-optic guided-wave analog-to-digital converters," *IEEE Proc.*, Vol. 72, pp. 802-819 (July 1984).

F. S. Chu and J. E. Baran, "Fabrication tolerance of Ti:LiNbO$_3$ waveguides," *J. of Lightwave Technology*, Vol. 8, pp. 784-788 (1990).

P. Danielsen, "Two-Dimensional Propagating Beam Analysis of an Electronic Waveguide Modulator," *IEEE J. of Quantum Electronics*, Vol. QE-20, pp. 1093-1097 (Sept. 1984).

P. Danielsen and D. Yevick, "Improved analysis of the propagating beam method in longitudinally perturbed optical waveguides," *Applied Optics*, Vol. 21, pp. 4188-4189 (Dec. 1989).

N. R. Desai, K. V. Hoang, and G. J. Sonek, "Applications of PSPICE Simulation Software to the study of Optoelectronic Integrated Circuits and Devices," *IEEE Trans. Edu.*, Vol. 36, pp. 357-362 (Nov. 1993).

M. D. Feit and J. A. Fleck, Jr., "Computation of mode properties in optical waveguides by a propagating beam method," *Applied Optics*, Vo. 19, pp.1154-1164 (April 1980).

M. D. Feit and J. A. Fleck, Jr., "Computation of mode eigenfunctions in graded-index optical waveguides by the propagating beam method," *Applied Optics*, Vol. 19, pp. 2240-2246 (July 1980).

M. D. Feit and J. A. Fleck, Jr., "An Analysis of Intersecting Diffused Channel Waveguides," *IEEE J. of Quantum Electronics*, Vol. QE-20, pp. 1093-1097 (Sept. 1984).

J. A. Fleck, Jr., J. R. Morris, and M. D. Feit, "Time-Dependent Propagation of High Energy Laser Beams through the Atmosphere," *Appl. Phys.*, Vol. 10, pp. 129-160 (1976).

O. Hanaizumi, M. Miyagi, and S. Kawakami, "Wide *Y*-Junctions with Low Losses in Three-Dimensional Dielectric Optical Waveguides," *IEEE J. of Quantum Electronics*, Vol. QE-21, pp. 168-173 (Feb. 1985).

D. A. M. Khalil and S. Tedjini, "Coherent Coupling of Radiation Modes in Mach-Zehnder Electrooptic Modulators," *IEEE J. of Quantum Electronics*, Vol. 28, pp. 1236-1238 (May 1992).

K. T. Koal and P. L. Liu, "Modeling of Ti:LiNbO₃ waveguide devices: Part II--S-shaped channel waveguide bends," *J. of Lightwave Technology*, Vol. 7, pp. 533-539 (Mar. 1989).

F. J. Leonberger, C. E. Woodward, and R. A. Becker, "4-bit 828-megasample/s electro-optic guided-wave analog-to-digital converter," *Appl. Phys. Lett.*, Vol. 40, pp. 565-569 (April 1982).

P. E. Pace, "Integrated Optical Guided Wave Architectures for Signal Processing and Computing," Ph.D. dissertation, Univ. of Cincinnati, Ohio, 1990, pp. 137-157.

H. F. Taylor and A. Yariv, "Guided-wave optics," *IEEE Proc.*, Vol. 62, pp. 1044-1060 (1974).

H. F. Taylor, M. J. Taylor, and P. W. Bauer, "Electro-optic analog-to-digital convertion using channel waveguide modulators," *Appl. Phys. Lett.*, Vol. 32, pp. 559-561 (May 1978).

H. F. Taylor, "An Optical Analog-to-Digital Converter--Design and Analysis," *IEEE J. of Quantum Electronics*, Vol. QE-15, pp. 210-216 (April 1979).

H. F. Taylor, "Extended Precision in Video-Bandwidth Analogue/Digital Convertors Using Optical Techniques," *Elec. Lett.*, Vol. 20, pp. 67-68 (April 1984).

J. Van Roey, J. van der Donk, and P. E. Lagasse, "Beam-propagation method: analysis and assessment," *J. Opt. Soc. Am.*, Vol. 71, pp. 803-810 (July 1981).

R. G. Walker, I. Bennion, and A. C. Carter, "Novel GaAs/AlGaAs Guided-Wave Analogue/Digital Convertor," *Elec. Lett.*, Vol. 25, pp. 1443-1444 (Oct. 1989).

S. Yamada, M. Minakata, and J. Noda, "High Speed 2-Bit Analogue-Digital Convertor Using LiNbO₃ Waveguide Modulators," *Elec. Lett.*, Vol. 17, pp. 259-260 (Apr. 1981).

S. Yamada, M. Minakata, and J. Noda, "Analog-to-Digital conversion using a LiNbO₃ balanced bridge modulator," *Appl. Phys. Lett.*, Vol. 39, pp. 124-126 (July 1981).

D. Yap and L. M. Johnson, "Radiation-field coupling in optical waveguide structures with closely spaced abrupt bends and branches," *Integrated Optical Circuit Engineering*, Vol. 517, pp. 137-141 (1984).

D. Yevick and B. Hermansson, "Efficient Beam Propagation Techniques," *IEEE J. of Quantum Electronics*, Vol. 26, pp. 109-112 (Jan. 1990).

D. Yevick and P. Danielsen, "Numerical investigation of mode coupling in sinusoidally modulated GRIN planar waveguides," *Applied Optics*, Vol. 21, pp. 2727-2733 (Aug. 1982).

R. C. Youngquist, L. F. Stokes, and H. J. Shaw, "Effects of Normal Mode Loss in Dielectric Waveguide Directional Couplers and Interferometers," *IEEE J. of Quantum Electronics*, Vol. QE-19, pp. 1888-1896 (Dec. 1983).

DISTRIBUTION LIST

<div align="right">No. Copies</div>

1. Defense Technical Information Center 2
   Cameron Station
   Alexandria, Virginia 22304-6145

2. Library, Code 52 2
   Naval Postgraduate School
   Monterey, California 93943-5101

3. Chairman, Code EC 1
   Department of Electrical and Computer Engineering
   Naval Postgraduate School
   Monterey, California 93943-5121

4. Chairman, Code PH 1
   Department of Physics
   Naval Postgraduate School
   Monterey, California 93943-5117

5. Professor Phillip E. Pace, Code EC/PC 2
   Department of Electrical and Computer Engineering
   Naval Postgraduate School
   Monterey, California 93943-5121

6. Professor Alfred W. M. Cooper, Code PH/CR 1
   Department of Physics
   Naval Postgraduate School
   Monterey, California 93943-5117

7. Professor Ronald Pieper, Code EC/PR 1
   Department of Electrical and Computer Engineering
   Naval Postgraduate School
   Monterey, California 93943-5121

8. Dr. Michael D. Feit 1
   Lawrence Livermore National Laboratory
   P.O. Box 808
   Livermore, California 94550

9. Dr. William K. Burns, Code 5671 1
    Naval Research Laboratory
    Optical Sciences Division
    Washington, DC 20375-5000

10. Dr. David Yevick 1
    Department of Electrical and Computer Engineering
    Queen's University at Kingston
    Kingston, Ontario, Canada, K7L3N6

11. Donald LaFaw 1
    Lab for Physical Sciences
    8050 Greenmead Drive
    College Park, Maryland 20740

12. Director, Training and Education 1
    MCCDC, Code C46
    1019 Elliot Rd.
    Quantico, Virginia 22134-5027